Measurement of single transverse spin asymmetry
via single hadrons and di-hadron correlations
in the 200GeV $p+p$ collision in the PHENIX experiment at RHIC

by

Feng Wei

A dissertation submitted to the graduate faculty

in partial fulfillment of the requirements for the degree of

DOCTOR OF PHILOSOPHY

Major: Nuclear Physics

Program of Study Committee:
John Lajoie, Major Professor
James Cochran
Jianwei Qiu
Alex Travesset
Jim Evans

Iowa State University

Ames, Iowa

2010

TABLE OF CONTENTS

Acknowledgements

First and foremost, I would like to thank my adviser Prof. John Lajoie. for his guidance and support throughout my research in these six years. He has always had a lot of good ideas and suggestions whenever I have discussed my work with him. He spent plenty of energy and time to teach me valuable knowledge and skills on PHENIX hardware, triggers, data analysis and Monte-Carlo simulation. He encouraged me to develop my own interests on spin physics. Such an accommodating and supportive supervisor is not something a graduate student can take for granted. I would like to thank Prof. Jianwei Qiu for valuable discussion and direction about theoretical physics on spin. Furthermore, thanks must go as well to Prof. James Cochran, Prof. Alex Travesset and Prof. Jim Evans for their encouragement and support. I would like to thank Dr. Zhongbo Kang for lots of valuable discussion and suggestion on various physics questions. I would like to thank Todd Kempel for help on my analysis. Thanks also go to my friends Yongxing Yao, Wei Bu, Ning Lu, Jie Ma, Yingzhou Du and Jizhou Chen for our friendship and for discussion on everything. I would like to dedicate this thesis to my wife Jun without whose support I would not have been able to complete this work. Her love and support in these years I would also like to thank my friends and family for their loving guidance during the writing of this work.

LIST OF TABLES

LIST OF FIGURES

CHAPTER 1. Historical Review

1.1 From matter to particles

"What is matter made of?" This fundamental question has puzzled people for thousands of years and was not well answered until the 20th century.

About 400 B.C., ancient Greek philosophers, such as Democritus, hypothesized that all matter is composed of tiny indestructible units, called "atoms". But the concept "atom" from ancient Greek philosophers is different from the modern concept of the atom that was first introduced by English natural philosopher John Dalton in chemistry in the early 19th century. In 1897 J.J.Thomson discovered the electrons and built a "plum pudding" model to describe the structure of atoms, which unveiled a new world of elementary particle physics. However, the "plum pudding" model was later proved incorrect by Ernest Rutherford by the famous α-particle scattering experiments that showed positive charge, and most of the mass of the atom, is concentrated in a tiny core, or nucleus, at the center of the atom. Rutherford gave the name "proton" to the nucleus of the lightest atom(Hydrogen). The discovery of neutrons by James Chadwick in 1932 made physicists realize that nucleus is made of protons and neutrons which is given a collective name "nucleons".

Now people seem to know the answer to the question above. However new questions quickly arose, "Are nucleons the most elementary partices? Are they point-like particles in a physics sense?"

1.2 The nucleon structure

1.2.1 The history of discovery

In 1931 Stern and collaborators measured the anomalous magnetic moment of the proton, which provided the first evidence that nucleons were more than mere point-like Dirac particles. Physicists began to study the structure of proton and neutron. In 1955, Hofstadter and McAllister made the first measurements of the RMS radius for the charge and magnetic moment of the proton and neutron which is clear evidence that protons and neutrons are not point-like particles. Then a question naturally came out "what kinds of more elementary particles are nucleons composed of?"

In 1961 Gell-Mann[43] and Ne'eman[45] developed a particle classification system known as the Eightfold Way which is also called SU(3) flavor symmetry. In 1964, a quark model was independently proposed by Gell-Mann and Zweig [44] which says all hadrons (baryons, such as the proton and neutron, and mesons, such as the pions) were composed of three types of quarks (q), defined as up (u), down (d) and strange (s). The theory was verified by experiments soon.

In 1968, a deep inelastic scattering (DIS) experiment at the Stanford Linear Accelerator Center (SLAC) led by Friedman, Kendall and Taylor showed that the proton contained much smaller point-like objects and was therefore not an elementary particle[46][47]. Physicists were reluctant to identify these objects with quarks at the time, instead calling them "partons" - a term coined by Richard Feynman[48]. With the experimental observation of Bjorken scaling, the validation of the quark model, and the confirmation of asymptotic freedom in quantum chromodynamics(QCD), the partons that were observed at the SLAC would later be identified as up and down quarks as the other flavors were discovered. Nevertheless, "parton" remains in use as a collective term for the constituents of hadrons (quarks, anti-quarks, and gluons).

All the theoretical and experimental work in 1960's and 1970's about the structure of hadrons and involved interaction (known as strong force) led to the development of the theory of Quantum Chromodynamics (QCD). QCD is a quantum field theory of a special kind called a non-abelian gauge theory. It is an important part of the Standard Model of particle physics.

QCD has two peculiar properties - asymptotic freedom and confinement, which make quarks behave as though strongly bound at a certain scale (about 10^{-15}m) and behave as free (very tiny interaction with each other) at shorter distances. Because the content of the theory is complicated, today various techniques have been developed to work with QCD such as perturbative QCD, lattice QCD, effective field theories and so on.

Bjorken realized that the probability of finding a parton inside a proton depended primarily on the fraction of the proton's momentum carried by the struck parton, which was called "x" in large Q^2 (Q is the momentum transfered from lepton to parton) inelastic scattering experiment [49]. These 1-D functions are called parton distribution functions (PDFs). Because of the inherent non-perturbative effect in a Quantum Chromodynamics (QCD) state, parton distribution functions cannot be obtained by perturbative QCD. Due to the limitations in present lattice QCD calculations, the known parton distribution functions are instead obtained by using experimental data. Several sets of PDFs are worked out by different collaborations. They are obtained by means of a global fit to experimental data for one or more physical processes which can be calculated using perturbative QCD, such as deep inelastic scattering, the Drell-Yan process and others. The commonly used sets includes CTEQ, GRV, MRST and NNPDF[64, 65, 66]. So far the PDFs of unpolarized proton have been determined very well.

However polarized protons are still not fully understood by physicists. More details about the structure of polarized protons are talked about in chapter 2.

1.2.2 Structure functions and PDFs of unpolarized protons

In an inelastic scattering experiment, the structure of the proton and neutron is described by the nucleon structure functions. The differential cross section for a typical electron-proton (ep) inelastic scattering as shown in Figure 1.1 can be written as in Eq. 1.1,

$$\frac{d\sigma}{dE'd\Omega} = \frac{4\alpha^2 E'^2}{q^4}(W_2(\nu, q^2)\cos^2\frac{\theta}{2} + 2W_1(\nu, q^2)\sin^2\frac{\theta}{2}) \tag{1.1}$$

where W_1 and W_2 are the proton structure functions, q is the four-momentum transfer in the scattering, α is the fine structure constant, θ is the electron scattering angle in the laboratory

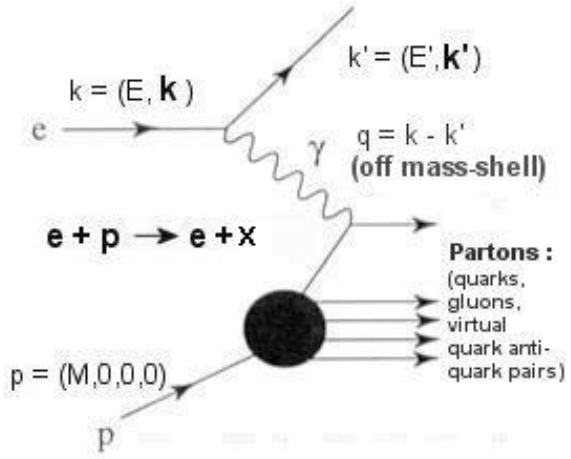

Figure 1.1 The semi-inclusive DIS process.

frame, E' is the scattered electron energy, and the energy loss of scattered electron $\nu = \frac{p \cdot q}{M}$ in which p is the initial nucleon four-momentum and M is is the invariant proton mass.

In 1969, Bjorken proposed that the structure functions W_1 and W_2 measured in deep inelastic scattering may exhibit scaling behavior in infinite momentum frame as shown in Eq. 1.2.

$$\begin{aligned} F_1(x) &= M \cdot W_1(\nu, Q^2) \\ F_2(x) &= \nu \cdot W_2(\nu, Q^2) \end{aligned} \tag{1.2}$$

where $Q^2 = -q^2$ and the dimensionless variable $x = \frac{Q^2}{2p \cdot q}$.

The Eq. 1.2 essentially says that there is no Q^2 dependence for a given value of x in proton structure functions at large Q^2. This led to the idea that inelastic electron-proton scattering at large Q^2 could be viewed as elastic scattering of an electron off of a hard, point-like particle within the proton. However, Bjorken scaling violations have been observed at low x and low Q^2 due to gluon radiation emitted by the parton prior to the hard scattering.

In 1969, Callan and Gross revealed the relation [42] between scaling structure functions $F_1(x)$ and $F_2(x)$ for spin-$\frac{1}{2}$ charged components in the nucleon, as shown in Eq. 1.3. $\frac{2xF_1(x)}{F_2(x)}$

measures the ratio of magnetic to electric scattering from partons. The ratio is unity for a Dirac parton (spin-$\frac{1}{2}$) and zero for spin 0 partons. They discovered that by measuring the ratio $R = \frac{\sigma_L}{\sigma_T}$ (where σ_L (σ_L) is the cross section for the scattering of longitudinal (transverse) polarized virtual photons), one could determine the spin of the charged constituents of the nucleon[50]. In the naive parton model with spin-$\frac{1}{2}$ partons, the relation in Eq. 1.4 was expected. If asymptotic scaling holds, $R = q^2/v^2$ in the limit of large q^2 so that we have $\frac{2xF_1(x)}{F_2(x)} = 1$. In late 1970s the SLAC experiments verified the prediction by Callan and Gross as shown in Figure 1.2, which provided strong evidence that quarks are spin-$\frac{1}{2}$ particles.

$$2xF_1(x) = F_2(x) \tag{1.3}$$

$$\frac{1+R}{1+q^2/\nu^2} = \frac{F_2(x)}{2xF_1(x)} \tag{1.4}$$

With the development and accomplishments of the Standard Model, six flavors of quarks are defined as up(u), down(d), strange(s), charm(c), bottom(b) and top(t). The existance of these six types of quarks have also been confirmed by experiments. The scaling structure functions can be expressed in terms of the parton distribution functions (PDFs) for different flavors as shown in Eq. 1.5.

$$\begin{aligned} F_1(x) &= \frac{1}{2}\sum_i e_i^2 f_i(x) \\ F_2(x) &= \sum_i e_i^2 x f_i(x) \end{aligned} \tag{1.5}$$

where e_i indicates the electromagnetic charge of the quark of flavor i, and $f_i(x)$ is just the parton distribution function of the quark of flavor i. The PDFs essentially give the probability of finding a certain parton with momentum fraction x. Gluons don't carry electromagnetic charge but the distribution of gluons inside nucleons can still be described by using a PDF, which is just not directly accessible in DIS.

Parton distribution functions are known in several sets worked out by different collaborations. They are obtained by means of a global fit to experimental data for one or more physical processes which can be calculated using perturbative QCD, such as deep inelastic scattering,

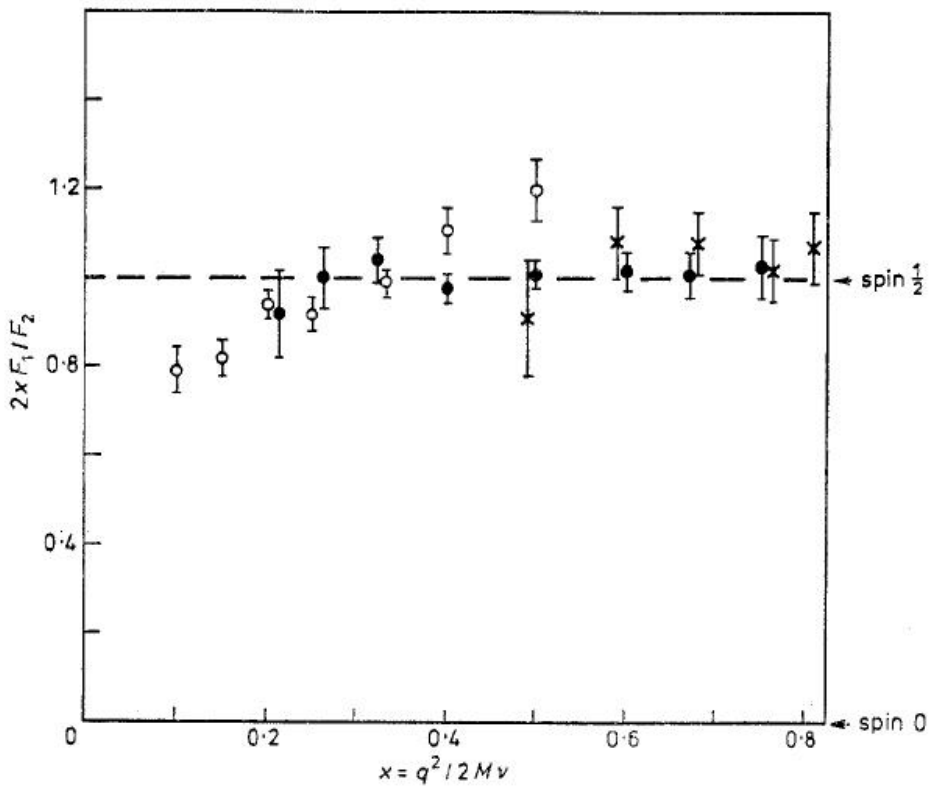

Figure 1.2 The ratio $\frac{2xF_1}{F_2}$ as a function of x for three ranges of q^2 (from Riordan et. al. 1975). For point-like asymptotic region ($q^2 \to \infty$). $\circ$, $q^2 = 1 - 3$GeV; $\bullet$, $q^2 = 4 - 10$GeV; $\times$, $q^2 = 12 - 16$GeV; $---$, Callan-Gross as $q^2 \to \infty$.

the Drell-Yan process and others. The commonly used sets includes CTEQ, GRV, MRST and NNPDF. An Example of PDFs from MRST is shown in Figure 1.3[54]. For the PDFs from other collaborations, please see [55, 56].

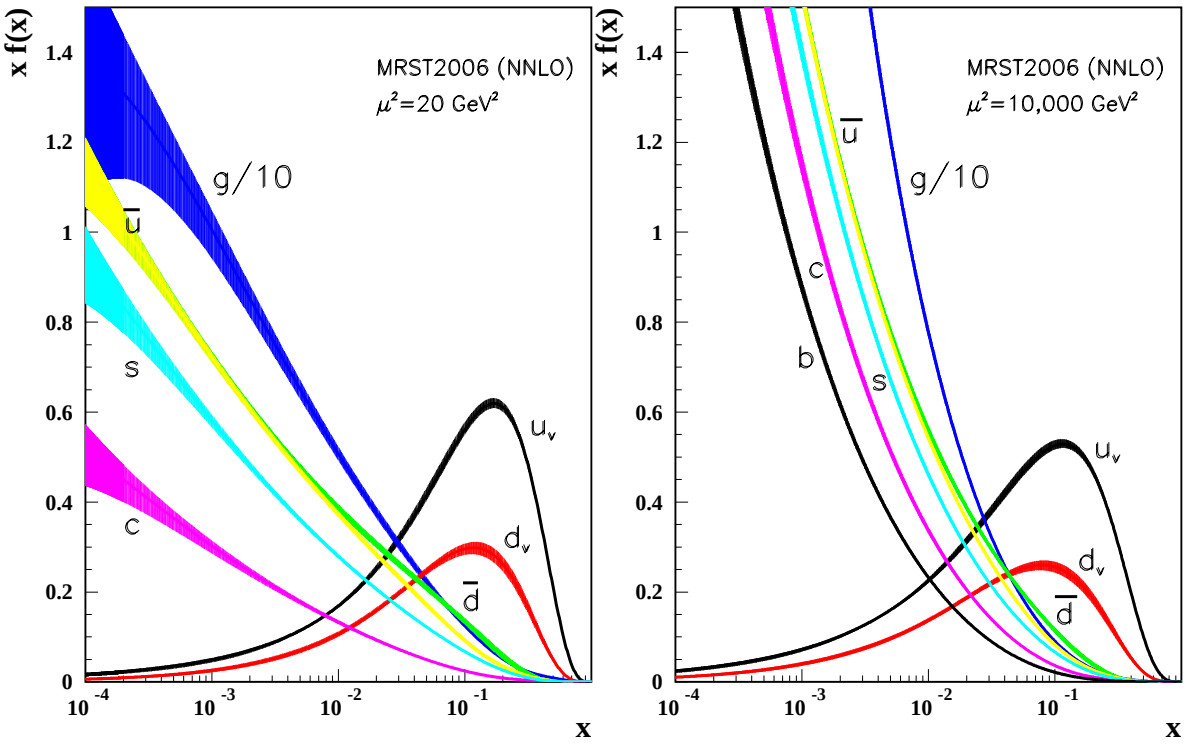

Figure 1.3 The parton distribution fuctions of unpolarized proton from MRST group in 2006.

CHAPTER 2. The structure of the polarized proton

2.1 The Longitudinal Spin Structure of the proton

2.1.1 Spin Crisis

Protons are spin-$\frac{1}{2}$ fermions and are composed of three valence quarks which also carry spin $\frac{1}{2}$ in units of Planck's constant $\hbar$. A naive model was used to describe the spin of the proton in terms of the valence quarks inside the proton by the direct sum of two aligned quark spins and one anti-aligned. However, in the late 1980's the European Muon Collaboration (EMC) published their polarized deep inelastic measurement of the proton's spin dependent structure function which suggested that the quarks' intrinsic spin contributes little of the proton's spin. At that time relativistic constituent quark models of the proton generally predict that about 60% of the proton's spin should be carried by the spin of its three valence quarks with the rest carried by orbital angular momentum. The most accurate polarization experiments have taught us that the contribution from the spin or helicity of the quarks inside is small, 30% at most, challenging our understanding about the structure of the proton[67].

A complete spin sum rule can be described as shown in Eq. 2.1, where Δq ($\Delta\bar{q}$) is spin contribution of quark (anti-quark), Δg is gluon spin, $L_q(L_{\bar{q}})$ is the angular momentum of quarks (anti-quarks), and L_g is the angular momentum of gluon.

$$\frac{1}{2} = \frac{1}{2}(\Delta q + \Delta\bar{q}) + \Delta g + L_q + L_{\bar{q}} + L_g \tag{2.1}$$

2.1.2 The pDIS experiment

The rest of proton spin can be from sea quarks, gluons and the angular momentum of quarks, anti-quarks besides from quarks. Our present knowledge about the spin structure

of the proton at the quark level comes from polarized deep inelastic scattering experiments (pDIS) which use high-energy polarized electrons or muons to probe the structure of a polarized proton. The spin experiments at CERN, DESY, JLab and SLAC involve firing high-energy charged leptons (electrons or muons) at a polarized proton target. The electron exchanges a deeply-virtual spin-one photon which acts as a high resolution probe of the quark structure of the target. The photon can be absorbed by a spin-$\frac{1}{2}$ quark polarized in the opposite direction to the photon but not by one polarized in the same direction as the photon (quarks have no spin-$\frac{3}{2}$ state). This allows us to extract information about the spin of the quarks when one controls the polarization of both the beam and the proton target.

The pDIS experiments have provided very good constraints on helicity parton distribution function of u (Δu) and d (Δd). However, pDIS expriments are not directly sensitive the gluon due to the fact that the photon and the gluon can not be coupled directly. In addition, the helicity distribution of sea quarks are not well-known for the same reason. They need more study by using polarized $p + p$ scattering.

Polarized PDFs are also investigated by many groups such as AAC[57, 58], GRSV[59], DSSV[51], and so forth. A recent NLO global fit to the world data for the PDFs of polarized quarks, antiquarks and gluon from DSSV group is shown in the Figure 2.1 [60].

2.1.3 Polarized $p + p$ Scattering at RHIC

The inconsistency between theoretical predictions and experimental results for the proton spin caused a well-known "Proton Spin Crisis". The challenge to understand the spin structure of the proton has inspired new experiments at RHIC to figure out the gluon spin and parton angular momentum contributions to the proton's spin.

In polarized $p+p$ collisions, we take advantage of the leading-order coupling of quarks and gluons due to strong interaction and can directly access the Δg. Since the 2003 polarized $p+p$ run at RHIC, the PHENIX experiment has made measurements of the logitudinal double-spin asymmetry (A_{LL}) of neutral poins (π^0) at mid-rapidity. Pion production dominated by gluon-gluon and gluon-quark interaction. Thus, the measurements are sensitive to the polarized

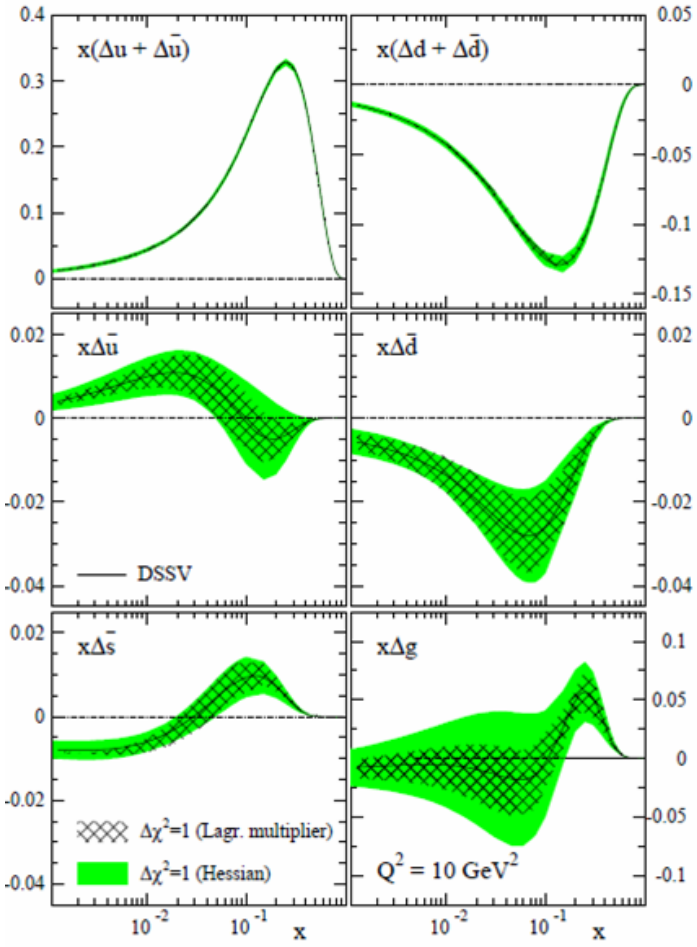

Figure 2.1 DSSV polarized PDFs of the proton at $Q^2 = 10\text{GeV}^2$ along with their uncertainty bands.

gluon distribution function. The current PHENIX result as shown in Figure 2.2 [18] as well as the recent global analysis[51] as shown in Figure 2.3 indicate Δg could be very small (nearly zero).

2.2 The Transverse Spin Structure of the Proton

The transverse spin structure of the proton is different from the longitudinal spin structure because the operations of Lorentz boosts and spatial rotations can not commute. The difference between the transverse and longitudinal polarization structure of the proton can lead us to understand the relativistic nature of partons bound within the proton. A detailed description

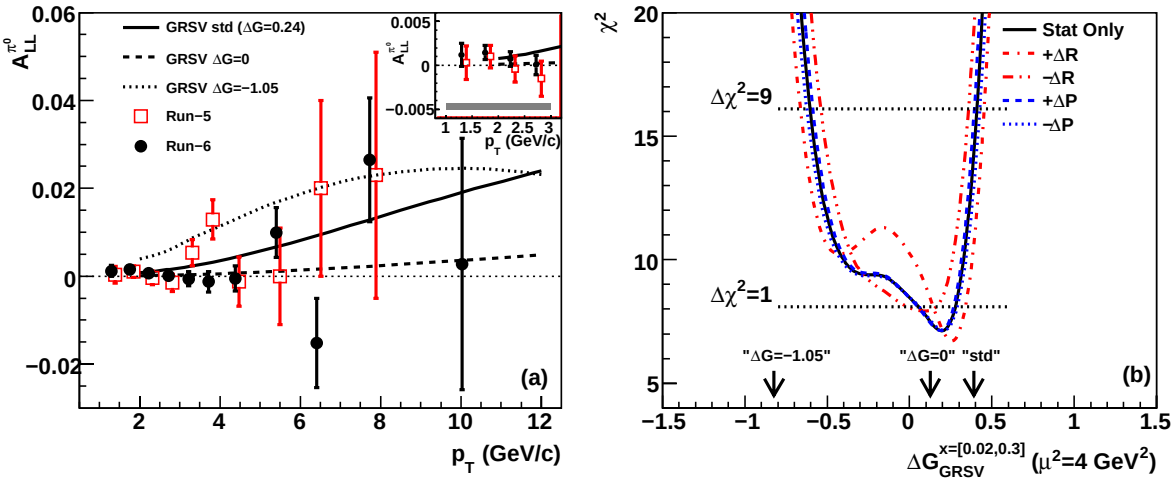

Figure 2.2 (a) Asymmetry in π^0 production as a function of p_T. (b) The χ^2 profile as a function of $\delta G^{[0.02,0.3]}_{GRSV}$. The χ^2 distribution of the measured data plotted versus the value of the first moment of the polarized gluon distribution (solid line) in the x_g range from 0.02 to 0.3 corresponding to our π^0 data in pT bins from 2 to 9 GeV/c. Dashed and dotted lines correspond to -9.4% and $+9.4\%$ variation in A_{LL} normalization related to the beam polarization uncertainty, the dominant systematical uncertainty of our data. Only statistical uncertainties were used for each curve. Arrows indicate ΔG corresponding to the different polarized gluon distributions.

of the relationship between transverse spin structure and longitudinal spin structure of the proton can be found in [19].

Similarly with the longitudinal spin sum rule, the transverse spin sum rule can be expressed in Eq. 2.2, where δq ($\delta\bar{q}$) is transversity of quark (anti-quark), $L_q(L_{\bar{q}})$ is the transverse component of angular momentum of quarks (anti-quarks), and L_g is the transverse component of angular momentum of gluon. Note that there is no transversity distribution for gluons at leading twist because there is no mechanism to flip the helicity of (spin-1) gluons in the scattering.

$$\frac{1}{2} = \frac{1}{2}(\delta q + \delta\bar{q}) + L_q + L_{\bar{q}} + L_g \tag{2.2}$$

The Soffer bound [52] shown in Eq. 2.3 gives the relation between transversity, helicity, and

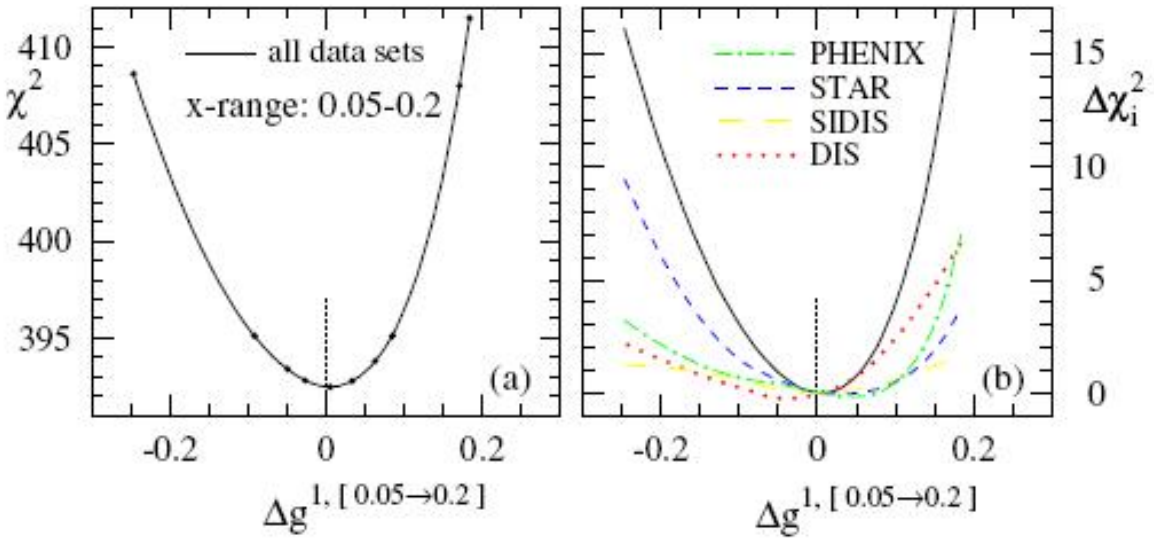

Figure 2.3 The χ^2 profile (a) and partial contributions $\Delta\chi_i^2$ (b) of the data sets for variations of $\Delta g^{1,[0.05\rightarrow0.2]}$ at $Q^2 = 10\text{GeV}^2$.

unpolarized quark distributions of the proton, where q(x) is unpolarized quark distribution function and $\Delta q(x)$ is quark helicity distribution function.

$$|2\delta q(x)| \leq q(x) + \Delta q(x) \tag{2.3}$$

2.2.1 The Transverse Single Spin Asymmetry

Measuring the transverse single spin asymmetry (SSA) is a very important method to probe the spin structure of transversely polarized protons. The transverse single spin asymmetry is defined as Eq. 2.4, where $\sigma^{\uparrow}$ ($\sigma^{\downarrow}$) is cross section of measured hadrons fragmented from the parton in the proton carrying spin $\uparrow$ ($\downarrow$). $\sigma^{\uparrow} - \sigma^{\downarrow}$ represents the spin difference cross section, while $\sigma^{\uparrow} + \sigma^{\downarrow}$ indicates the spin average cross section which is essentially unpolarized cross section.

$$A_N = \frac{\sigma^{\uparrow} - \sigma^{\downarrow}}{\sigma^{\uparrow} + \sigma^{\downarrow}} \tag{2.4}$$

In the early 1970s, a leading-twist pQCD calculation predicted that the transverse SSA should be propotional to $\alpha_s \frac{m_q}{\sqrt{s}}$ [20], where α_s is the strong coupling constant, m_q is the mass

of quark and $\sqrt{s}$ is the center of mass energy of the collision. The mass of light quarks u and d is much smaller than typical $\sqrt{s}$ and α_s can be treated as 1. Thus, the expected transverse SSA is quite small, roughly in order of 10^{-4}. However, the E704 experiment at FNAL initially observed surprisingly large asymmetries for π^+, π^- and even π^0 as shown in Figure 2.4 [21].

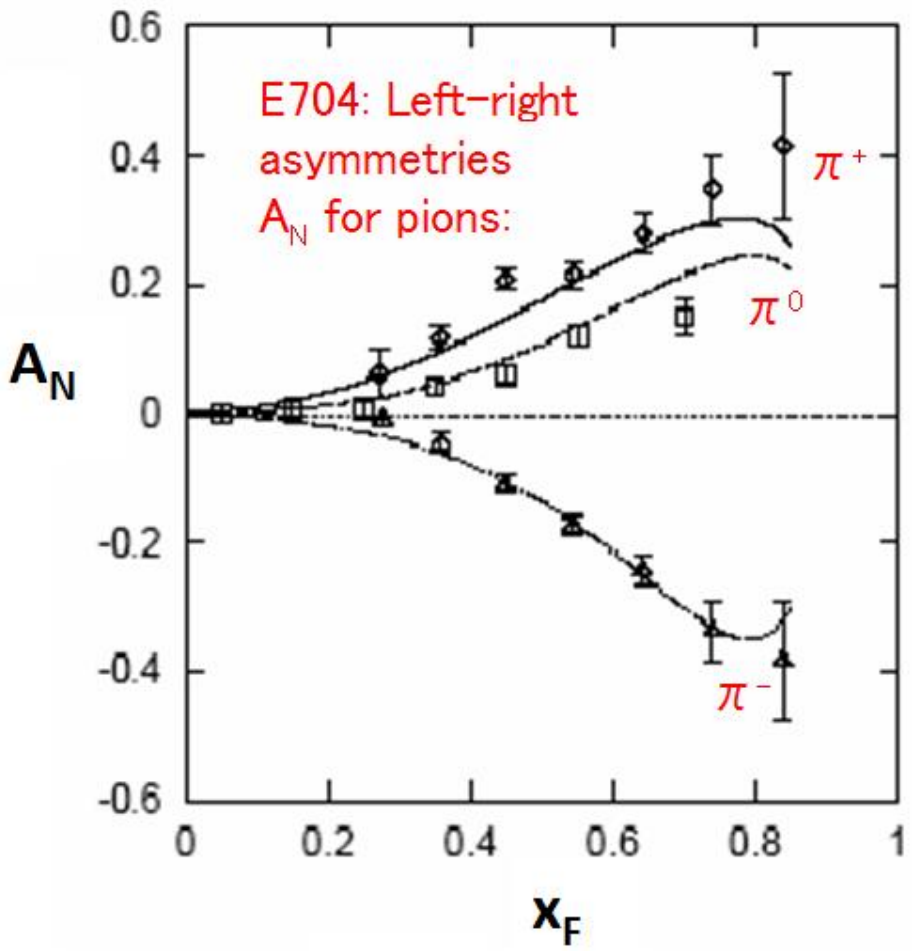

Figure 2.4 The measurement of single transverse spin asymmetries for pions from E704 experiment at FNAL.

In 1989, Dennis Sivers proposed that these large asymmetries could be generated by a transverse-momentum-dependent partonic distribution (TMD), in which the transverse momentum of the partons is correlated with the spin of the proton [23]. This work is known as the "Sivers effect". In 1991, Qiu and Sterman [24] consistently evaluated such asymmetries in terms of generalized factorization theorems in perturbative QCD based on the point of view

by Efremov and Teryaev [25] that a non-vanishing SSA can be obtained in perturbative QCD if one goes beyond the leading power. This work is also called Efremov-Teryaev-Qiu-Sterman (ETQS) mechanism, or twist-3 approach to the SSAs.

Another common explanation suggests that the SSAs may be related to the transversity distribution of the quarks in the proton convoluted with a transverse momentum dependent fragmentation function, known as the Collins function[26]. The Collins function, which gives the distributions for a transversely polarized quark to fragment into an unpolarized hadron with non-zero transverse momentum, has aroused great interest recently since a chiral-odd structure function can be accessible together with another chiral-odd distribution/fragmentation function. The Collins effect has been measured at BELLE[53].

Thus, a possible expansion of transverse SSA is described schematically in Eq. 2.5, where A_N is the single spin asymmetry, $f_{1T}^{\perp}$ is the Sivers function, D_1 is fragmentation function of unpolarized parton, δq is the transversity and $H_1^{\perp}$ is the Collins function.

$$A_N \propto f_{1T}^{\perp} \otimes D_1 + \delta q \otimes H_1^{\perp} + ... \tag{2.5}$$

2.2.2 The Sivers Effect

The Sivers effect is a correlation between the direction of the transverse spin of the proton and the transverse momentum direction of an unpolarized parton inside the proton. Being different from the PDFs of an unpolarized proton, Sivers introduces a small intrinsic transverse momentum $k^{\perp}$ which changes the PDFs of transversely polarized proton to be decribed as shown in Eq. 2.6.

$$\hat{f}(x, \vec{k}^{\perp}, \vec{S}_T) = f(x, k^{\perp}) + \frac{1}{2}\Delta^N f(x, k^{\perp}) \frac{\vec{S}_T \cdot (\vec{p} \times \vec{k}^{\perp})}{|\vec{S}_T||\vec{p}||\vec{k}^{\perp}|} \tag{2.6}$$

where $\vec{k}^{\perp}$ is the partons' intrinsic transverse momentum with $k^{\perp} = |\vec{k}^{\perp}|$, $f(x, k^{\perp})$ is the unpolarized parton distribution, $\Delta^N f(x, k^{\perp})$ denotes the Sivers function and $\vec{S}_T$ is the transverse polarization of the proton, $\vec{p}$ is the three-momentum of the proton. As we can see, the correlation proposed by Sivers corresponds to a time-reversal odd triple product $\vec{S}_T \cdot (\vec{p} \times \vec{k}^{\perp})$.

In experiment, the Sivers effect has been observed in semi-inclusive deeply-inelastic scattering (SIDIS)[68]. In order to investigate the Sivers effect in polarized $p+p$ collision, W. Vogelsang et al. proposed that this effect may be observed from jets correlation[27, 69] in a leading power. Two outgoing jets are approximately back-to-back in azimuthal angle in the plane perpendicular to the direction of the incoming proton beams at unpolarized $p+p$ collision, which is $\Delta\phi \equiv \phi_{j2} - \phi_{j1} = \pi$. In the polarized $p+p$ collision, a left-right imbalance in $\vec{k}^{\perp}$ of the parton will then affect the $\Delta\phi$ distribution of jets nearly opposite to the leading jet and give the cross section an asymmetric piece around $\Delta\phi = \pi$ as shown in Figure 2.5.

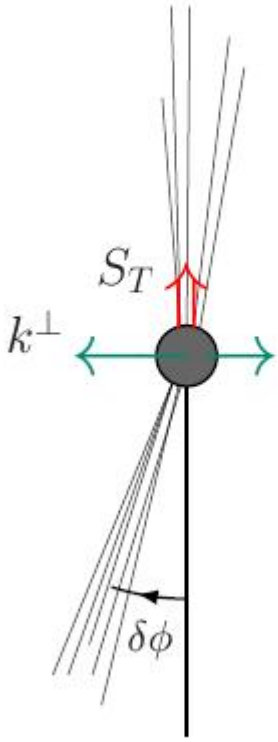

Figure 2.5 Asymmetric jet correlation. The proton beams run perpendicular to the drawing.

In the PHENIX experiment, because the central arms only cover half of the azimuthal angle and don't have full 2π azimuthal acceptance, it is very difficult to fully reconstruct the jets. Therefore, we are using di-hadron correlation instead of di-jet correlation in this thesis. In PHENIX, a lot of jet properties from di-hadron correlation in $p+p$ collisions have been

studied[61]. The sum of transverse momentum of two leading hadrons from two jets statistically (may not be in event-by-event basis) carries the information of $\vec{k}^{\perp}$, which is defined as $\vec{q}_t$ as shown in Figure 2.6.

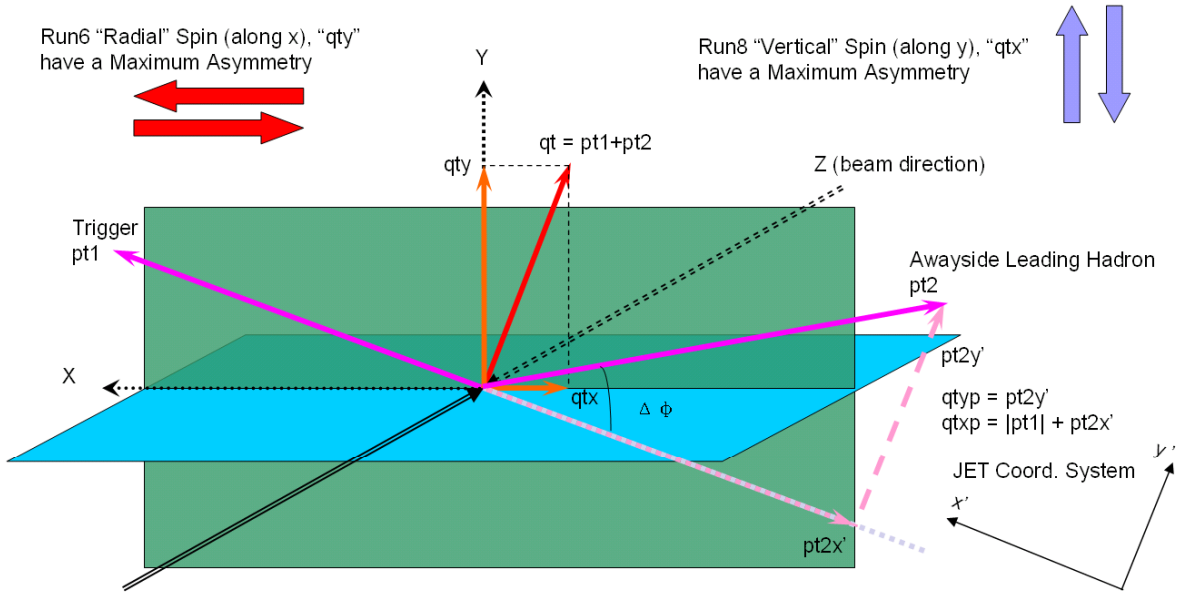

Figure 2.6 Variable definitions in di-hadron correlation.

The PHENIX coordinate $\vec{X}$, $\vec{Y}$, $\vec{Z}$ is defined in Figure 2.6. In Run6, the transverse spin direction $\vec{S}_T$ in the transverse running is radial (along $\vec{X}$ direction). The incoming protons momentum $\vec{p}$ is along $\vec{Z}$ direction. So in Run6 case, the Sivers function in Eq. 2.6 can be rewritten as

$$\begin{aligned} \hat{f}(x, \vec{k}^{\perp}, \vec{S}_T) &= f(x, k^{\perp}) + \frac{1}{2}\Delta^N f(x, k^{\perp}) \frac{\vec{X} \cdot (\vec{Z} \times \vec{k}^{\perp})}{|\vec{k}^{\perp}|} \\ &= f(x, k^{\perp}) + \frac{1}{2}\Delta^N f(x, k^{\perp}) \frac{k_y^{\perp}}{|\vec{k}^{\perp}|} \end{aligned} \tag{2.7}$$

where $k_y^\perp$ is y-component of $\vec{k}^\perp$. By replacing $\vec{k}^\perp$ by $\vec{q}_T$ in Eq. 2.7, we can know that q_{Ty}, the y-component of q_T, should be similar with $k_y^\perp$ which is sensitive to the asymmetry.

2.2.3 The Collins Effect

The Collins effect describes a parton spin dependent azimuthal asymmetry in the distribution of hadrons within a jet. In theory, this effect can be described by the Collins fragmentation function (FF) which was proposed in the early 1990's by Collins, Heppelmann, and Ladinsky [28, 29, 30]. The Collins FF represents the correlation between the transverse polarization of the fragmenting quark and the orientation of the hadron production plane, given by $\vec{S}\cdot(\vec{k}\times\vec{p}_h)$, where $\vec{S}$ is the transverse polarization scattered quark, $\vec{k}$ is its three-momentum, and $\vec{p}_h$ is the three-momentum of the final-state hadron.

In measurement of SSA of the polarized $p+p$ collision, the Collins FF is always convoluted with transversity as shown in Eq. 2.5. It is not possible to separate the transversity and the Collins FF in both SIDIS and polarized $p+p$ collision. In 2005, a transverse momentum dependent Collins fragmentation function (FF) measured in e^+e^- annihilation was published by the BELLE experiment [53]. The availability of the Collins FF makes it possible to extract the transversity distribution from asymmetry measurements in $p+p$ collisions since the Collins FF is regarded as a universal function. As constraints start to be provided on transversity and the various transverse-momentum-dependent distribution and fragmentation functions, more can in turn be learned from hadronic collision data.

CHAPTER 3. RHIC

3.1 Introduction

The Relativistic Heavy Ion Collider (RHIC) is located at and operated by Brookhaven National Laboratory in Upton, New York. It is the first heavy-ion collider, and the first and only polarized-proton collider in the world. RHIC is hexagonal in shape, 3.83km long circumference and has six interaction points (IPs), four of which are/were used by PHENIX, STAR, BRAHMS and PHOBOS experiments and the other two are used for the radio frequency system (RF) and polarimetry. As an intersecting storage ring particle accelerator, two independent, super-conducting rings (named as "blue" and "yellow" rings) allow collisions between species of ions such as proton(p), deutron(d), copper(Cu), gold(Au) and so on with a maximum energy of 100GeV per nucleon for heavy ions and a maximum energy of 250GeV for protons. Each ring has an independent source of ions, which permits the collisions of unlike ion species. The main types of ion collions started at RHIC so far are p + p, d + Au, Cu + Cu and Au + Au.

Before ions are injected into RHIC, they are pre-accelarated to 9GeV per nucleon by several stages of boosters such as Tandem Van de Graaff accelerator, Booster Synchrotron and Alternating Gradient Synchrotron(AGS). In RHIC, ions continue to be accelerated to make center-of-mass energy ($\sqrt{s}$) of 62.4GeV, 200GeV and 500GeV collions. The collions in RHIC are made bunch by bunch. Each beam has maximum 120 bunches positions for ions storage, up to 112 bunches are actually filled, the other 8 bunches keep empty for beam alignment and safe beam abort. Each bunch can contain roughly 1×10^9 gold ions or 2×10^{11} protons. Typical collider operation at $\sqrt{s} = 200$GeV $p+p$ has a luminosity $2 \times 10^{32} cm^{-2} s^{-1}$. The design polarization for proton beams is 70%, and the current polarization performance is roughly 60% for 200GeV runs. This is being improved for future running at $\sqrt{s} = 500$GeV for the polarized

proton program.

In the four major experiments mentioned above, PHENIX and STAR are two large experiments and still active so far, BRAHMS and PHOBOS are relatively small experiments and have finished their goals and ended their physics program. PHENIX, STAR and BRAHMS all have a spin-physics program. They provide overlap and complementary measurements with each other, which not only keep respectively specific research area but also is able to make cross-check on results.

3.2 RHIC as a Polarized $p + p$ Collider

As the first and only polarized $p + p$ collider in the world, RHIC has installed a lot of equipment relevant for polarized proton beams as shown in Figure 3.1. More details about RHIC as a polarized-proton collider are introduced in [1].

3.2.1 Polarized Proton Source and Boosters

The optically pumped polarized H^- source (OPPIS) technique is applied for polarized H^- ion beam production at RHIC, which was developed in the early 1980's at KEK (Japan), INR Moscow (Russia), LAMPF (USA) and TRIUMF (Canada) citepolsource. This technique is based on spin-transfer collisions between a proton or atomic hydrogen beam of a few keV beam energy and optically-pumped alkali metal vapors, which can produce protons with 85% polarization. Polarzied protons are then accelerated to 200MeV by the Linac and injected into the Booster. Proton bunches are injected into the AGS ring from the booster ring with energy of 2GeV per proton. The bunches are then accelerated to approximately 23GeV, and then injected into RHIC ring. Since there are many depolarizing resonances in AGS and RHIC that cause great polarization loss, Siberian snakes are used to remove those depolarizing resonances and greatly reduce polarization loss of protons.

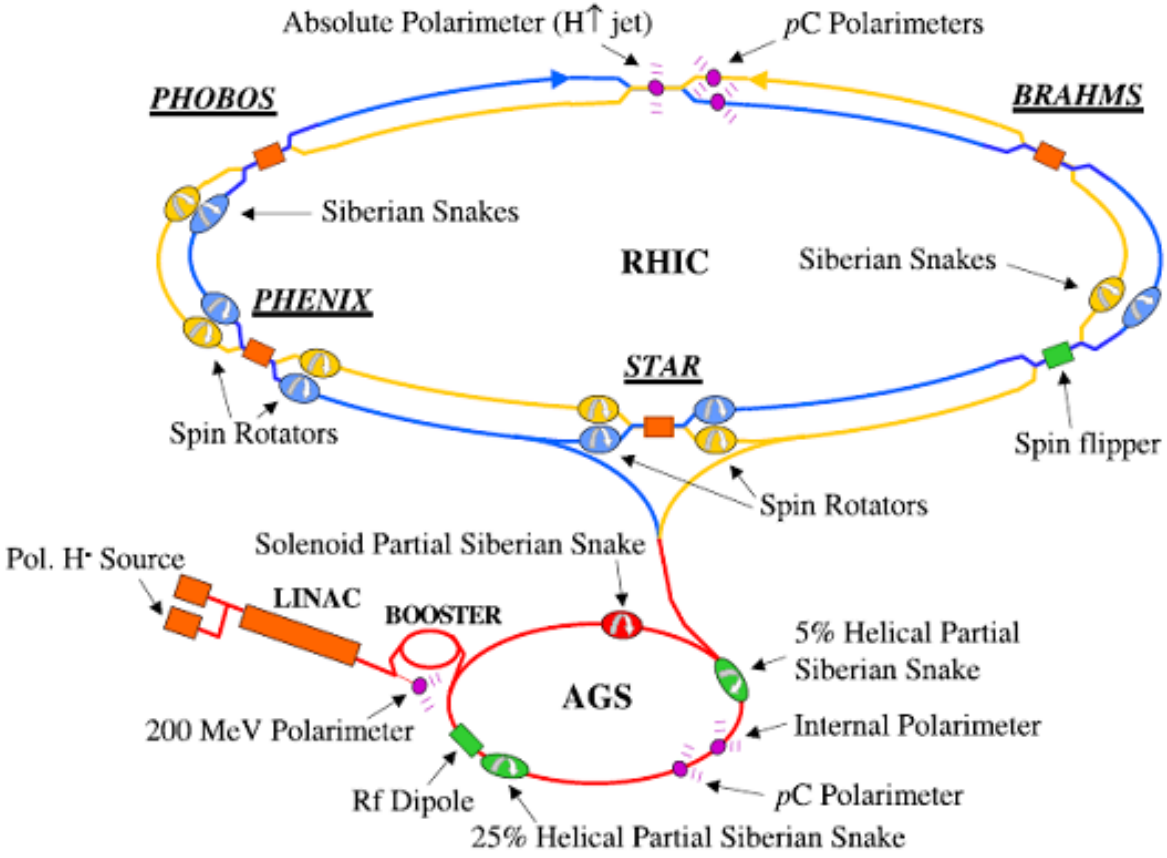

Figure 3.1 The RHIC polarized proton facility.

3.2.2 Siberian Snakes

Accelerating polarized beams requires an understanding of both the orbital motion and spin motion. Whereas the effect of the spin on the orbit is negligible the effect of the orbit on the spin is usually very strong. The evolution of the spin direction of a beam of polarized protons in external magnetic fields such as exist in a circular accelerator is governed by the Thomas-BMT equation [4] (Eq. 3.1),

$$\frac{d\vec{p}}{dt} = -(\frac{e}{\gamma m})[G\gamma\vec{B}_{\perp} + (1+G)\vec{B}_{\parallel}] \times \vec{p} \tag{3.1}$$

where the polarization vector $\vec{p}$ is expressed in the frame that moves with the particle, e is the proton charge, m is the proton mass, $\gamma = \frac{E}{m}$ is the relativistic boost, $G = 1.7928$ is the anomalous magnetic moment of the proton, $B_{\perp}$ indicates the magnetic field perpendicular to

the plane of proton motion, typically the vertical guide field, and $B_{\parallel}$ is the longitudinal field. For very high energy proton beams, γ is very large so that $B_{\perp}$ term dominates.

This simple precession equation is very similar to the Lorentz force equation which governs the evolution of the orbital motion in an external magnetic field (Eq. 3.2):

$$\frac{d\vec{v}}{dt} = -(\frac{e}{\gamma m})B_{\perp} \times \vec{v} \tag{3.2}$$

From comparing these two equations it can readily be seen that, in a pure vertical field, the spin rotates $G\gamma$ times faster than the orbital motion. In this case the factor $G\gamma$ then gives the number of full spin precession for every full revolution, which is also called the spin tune v_{sp}. At RHIC energy of $200GeV$, v_{sp} reaches about 400.

The acceleration of polarized beams in circular accelerators is complicated by the presence of numerous depolarizing spin resonances. During acceleration, a spin resonance is crossed whenever the spin precession frequency equals the frequency with which spin-perturbing magnetic fields are encountered. There are two main types of spin resonances corresponding to the possible sources of such fields: imperfection resonances, which are driven by magnet errors and misalignments, and intrinsic resonances, driven by the focusing fields. The resonance conditions are usually expressed in terms of the spin tune v_{sp}. The resonance condition for imperfection depolarizing resonances arise when $v_{sp} = G\gamma =$ n, where n is an integer. Imperfection resonances are therefore separated by only 523MeV energy steps. The condition for intrinsic resonances is $v_{sp} = G\gamma = kP \pm v_y$ where k is an integer, v_y is the vertical betatron tune and P is the super-periodicity. When a polarized beam is accelerated through an isolated resonance, the final polarization can be calculated as shown in Eq. 3.3

$$\frac{P_f}{P_i} = 2e^{-\frac{\pi|\epsilon|^2}{2\alpha}} - 1 \tag{3.3}$$

where P_i and P_f are the polarizations before and after the resonance crossing, respectively, and α is the change of the spin tune per radian of the orbit angle.

Siberian snakes are actually a series of spin-rotating dipoles, so named because of the beam trajectory through the magnets and the fact that they were developed at Novosibirsk. For polarized protons in RHIC, two full Siberian snakes per ring are 180° apart and with their

axis of spin precession at 90° to each other[3]. At higher energies a full Siberian snake, which is a 180° spin rotator of the spin about a horizontal axis, will keep the stable spin direction unperturbed at all times as long as the spin rotation from the Siberian snake is much larger than the spin rotation due to the resonance driving fields. Therefore the beam polarization is preserved during acceleration[5].

3.2.3 RHIC Polarimeters

The polarization of the proton beams at RHIC is measured by using two different sets of polarimeters, the polarized hydrogen gas jet (H-Jet) polarimeter[9] and the proton-carbon (pC) polarimeter[8]. These polarimeters are set up in 12 o'clock area (IP12) at the RHIC ring. The H-Jet polarimeter is located at the collision point allowing measurements of both beams. Two identical pC polarimeters are equipped in the yellow and blue rings, where the rings are separated. The pC-polarimeter measures relative polarization to a few percent statistical accuracy within 20 to 30 seconds using an ultra-thin (typically $6-8\mu g/cm^2$) carbon ribbon target, providing fast feedback to beam operations and experiments. Sufficient statistics also allows us to observe microscopic structures of the beam such as bunch by bunch basis polarizations and a polarization profile. The absolute normalization is provided by the H-Jet polarimeter, operated in parallel to pC polarimeters. It accumulates statistics less than pC polarimeters, i.e. takes over $1-2$ days to obtain approximately 5% statistical uncertainty. The operation of pC polarimeters was thus focused on the better control of relative stability between one measurement to another rather than the polarization measurement in an absolute scale[10].

3.2.4 Spin Rotators

As discussed above, the stable spin direction in each ring is vertical with spin up between snakes in one half of the ring and spin down in the other half. However, the collisions of longitudinally polarized protons are required for measurements of A_{LL} and W Physics. Thus, four spin rotator dipole magnets for both PHENIX and STAR experiments have been commis-

sioned in 2003 to achieve both longitudinal and radial spin. The spin direction is rotated away from vertical immediately before the collision point and then back to vertical immediately afterwards.

3.2.5 Polarization Performance

The performance for RHIC transverse polarized runs for single spin asymmetry can be evaluated by the figure of merit (FOM) which is defined in Eq. 3.4,

$$FOM = \langle P \rangle^2 \cdot \int Ldt \tag{3.4}$$

where $\langle P \rangle$ is the average polarization over the run and $\int Ldt$ is the integral luminosity of the run. This equation clearly shows that polarization is the dominant effect on the RHIC performance and doubling polarization is equivalent to a factor of 4 increase in luminosity.

The RHIC performance and center of energy for transversely polarized runs in past years is listed in Table 3.1.

Table 3.1 The performance of RHIC Transversely polarized runs

Year	$\sqrt{s}$ **(GeV)**	$\int Ldt$ $\mathbf{pb}^{-1}$	**Polarization (%)**	**FOM** $(10^{-2}\mathbf{pb}^{-1})$
2001 Run2	200	0.15	15	0.34
2005 Run5	200	0.16	47	3.53
2006 Run6	200	2.7	51	70.23
2006 Run6	62.4	0.02	48	0.46
2008 Run8	200	5.2	46	110.03

CHAPTER 4. PHENIX Experimental Setup

4.1 Global Detectors

In PHENIX, two pairs of detectors, Beam-Beam Counters (BBCs) and Zero-Degree Calorimeters (ZDCs), at forward (North) and backward (South) pseudo-rapidity are used to determine the necessary global event information as following:

- Determine if a collision has occurred.
- Determine if a collision should be triggered on.
- Determine the initial time of the collision for time-of-flight (TOF) measurements.
- Determine the collision point (in the case of PHENIX, the vertex point along the beam direction).
- Determine the collision centrality in heavy ion reactions.

4.1.1 The Beam-Beam Counters

In PHENIX the Beam-Beam Counters (BBCs) are used in all aspects of event characterization. The BBCs[13] are sets of 64 Cherenkov counters symmetrically placed 144cm along the beam line and cover 2π azimuth and $3.0 < |\eta| < 3.9$ units of pseudo-rapidity. The BBCs are part of the Global Level-1 (GL1) trigger system which determines if a collisions has occurred. A minimum-bias (MB) trigger occurs when there is a minimum of one photomultiplier tube (PMT) fired in each of the two BBCs. The BBCs determine the event vertex from the average time difference between leading particles reaching each BBC. In $200GeV$ $p+p$ collisions, the

BBCs see approximately 50% of the total inelastic p+p cross section and provide a online vertex resolution of approximately 5cm.

4.1.2 The Zero-Degree Calorimeters

Two compact hadronic Zero-Degree Calorimeters (ZDC) with tungsten absorber plates[12] are installed close to the beam pipe at a distance of 18m north and south of the interaction point, placing them at very forward ($|\eta| > 6$) pseudorapidities. Since the ZDC's are located behind the dipole magnets, the bending of charged particles away from the ZDC allows for a determination of the deposited energy of spectator neutrons with a resolution of 20%. The ZDCs are primarily used in $p + p$ collisions as local polarimetry and to do a systematic study on the relative luminosity between bunch crossings with different spin configurations. ZDCs are also provide information on the collision vertex with relatively poorer online resolution approximately 30cm.

4.2 Central Arm Detectors

The detector subsystems in the two central arm spectrometers are stacked in layers (see Figure 4.1). For the analysis presented here, two wire chambers,the Drift Chamber (DC) and the first Pad Chamber plane (PC1) provided the primary charged particle tracking. Tracks were also linked to the third and outermost Pad Chamber plane (PC3) to reject background from conversions and decays. The Ring Imaging Cherenkov (RICH) detector is mainly used for electron detection. For our analysis, we used the RICH to reject electron contributions to charged tracks. The energy deposit by photons and charged particles can be measured by electromagnetic calorimetry (EMcal), which covers the full central arm acceptance and is divided into four sections per arm.

4.2.1 The Drift Chamber

Two identical Drift Chamber cylinders with a longitudinal extent of 2m are located in a residual magnetic field at $2 - 2.4$m referenced to the beam-axis. The gas volume is filled with

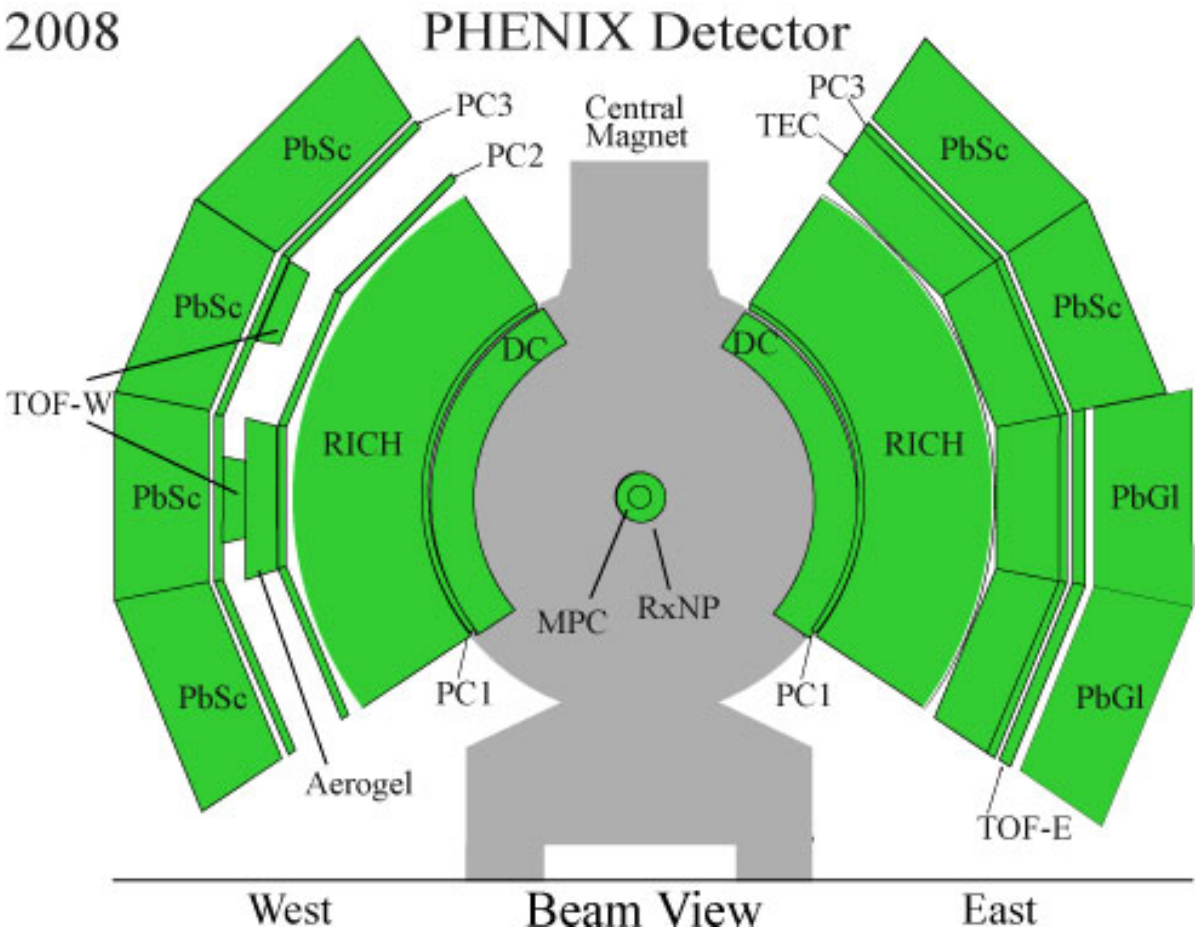

Figure 4.1 A view along the beam pipe for PHENIX central arm detectors in Run8.

a 50% by 50% mixture of argon and ethane. The DC contains two groups of wire planes. The first group of twelve wire planes (X wires) measure trajectories of charged particles in the $r - \phi$ direction with a track finding efficiency of greater than 99% and a two-track resolution of 2mm[14]. The second group of eight stereowire planes (U,V wires) provide a measurement of the z-coordinate. Due to the low stereo angle and the small number of wires, this measurement does not give the optimal resolution. To obtain the most accurate measurement of the longitudinal track component, the DC stereo wires, the Pad Chamber and the BBC z-vertex position information are combined. Wire planes in front of the drift chamber reference radius ($R = 2.2$m) are labeled X1, U1, V1 and those beyond the reference radius are denoted X2, U2 and V2.

4.2.2 The Pad Chambers

The Pad Chambers are multiwire proportional chambers and are installed outside of the magnetic field region. They consist of a wire plane, enclosed in a gas volume by two cathode walls. One of the cathode planes is sub-structured into pixels with pad readout, the other consists of an etched copper layer. The cathode panels have a sandwich structure that provides sufficient strength so that no additional frame support is needed. This design results in a greatly reduced radiation thickness, keeping the creation of conversion electrons to a minimum. The operating gas for the Pad Chamber is as same as the DC, which is also a 50% by 50% mixture of argon and ethane.

Three separate Pad Chamber planes, covering a total area of 88m^2, are used to determine three dimensional hit information for charged particle tracks. The first plane (PC1) at radial distance of 2.5m is mounted to the Drift Chamber. The third Pad Chamber plane (PC3) is located 4.9m away from the beam pipe between the RICH and EmCal detectors (see Figure 4.1). Track projection from the DC to PC3 plays an important role in background rejection. The PC1 and PC3 planes are present in both arms, while the second plane (PC2) is only installed in the west arm at a radial distance of 4.2m behind the RICH detector. The PC2 is not used in this analysis.

4.2.3 The Ring Imaging Cherenkov Detector

In each central arm, a Ring Imaging Cherenkov (RICH) detector is mounted after the PC1 and used for electron identification. If an electron traverses the CO_2 filled RICH volume with a velocity greater than the speed of light in the medium, Cherenkov light is radiated and reflected by two intersecting spherical mirrors onto two detectors with 40 modules of 32 photomultiplier tubes each. With CO_2 as operating gas, the heavier pions start to fire the RICH above $p_T \approx 4.65\text{GeV}/c$ and therefore good electron/pion separation is achieved below this value. A more detailed description of the RICH detector layout and performance can be found in [14]. In this analysis the RICH detector is only used to reject electron contributions to the charged tracks.

4.2.4 The Electromagnetic Calorimeter

The Electromagnetic Calorimeter (EmCal) consists of two subsystems. Six sectors of lead-scintillator (PbSc) detectors and two sectors of lead-glass (PbGl) detectors cover the full central arm acceptance of PHENIX. Both set of detectors have been designed to measure electrons and photons with excellent timing and good position and energy resolution. They also provide a very good measurement of the hadronic energy. The hadronic response of the PbSc detector is well understood. The hadronic response of the PbGl is not. For this reason, and also because of the better timing resolution, the PbSc is the calorimeter of choice for hadron identification in this work. The design and performance of the EmCal is reported in [15]. In what follows, we will therefore only focus on the most important features of the PbSc detector. The PbSc is a sampling calorimeter made of a large number of "towers". A total of 66 sampling scintillator cells and lead tiles are combined in an alternating pattern to form such a tower. Light is collected via wavelength shifting fibers that are directly connected to the cells and read out by a photo-tube. An illustration of a typical PbSc module layout is given in Figure 4.2. Four towers form a module and 36 modules form a supermodule. Each sector consists of 18 supermodules. Electromagnetic and hadronic particles deposit energy differently in a module and the shower shape can be used to distinguish between them [15].

4.3 Muon Arm Detectors

The PHENIX Muons Arms (as shown in Figure 4.3) consist of two independent spectrometers at both forward and backward directions of the interaction point, corresponding to $1.2 < |\eta| < 2.4$ for the North arm and $1.2 < |\eta| < 2.2$ for the South arm. Each spectrometer is designed with sufficient geometric acceptance (one steradian), momentum resolution, and muon identification capabilities to permit the study of vector meson production, the Drell-Yan process (via muon pairs), and heavy quark production (through both muon pairs and single muons). The muon arms, augmented with anticipated upgrades, will also play an important role in the RHIC spin program through the detection of single high p_T muons ($p_T > 20\text{GeV}/c$) resulting from Z^0 and $W^{\pm}$ decays produced in the collision of polarized protons.

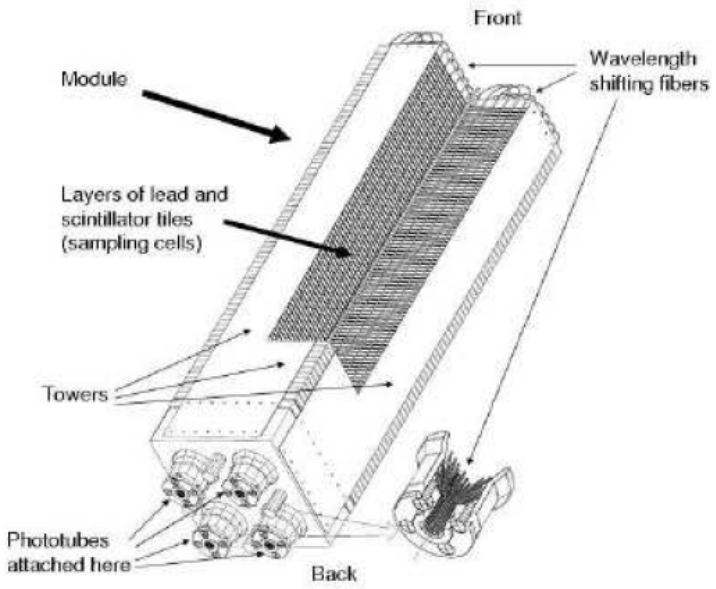

Figure 4.2 The layout of a PbSc module.

4.3.1 The Muon Magnets

The two PHENIX muon magnets house both the north and south Muon Tracker subsystems and use solenoid coils to produce radial magnetic fields. The muon magnets were designed in order to enclose the entire tracking chambers to maximize muon acceptance (full azimuth and approximately 25° in θ) while simultaneously minimizing the effect on the RHIC circulating beams. The magnetic field is reasonably uniform and is mapped to a precision of 1%. The radial magnetic field's integral is approximately proportional to the polar angle θ. Charged particles follow helical trajectories, moving in ϕ with approximately constant θ. The north muon magnet's position is fixed and covers the full length between the PHENIX central arm and the front of the Muon Identifier. The south muon magnet is 1.5m shorter and can be moved to allow access to the PHENIX central arm detectors. Both arms have similar $\int B \cdot dl$, but the additional length and flatter piston angle give the north muon magnet better theoretical acceptance. The muon magnet backplates, also referred to as magnet yokes, serve as the first

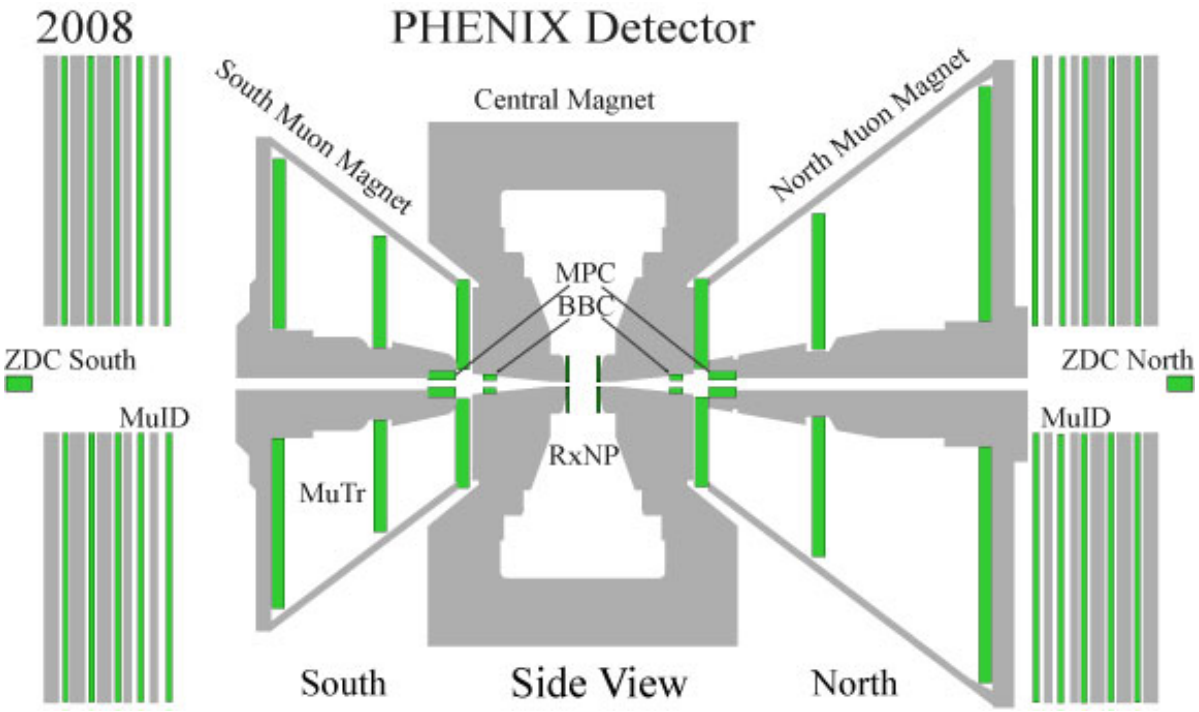

Figure 4.3 A side view for PHENIX forward/backward detectors in Run8.

absorber layer of the Muon Identifier and have a thickness of 30cm in the north arm and 20cm in the south arm. The front z locations of the north and south magnet backplates are 630cm and −480cm respectively.

Magnetic field maps for both the PHENIX central and muon magnets are conducted using a surface mapping method that provides a calculation of the magnetic field based on measurements performed at points on the surface of the magnet. Hall probes are used to measure several points along radial lines on the magnet's interior surface. The integral magnetic field strength $\int B \cdot dl$ along a line at 15° is 0.75 Tesla-meters in the south magnet and 0.72 Tesla-meters in the north magnet. In both arms the average transverse momentum kick from the magnets is 0.2GeV/c.

4.3.2 The Muon Tracker

The basic layout of the muon tracker is represented in Figure 4.4. Both the north and south muon tracking chambers consist of three stations of cathode strip chambers for measuring the

trajectory of particles in a magnetic field. The strength of the magnetic field is sufficient to permit momentum and charge sign determination. The MuTr stations are in the shape of octants, as seen in Figure 4.4, with the station number (1, 2 or 3) and diameter increasing with distance from the interaction point. The largest tracking station is station-3 with octant chambers about 2.4m wide and long.

The MuTr determines the momentum of charged particles in a standard fashion by combining the bend of a charged particle in a magnetic field and precise trajectory information using the basic principle provided in the Lorentz force law. The magnetic field in the MuTr volume is essentially radial and the particles traverse the volume at relatively low angles relative to the beam line of about 20°. For a charged particle entering, the magnetic field the component of the velocity parallel to the magnetic field is unaffected, while the component of the velocity perpendicular to the magnetic field will cause the particles motion to bend in the perpendicular direction. For this perpendicular component, the momentum of the particle is given by Eq. 4.1,

$$p = q \cdot B \cdot R \tag{4.1}$$

where q its charge, B the magnetic field strength, and R is the radius of the induced circular motion. As a charged particle passes through the MuTr volume, each of the tracking stations measures a position point along the particle's arc as it bends. A particle's momentum can be determined to the extent that both B and R are known. The MuTr essentially measures R in 3-dimensions in a high particle multiplicity environment.

Tracking stations 1 and 2 each contain 3 chamber "gaps", and station 3 contains 2 "gaps". Each chamber gap consists of two cathode planes on either side of an anode wire plane. The anode wires are instrumented in each half-octant, each covering a segment of ϕ acceptance. One plane of cathode strips runs radially (perpendicular to the anode wires), while the second plane has cathode strips at stereo angles that range between 0 and $\pm 11.25°$ relative to the perpendicular strips. The perpendicular cathode strips are capable of providing the highest resolution ϕ measurements. Each strip is 1cm wide, and the distribution of charge is fit across multiple strips, ultimately providing position resolution in the bend plane of about 100μm.

The stereo angle cathode strips provide crude two-dimensional resolution which aids in the rejection of false cathode strip hits, generally referred to as "ghost" hits. For the purposes of read out cathode strips serve as the most basic unit of the MuTr. The chambers are operated with a gas mixture that is 50% Ar, 30% CO_2, and 20% CF_4 and at a typical voltage of 1850V.

Table 4.1 MuTr gap positions. Distances are to the front of the gap.

Arm	**Station**	**Number of Gaps**	z **(cm)**	**Rad. Length %** X_0
North	1	3	180	< 10
North	2	3	347	< 0.1
North	3	2	612.5	< 10
South	1	3	-180	< 10
South	2	3	-300	< 0.1
South	3	2	-460	< 10

Except for the area lost due to the support structure, the MuTr stations have full azimuthal acceptance (ϕ), and a θ acceptance that ranges from 10° to 37°, which corresponds to $1.2 < |\eta| < 2.4$. Table 4.1 lists the positions of the different MuTr chambers and their relative radiation lengths. In order to measure the particle bend with maximum resolution, the amount of material in station-2 is minimized, with $\leq 0.1\%$ radiation length. The amount of material in all three MuTr stations amounts to about $0.2X_0$ (radiation lengths).

The MuTr chambers must contend with secondaries from the collision that can degrade the inherent 100μm resolution capability or even cause incorrect momentum determination. The impact of likely collision-related backgrounds on momentum determination has direct bearing the measurement of single hadrons and is discussed further in Chapter 6. Additional information and references concerning the design, construction, and electronics of the MuTr can be found in [16].

4.3.3 The Muon Identifier

Once a charged particles passes through the station-3 of the MuTr, it reaches the muon magnet backplate which serves as the first absorber layer of the MuID. Figure 4.3 shows the basic design of the MuID which has five alternating steel absorber (gray) and instrumented

sensitive (green) layers that permit the separation of muons from hadrons. The thickness of each absorber MuID layer is different as showin in Table 4.2. The choice of the total amount of steel absorber and the thickness of the absorber layers in the MuID was determined by two primary designs goals that address (1) restricting hadron contamination in the muon sample, and (2) the desire to measure low momentum muon pairs, for instance for meson detection.

Table 4.2 MuID gap positions. Front and back are defined relative to the interaction point at (0,0,0). The absorber width is for the preceding absorber layer.

Arm	**Gap**	**Front z (cm)**	**Back z (cm)**	**Absorber width (cm)**
North	0	686.96	704.24	30 (backplate)
North	1	728.46	745.74	10
North	2	768.76	786.04	10
North	3	815.86	833.14	20
North	4	861.36	878.64	20
South	0	−686.96	−704.24	20 (backplate)
South	1	−728.46	−745.74	10
South	2	−768.76	−786.04	10
South	3	−815.86	−833.14	20
South	4	−861.36	−878.64	20

Shortly after the first collisions were recorded in PHENIX, the occupancies observed in the MuID where approximately twice that expected from Monte Carlo (GEANT 3) simulations [17]. Investigation uncovered that the simulations were missing material. After this issue was resolved, it was determined that the primary source of the backgrounds observed in the MuID were particles emanating from the beam pipe at nearly perpendicular angles $7-9$m downstream from the collision vertex. In addition to this, another unexpected source of backgrounds was determined to be due to the beam "scraping" on the steering magnets inside the tunnel before entering the interaction region. This phenomenon deposits energy not from the direction of the collision vertex but from behind the detector. Improved beam steering and collimation, as well as the addition of steel shielding in the MuID square-hole (after RHIC Run2) and in the beam tunnel (after RHIC Run3) have alleviated but not completely removed both of these background sources.

4.3.4 The Muon Piston Calorimeter

The Muon Piston Calorimeter (MPC) is a pair of electromagnetic calorimeters built from $PbWO_4$ scintillating crystals and read out using avalanche photodiodes (APD) which sit in the north and south piston holes of the muon magnets of PHENIX. The acceptance in the south (north) is approximately $-3.7 < \eta < -3.1$ ($3.1 < \eta < 3.9$). The difference is due to a flange in bellows around the beam pipe in the south which is not present in the north. The absence allows one extra ring of towers in the north at high rapidity. The Run-8 configuration included 196 (220) towers in the South (North) MPC, and an improved gain monitoring system based on LED's and optical fibers. The MPC uses the similar electronics with the central-arm electromagnetic calorimeter. A picture of the south MPC is shown in Figure 4.5.

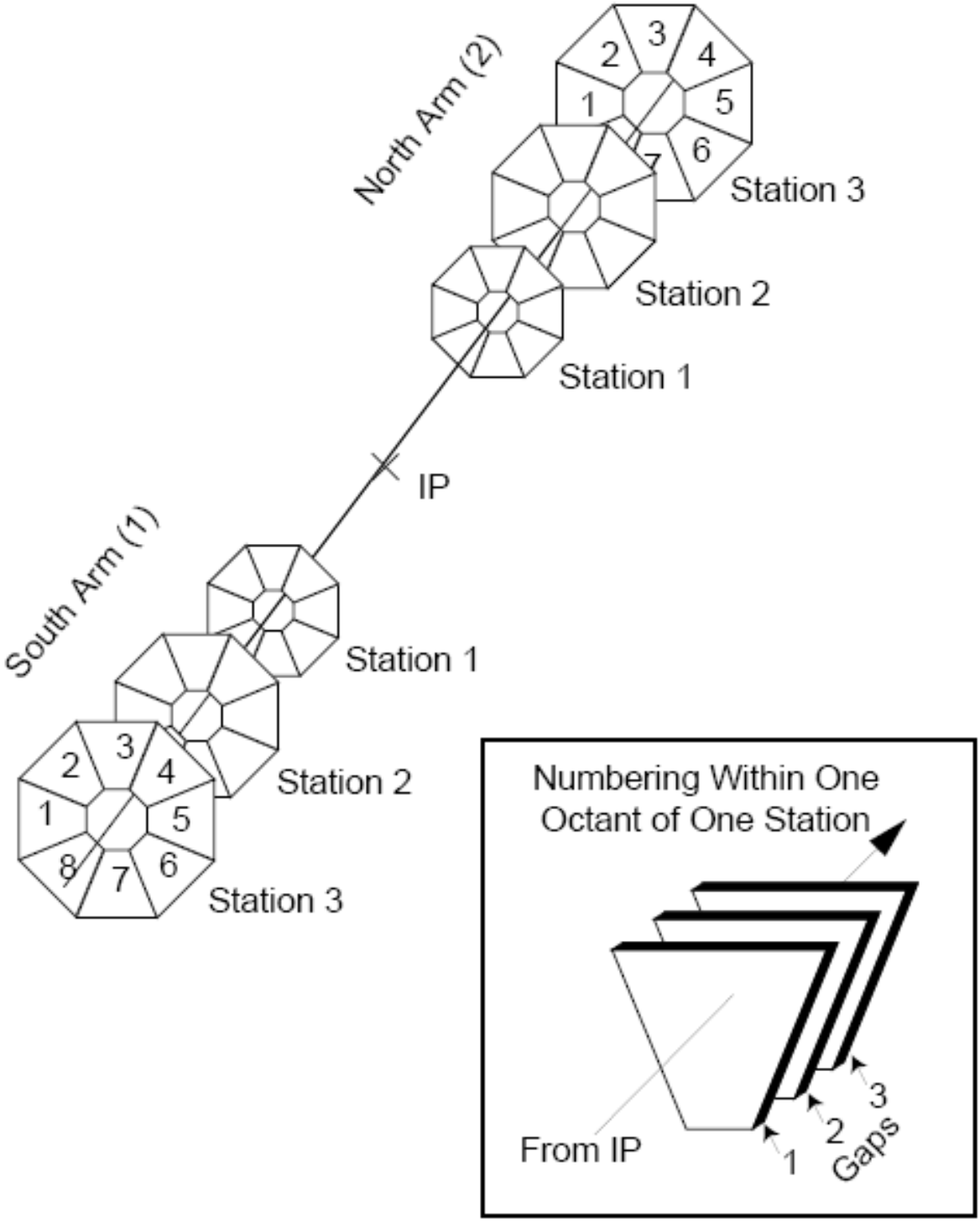

Figure 4.4 MuTR chamber description. Each MuTr station octant is actually instrumented in half octants (not depicted).

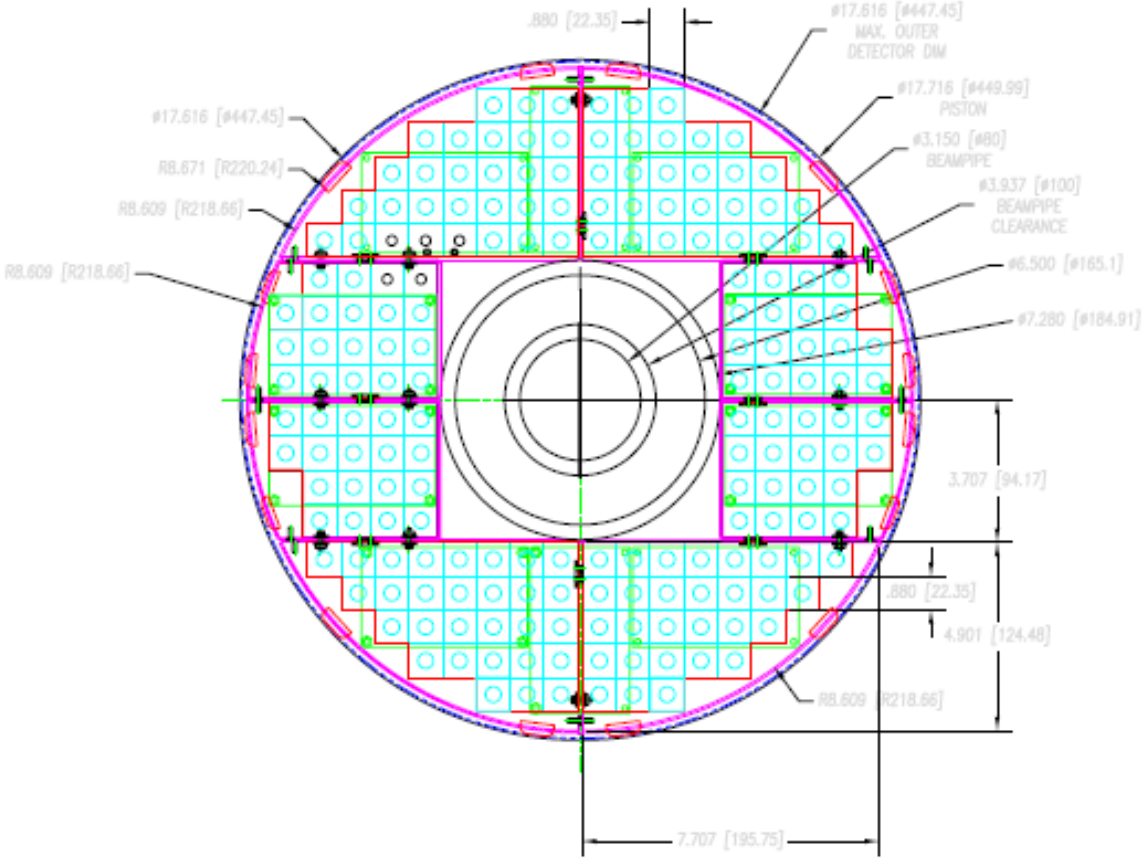

Figure 4.5 MPC South Mechanical Design and Tower Layout.

CHAPTER 5. Measurement Requirements

5.1 Measuring Single Spin Asymmetry A_N

As was written in Chapter 2, the single spin asymmetry can be defined as

$$A_N = \frac{\sigma^{\uparrow} - \sigma^{\downarrow}}{\sigma^{\uparrow} + \sigma^{\downarrow}} \tag{5.1}$$

In experiment, a cross section σ can be written as

$$\sigma = \frac{\frac{N}{\epsilon_{reco}\epsilon_{bias}\epsilon_{acc}}}{L} \tag{5.2}$$

where N is the measured yield which needs to be corrected for the efficiencies in reconstruction (ϵ_{reco}), trigger bias (ϵ_{bias}) and detector acceptance (ϵ_{acc}) and L is the luminosity.

Therefore, A_N can be written as

$$A_N = \frac{\sigma^{\uparrow} - \sigma^{\downarrow}}{\sigma^{\uparrow} + \sigma^{\downarrow}} \tag{5.3}$$

$$= \frac{\frac{\frac{N^{\uparrow}}{\epsilon^{\uparrow}_{reco}\epsilon^{\uparrow}_{bias}\epsilon^{\uparrow}_{acc}}}{L^{\uparrow}} - \frac{\frac{N^{\downarrow}}{\epsilon^{\downarrow}_{reco}\epsilon^{\downarrow}_{bias}\epsilon^{\downarrow}_{acc}}}{L^{\downarrow}}}{\frac{\frac{N^{\uparrow}}{\epsilon^{\uparrow}_{reco}\epsilon^{\uparrow}_{bias}\epsilon^{\uparrow}_{acc}}}{L^{\uparrow}} + \frac{\frac{N^{\downarrow}}{\epsilon^{\downarrow}_{reco}\epsilon^{\downarrow}_{bias}\epsilon^{\downarrow}_{acc}}}{L^{\downarrow}}} \tag{5.4}$$

The efficiencies in the measurement, $\epsilon^{\uparrow}$ and $\epsilon^{\downarrow}$, can be treated as spin independent quantities because RHIC polarized proton beams have alternate spin $\uparrow$ and $\downarrow$ patterns and PHENIX detectors collect the outgoing particles from spin $\uparrow$ and $\downarrow$ proton collisions in almost the same time (approximately 106ns crossing). In addition, it is impossible to reach 100% polarization for proton beams in the experiment and the measured asymmetries have to be scaled by the polarization of proton beams to obtain the real physical asymmetries. Thus, the Eq. 5.4 can be rewritten in a simpler form

$$A_N = \frac{1}{P}\frac{\frac{N^{\uparrow}}{L^{\uparrow}} - \frac{N^{\downarrow}}{L^{\downarrow}}}{\frac{N^{\uparrow}}{L^{\uparrow}} + \frac{N^{\downarrow}}{L^{\downarrow}}} \tag{5.5}$$

where P is the polarization of the proton beam at RHIC.

5.2 Relative Luminosity

Luminosity measured with a detector can be written as

$$L = \frac{N}{\sigma_{detector}} \tag{5.6}$$

where N is the number of $p+p$ collisions measured by the detector and $\sigma_{detector}$ is the inelastic $p+p$ cross section seen by the detector, which is defined as

$$\sigma_{detector} = \sigma_{inclusive}^{pp->X} \cdot \epsilon_{eff} \tag{5.7}$$

where $\sigma_{inclusive}^{pp->X}$ is the total inelastic $p+p$ cross section, and ϵ_{eff} is the efficiency of the detector. As discussed above, it can be treated as spin independent and needs to be checked.

If we assume the polarized cross section measured by the luminosity detector are also spin independent, the ratio of luminosities from spin $\uparrow$ and $\downarrow$ states, called relative luminosity (R), can be written as

$$R = \frac{L^{\uparrow}}{L^{\downarrow}} = \frac{N_{lumi}^{\uparrow}}{N_{lumi}^{\downarrow}} \tag{5.8}$$

where $N_{lumi}^{\uparrow}$ and $N_{lumi}^{\downarrow}$ are the number of spin $\uparrow$ and $\downarrow$ proton collisions measured by the luminosity detectors. In this case, the Eq. 5.5 can be rewritten as

$$A_N = \frac{1}{P}\frac{N^{\uparrow} - R \cdot N^{\downarrow}}{N^{\uparrow} + R \cdot N^{\downarrow}} \tag{5.9}$$

Besides relative luminsity formula, an alternative asymmetry calculation formula called "square root formula" is often used as shown in Eq. 5.10. It combines yields from spin $\uparrow$ and $\downarrow$ polarized bunches and from the left and right halves of the detector such that systematic errors are reduced. In particular, the acceptance and luminosity asymmetries cancel out to several orders.

$$A_N = \frac{1}{P\langle|cos(\phi)|\rangle}\frac{\sqrt{N_-^{\uparrow}N_+^{\downarrow}} - \sqrt{N_-^{\downarrow}N_+^{\uparrow}}}{\sqrt{N_-^{\uparrow}N_+^{\downarrow}} + \sqrt{N_-^{\downarrow}N_+^{\uparrow}}} \tag{5.10}$$

At PHENIX, the two main detectors, the BBCs and the ZDCs, can be used for luminosity measurements because they have high statistics, low background and sample between the $\pm$35cm z-vertex region which our asymmetry data sample is mainly from. The resolution of

the BBC is about 5cm, while the ZDC resolution is about 30cm. Therefore, the z-vertex region sampled by the BBCs much more accurately matches the actual offline z-vertex region used in the analysis (±35cm). In addition the level 1 trigger of BBC (BBCLL1) records about 40 times more events than ZDCLL1 trigger. Thus, the BBCs are used for measurements of luminosity, and the events from the ZDCs are used for systematic check.

5.2.1 Run8 Relative Luminosity

In order to study the systematic uncertainties in the assumption that σ_{BBC} is spin independent used to get Eq. 5.8, we need to compare the ZDC values of Relative Luminosity with those of the BBCs. Figure 5.1 shows the Relative Luminosity from BBCLL1 and ZDCLL1 triggered events by using only non-empty even, odd and all bunches respectively in Run8. Data for BBCLL1 and ZDCLL1 come from the GL1 boards that record the total number of triggers per beam crossing when the DAQ was live (able to take data) for up to four different triggers. The Global Level-1 trigger (GL1) is the part of the PHENIX online system that is responsible for generating triggers from the Local Level-1 (LL1) reduced bit data, coordinating busies, and managing partitioned running of the PHENIX detector.

5.2.2 Systematics of A_N from Relative Luminosity

Using standard error propagation on Eq. 5.9, the uncertainty in A_N due to the uncertainty in Relative Luminosity is found to be

$$\delta A_N(R) = \frac{1}{P}\frac{2N^{\uparrow}N^{\downarrow}}{(N^{\uparrow} + R \cdot N^{\downarrow})^2}\delta R \tag{5.11}$$

If the asymmetries are very small, where $N^{\uparrow} \approx RN^{\downarrow}$, the Eq. 5.11 can be approximately simplified as

$$\delta A_N(R) \approx \frac{1}{P}\frac{2R \cdot (N^{\downarrow})^2}{(2R \cdot N^{\downarrow})^2}\delta R = \frac{1}{P}\frac{\delta R}{2R} \tag{5.12}$$

Due to the high statistics of BBCs, the statistical uncertainties of $\frac{\delta R}{R}$ for an average fill is essentially very small ($\approx 10^{-5}$), which can be negligible. The two largest systematic sources of uncertainty are a possible asymmetry in the measured cross sections for different spin orientations

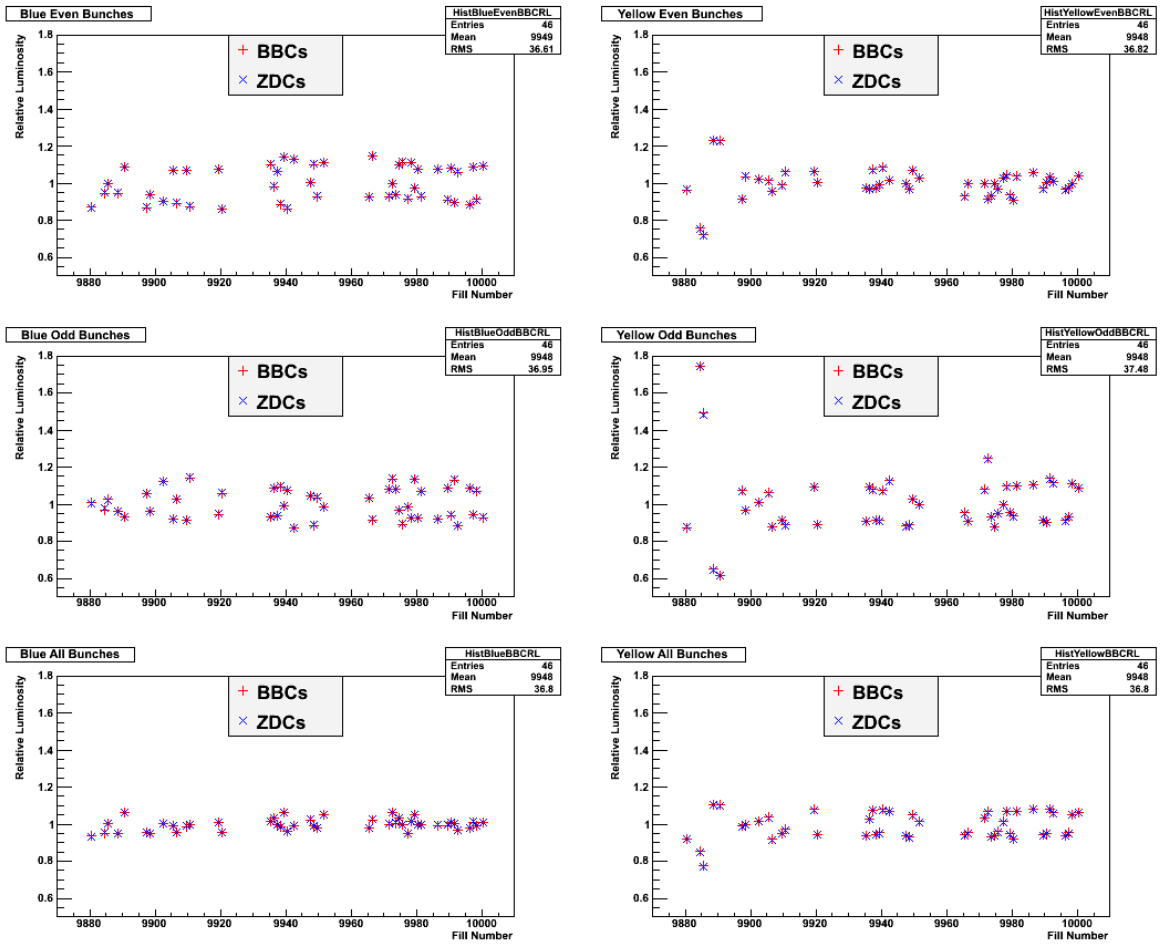

Figure 5.1 Relative Luminosity vs. fill number as measured by the BBCs and ZDCs in Run8.

and inaccurately measuring the total luminosity. As discussed above, luminosities measured by the ZDCLL1 trigger can be used to estimate the systematics. The systematic asymmetries of A_N from Relative Luminosities for both blue and yellow beams are $0.2\% \pm 0.015\%$ in Run8, however the signs of the asymmetries for blue and yellow beams happen to be opposite.

5.3 Polarization and Local Polarimetry

In order to calculate the real physical asymmetries, the polarizations of proton beams need to be measured. At RHIC, two separate polarimeters, the pC polarimeters and a polarized HJet polarimeter, are used to measure the magnitude of polarization. Both measurements

are made with vertically polarized protons, and exploit asymmetries in elastic scattering in the Coulomb-Nuclear Interference (CNI) region. The CNI region is defined as the energy range in elastic scattering in which the Coulomb and Nuclear forces are of the same strength, and therefore can interfere with each other, inducing a spin flip, observable as an asymmetry. Since both detectors were briefly described Chapter 3, here we only give results of polarizations measured fill by fill in Run6 and Run8.

For transversely polarized $p + p$ collisions in Run8, the spin direction for both blue and yellow beams was vertical. However, current MPC single clusters A_N analysis shows that the spin direction of blue beam is rotated about 18° from the vertical direction that the spin should be along. It may cause a significant underestimate of the measured asymmetries if this effect is not well corrected. Therefore, it is very important to check that the polarization direction is correct at PHENIX. A set of "local" polarimeters, composed of the ZDCs and SMDs, are used towards the objective. The official results of transverse polarization direction in Run8 measured by local polarimeter is shown in Table 5.1.

Table 5.1 Polarization directions from the Run8 transverse polarization running periods.

Beam	**Polarization Direction (radian)**
Blue	0.242 ± 0.030 (stat.) ± 0.111 (sys.)
Yellow	0.031 ± 0.048 (stat.) ± 0.114 (sys.)

CHAPTER 6. Single Transverse Spin Asymmetry of Forward Hadrons

6.1 Run Selection

The data acquisition system (DAQ) of PHENIX is limited to take up to 1 hour data although it can run as long as we like if no errors occur. This data-taking duration is call a "Run". In PHENIX, the name "Run" has two different meaning: (1) if it is followed by the calendar year number such as "Run2008" or "Run8", it means the whole year running. (2) if it is followed by the six digits ID such as "Run197450", it means the data-set taken in a certain time-duration (less than one hour). In the later chapters, this word "Run" always means the one-hour-run unless followed by the calendar year number.

One run is always manually started by the DAQ operator on shift, and it can be stopped automatically when one hour data-collecting is done or stopped manually in any abnormal situation.

It is very important to ensure that data used in analysis has a good quality. Thus a quality assurance (QA) study for each run is needed. Some real-time experiment parameters, such as magnetic field configuration, beam luminosity, level-one trigger rates, spin configuration, have important effects on the quality of data are recorded to an electronic log book. These parameters are measured between physical runs, using specific detector configurations, sometimes running exclusively and/or based on existing most recent physics data. Then they are used during the physical run by DAQ operator to maintain a uniform performance of detectors. This is called "online" calibration, contrary to the "offline" calibration later done to the reconstructed data. Each sub-system has a separate selection of runs of its own dataset. The "offline" run-by-run QA analysis in Run8 for MuTr and MuID was done by experts, see [62] for details.

In this analysis, the data samples are collected in PHENIX Run8 (2008) transverse polarized p+p collision at $\sqrt{s} = 200$GeV run256450 (2008/02/15) to run259576 (03/09/2009). According to the Run8 log book and the corresponding QA analysis[62], some runs are rejected by QA study as following reasons:

- Radial spin runs (because the spin orientation for most of runs in run8 are vertical)
- Spin Patterns are missing in Spin Database
- Remove the fill 9947 whose polarization for blue beam is not available
- Remove zero field runs
- Remove run without GL1p Scaler Counts
- Remove runs due to MuTr south station-2/3 octant-7/8 low voltage problem
- Remove runs due to run by run recalibration failed
- Remove low statistics fill
- Remove less than 8 minutes short-time runs
- MuTr FEM or HV bad channels

After removing those bad runs, the remaining good runs are shown in the list in Appendix A.

6.2 Event Selection

There are two requirements for any event used in the analysis as following:

- Trigger requirement: The event at the north (south) muon arm must be triggered by a coincidence between the MUIDLL1_N1H (MUIDLL1_S1H) trigger and a BBCLL1 trigger. The MUIDLL1_N1H and MUIDLL1_S1H triggers will be introduced below.

- z-vertex requirement: Offline reconstructed BBC z-vertex must be within ±35cm of the nominal interaction point (denoted as $|z_{BBC}| < 35$cm). The events $|z_{BBC}| > 35$cm are not used because (1) The collision vertices for them are too close to the magnetic pole tips sit at ±41cm; (2) The statistics is quite few. A lot of the central-arm analyses use $|z_{BBC}| < 30$cm because events within $30 < |z_{BBC}| < 35$cm see a limited central-arm acceptance and have higher background. However, events within $30 < |z_{BBC}| < 35$cm are still good from muon arms.

6.2.1 MUIDLL1 1H(One Hadron) triggers

Because the luminosity is always limited and the interesting physical events are usually rare, a number of triggers have been used to enhance the fraction of interesting events to be recorded. In PHENIX, there are two types of triggers: event triggers such as BBCLL1 and particle triggers such as MUIDLL1_N1H and MUIDLL1_S1H.

Data taken in muon arms is almost always triggered by the Level-1 muon triggers (denoted as MUIDLL1). There are three types of MUIDLL1 triggers: 1D (One Deep) trigger, 1S (One Shallow) trigger and 1H (One Hadron) trigger. Each of these triggers have two independent sets in north and south muon arms. Therefore the 1D trigger associated with north(south) arm is also called N1D(S1D) trigger, and they are similar for 1S and 1H triggers. The 1D triggers provide a data set of of events containing an enriched sample of tracks penetrating to gap 4 of the MuID, in which muons are dominant. The 1S trigger data set contains an enhanced sample of shallow penetrating tracks, defined to be gaps 2 and 3 in the MuID, in which hadrons should be dominant. Study of the flux of stopped hadrons in these shallow gaps allows for the estimation of the number of punch-through hadrons contaminating the sample of muon candidates in gap 4. However, it is very difficult to isolate hadrons from 1S trigger data sample. Therefore, newly designed 1H triggers were used since Run8 to replace 1S triggers, which provide cleaner hadrons data sample.

These MUIDLL1 triggers use combinations of hits in MuID layers, called symsets, to determine whether a trigger condition has been met. A symset as shown in Figure 6.1 is defined

for every (logical) MuID tube at gap 0 by projecting from a z-vertex of (0,0,0) through the gap 0 tube position to the gap 4 position. The corresponding symset is then those tubes that lie along the ray from gap 0 to gap 4 (corresponding to tubes 0-4B in the Figure 6.1). Due primarily to likely multiple scattering in absorber material and to a lesser extent z-vertices differing from z=0, the symset definition includes those tubes adjacent to the central symset tube row (rows A and C in the Figure 6.1).

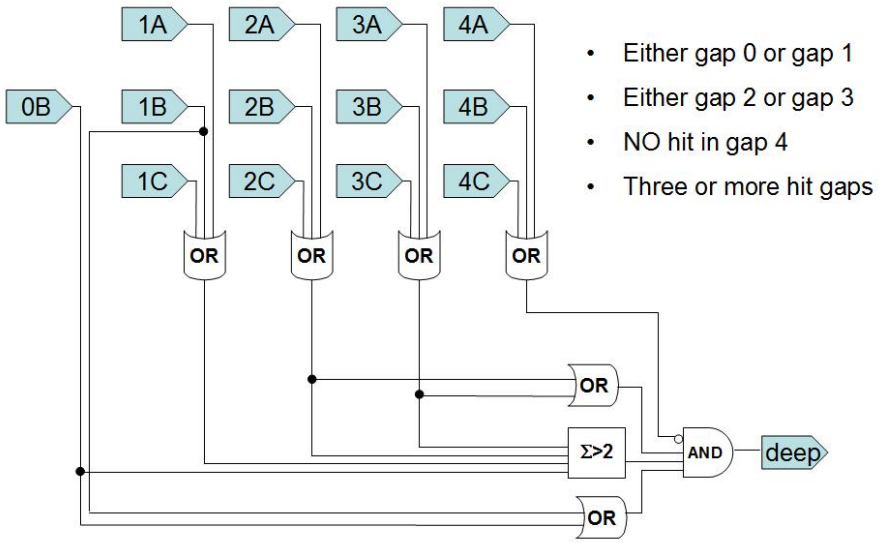

Figure 6.1 Local Level 1 Muon 1 Hadron trigger logic.

6.3 Track Reconstruction at Muon Arms

The current PHENIX muon arm software framework was developed in 2003 after the first two years of PHENIX operation. The tracking algorithm is written entirely in C++ and has been developed to cope with large hit multiplicity environments found in heavy ion collisions. With the reduced particle multiplicity and the corresponding detector occupancy in $p+p$ collisions, the same tracking algorithm is essentially applied in the $p+p$ case. The MuID and MuTr combine to form a "reconstructed" track in the muon arms, with composite information on: momentum, spatial position, penetration depth in the MuID steel, and collision vertex position (which also uses BBC information). This combination of hit information from two

separate subsystem detectors begins in the MuID.

6.3.1 MuID Road Reconstruction

For a given event the basic unit of the MuID detector readout used in the track reconstruction algorithm can be be either on or off which depends on having hit or not. Adjacent hits in the MuID are combined to form a cluster, and these clusters from MuID gaps can be combined for each tube orientation (horizontal or vertical) into a linear "roads" that can be projected back toward the collision vertex region. The algorithm starts from hits at Gap 1 and tries to form roads from hits that extend in both forward and backward directions in the MuID. There is no magnetic field in the MuID, and if ignoring the effects of multiple scattering, the path through the MuID steel layers is most likely a straight line. The one-dimensional roads are fit by using a straight line and then paired with roads of opposite orientation to form a two-dimensional MuID road. The two-dimensional MuID road contains the position and direction information from the MuID, which is included in the track reconstruction process.

Various conditions must be satisfied when pairing one-dimensional roads. To form a two-dimensional MuID road, the depth of the one-dimensional roads in opposite orientations can only differ less than one gap. Every one-dimensional road must contain hits in at least two gaps, and paired one-dimensional roads cannot differ in total hits by more than 2. The minimum depth allowed by a full MuID road is Gap 2, and it is not permitted for more than two gaps that lack hits preceding the last gap in the road. Under these various constraints, the gap depth of a full MuID road is determined by the deepest hit from paired one-dimensional roads. To reduce the combinatorial background in the next step of the muon arm reconstruction, the MuID roads seed the track finding algorithm for the MuTr.

6.3.2 MuTr Track Reconstruction

A cathode strip is the most basic unit of the MuTr. It will "fire" if enough ionization charge is deposited when a charged particle passes through the detector. A single particle usually fires $1-3$ adjacent cathode strips, which are combined to be a MuTr cluster. For high occupancy

events it is possible that two particles will fire cathode strips. In this case, it could lead to overlapping clusters. MuTr gap coordinates are derived from sets of fired cathode strips from a particular MuTr gap. Since the cathode strips are oriented at stereo angles to one another, two cathode strips within a gap can provide a two-dimensional position information. As we discussed in Chapter 4, MuTr station 1 and 2 have three gaps, and Mutr station 3 contains two gaps. These gaps are separated by just a few centimeters. Coordinates from each gap within a MuTr station corresponding to the two or three space points over the few centimeters of thickness of a particular MuTr station. Once these space points are fit with a straight line, they are called as MuTr stubs.

The MuTr track finding algorithm begins by attempting to match MuTr Station 3 stubs with all potential roads at the MuID Gap 0. If a match between a MuID road and MuTr station 3 stub is made, the algorithm will try to proceed to MuTr stations 2 and 1. Once the track has been formed from stubs of the three stations, the matched MuTr track and MuID road now possess all available information from the muon arm. Finally, the MuTr tracks are projected through the absorber to obtain the position and momentum information of the particle at the collision point. Figure 6.2 shows an example of muon arm reconstruction event display. The individual gaps within a particular MuTr station are too close together to be properly displayed in this figure.

6.4 Single Hadron Track Selection

As Figure 6.3 shows, the initial flux of hadrons are largest source of particles that are produced during collision and fly toward muon arms. The types of hadrons include but are not limited to $\pi^{\pm}$, $K^{\pm}$, K^0_s, K^0_L, p and $\bar{p}$, in which $\pi^{\pm}$ are dominant ($\approx 99\%$). Due to the significant amount of absorber material, more than 99% of the light hadrons reach the first absorber without decaying and are absorbed since the decay lengths ($c\tau$) of π's (780 cm) and K's (371 cm) very long compared to the flight path from the collision vertex to the first absorber material in the muon arm at $z = 41$ cm. And then first three layers of MuID absorber plates also stop many hadrons, so that only roughly 0.1% hardrons survive and hit MuID Gap

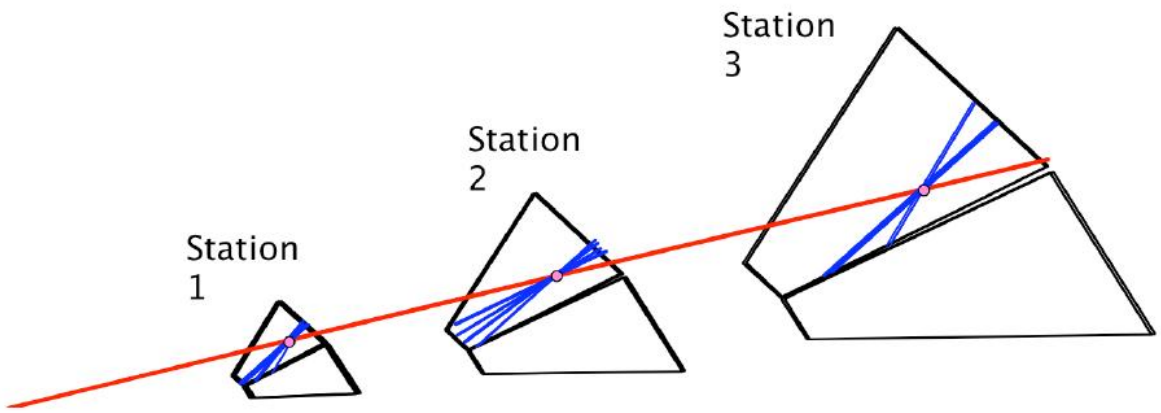

Figure 6.2 An event display for a single MuTr octant showing fired cathode strips (blue lines), MuTr stubs (pink circles), and a reconstructed MuTr track (red line). Each octant is instrumented as two half-octants.

2 and 3.

In general, there are three ways for a hadron to result in a track measured in muon arms.

- Decay into a muon before absorber, then the muon is measured in muon tracker, it is called hadron-decay-muon.
- Have only energy loss (Bethe-Bloch dE/dx) all the way through absorber, then measured in muon tracker, this is called a punch-through hadron or primary hadron.
- Produce hadronic showers in absorber, then the secondary particle from the showers are measured in muon tracker. This is called a secondary hadron.

Therefore, the hadron-decay-muons are taken as background. The secondary hadrons may not carry correct momentum and charge information and are possible to cause the dilution of asymmetries. In order to remove or suppress those types of hadrons, a Monte-Carlo simulation was required to find out optimal cuts. We will talk about the detailed simulation in next section.

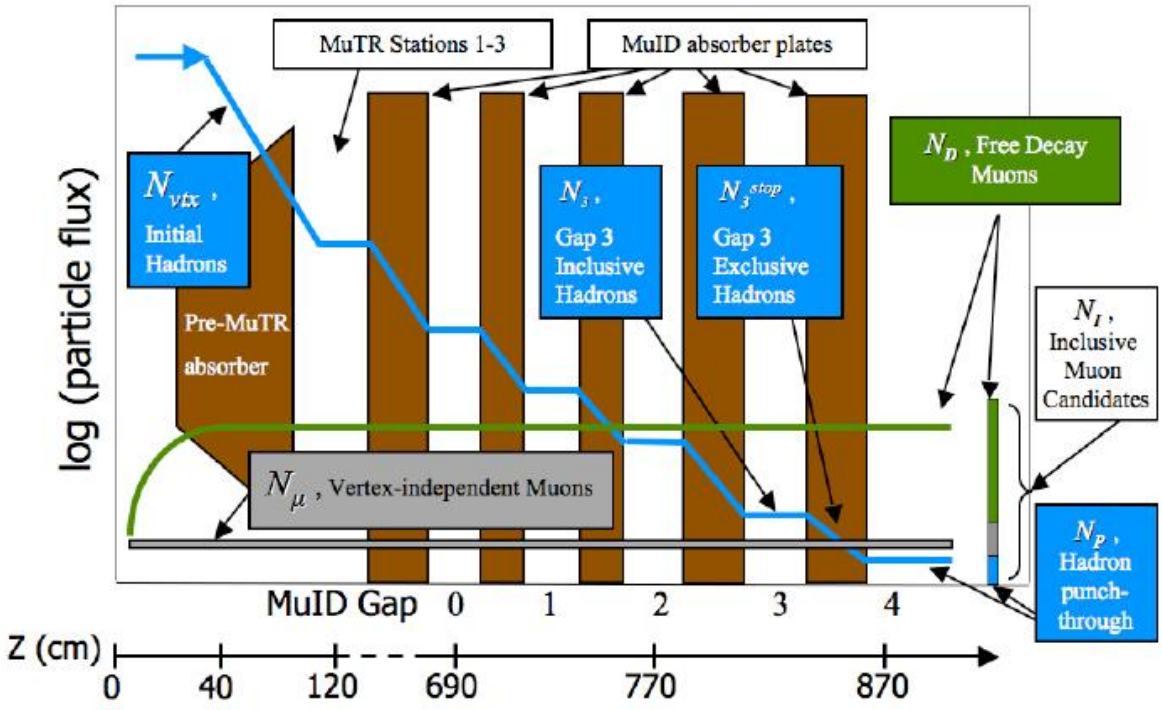

Figure 6.3 Schematic depiction of the relative flux of particles in the muon arm as a function of distance from the collision point.

6.5 Simulation

There are two levels for the simulation in PHENIX, PHPythia and PISA. PHPythia (PHENIX Pythia) is originated from Pythia which is a program for generation fo high-energy nuclear/particle physics events, i.e. for the description of collisions at high energies between elementary particles such as $e^{\pm}$, p and $\bar{p}$ in various combinations. Pythia contains theory and models from a number of physics aspects, including hard and soft interactions, parton distributions, initial-state and final-state parton showers, multiple interactions, fragmentation and decay. PHPythia generates events using Pythia within the friendly Fun4All framework. The primary advantage of using PHPythia is that the output is a Fun4All file, so that you can read the output phpythia.root file along with the simDST.root file. This makes it very easy to associate the original Monte-Carlo information with the data in the simulated DST.

PISA (PHENIX Integrated Simulation Application) is the PHENIX simulation software

package base on the GEANT3 libraries. The GEANT program decribes the passage of elementary particles through matters. GEANT3 is the third version of GEANT and the latest version is GEANT4. The output of the PISA package is a so-called "hits file" which is processed by software which runs in the Fun4All offline system. The first stage in the processing is the detector response modules for all the detector subsystems. In the detector response module software information obtained from the GEANT particle tracking through each detector subsystem is converted into simulated detector signals. The simulated signals are much like the real detector signals which appears on the real data PRDF's obtained by the online system which the PHENIX experiment is taking data. Thereafter, these simulated detector signals are processed by the same software which reconstructs the real data files into useful physics information suitable for analysis software.

6.5.1 PHPythia Simulation

The stardard code of PHPythia is available in the PHENIX CVS library. It can be checked out and modified to generate events according to physical process we are interested in. The PHPythia can fully simulate $p + p$ events with the full complement of observed final states particles. In this simulation, we only turn on the "$2 \rightarrow 2$" semi-hard QCD process where the "2" on the left side of "$\rightarrow$" means two incoming partons and the "2" on the right side of "$\rightarrow$" menas two outgoing partons. In $\sqrt{s} = 200$GeV $p + p$ collisions, the "$2 \rightarrow 2$" semi-hard QCD process include six sub-processes as shown in the Table 6.1. Obviously, the subprocesses of (4) and (6) are dominant ones.

After running PHPythia code with appropriate configuration, a number of events are generated and written into output file. By reading the output file, we find that there are predominantly three types of charged hadrons: $\pi^{\pm}$ ($\approx 85\%$), $K^{\pm}$ ($\approx 10\%$) and proton/anti-proton ($\approx 5\%$) as Figure 6.4 shown. Those hadrons generated from PHPythia (before absorbers) would be used as input hadrons for PISA simulation in next step.

Table 6.1 The sub-processes are included in the "$2 \to 2$" semi-hard QCD process. q ($\bar{q}$) represents quark(anti-quark) and g represents gluon.

Subprocesses	**Fractions in the "$2 \to 2$" semi-hard QCD process (%)**
(1) $q + q' \to q + q'$	$\approx 6.4\%$
(2) $q + \bar{q} \to q' + \bar{q}'$	$\approx 0.1\%$
(3) $q + \bar{q} \to g + g$	$\approx 0.1\%$
(4) $q + g \to q + g$	$\approx 43.5\%$
(5) $g + g \to q + \bar{q}$	$\approx 13.2\%$
(6) $g + g \to g + g$	$\approx 48.5\%$

6.5.2 PISA Simulation

The PISA package is also available in the PHENIX CVS library and is ready for users to check out. Running PISA is the most time-consuming step in the whole simulation. The configuration file "pisa.kumac" has almost all of the GEANT and PHENIX subsystem configuration options. Users can change which detectors are installed or turned on/off, the magnetic field map and its strength or polarity, tracking options etc. In order to save time, only detectors corresponding to the analysis should be turned on and other unused detectors need to be turned off, but the material of those detectors is still present in the simulation.

There are two packages to describe the hadronic showers in matter which are available to the users of GEANT3: GHEISHA and FLUKA. The GHEISHA code generates hadronic interactions with the nuclei of the current tracking medium, evaluating cross-sections and sampling the final state multiplicity and kinematics, while the GEANT philosophy is preserved for the tracking. FLUKA is a standalone code which is developed by the INFN-CERN Collaboration. Only a few parts of FLUKA have been included into GEANT3 which deal with hadronic elastic and inelastic interactions. The results of simulation by using GHEISHA will be a little different from those by using FLUKA in the treatment of positive and negative charged hadrons. In order to find out which one is relatively closer to PHENIX measurements, we plotted the ratio of positive and negative charged hadrons on momentum spectra for both GHEISHA and FLUKA simulation and compare them with our real data as Figure 6.5 shown. From the figure, it is easy to see that the momentum spectra from FLUKA simulation match the spectra from

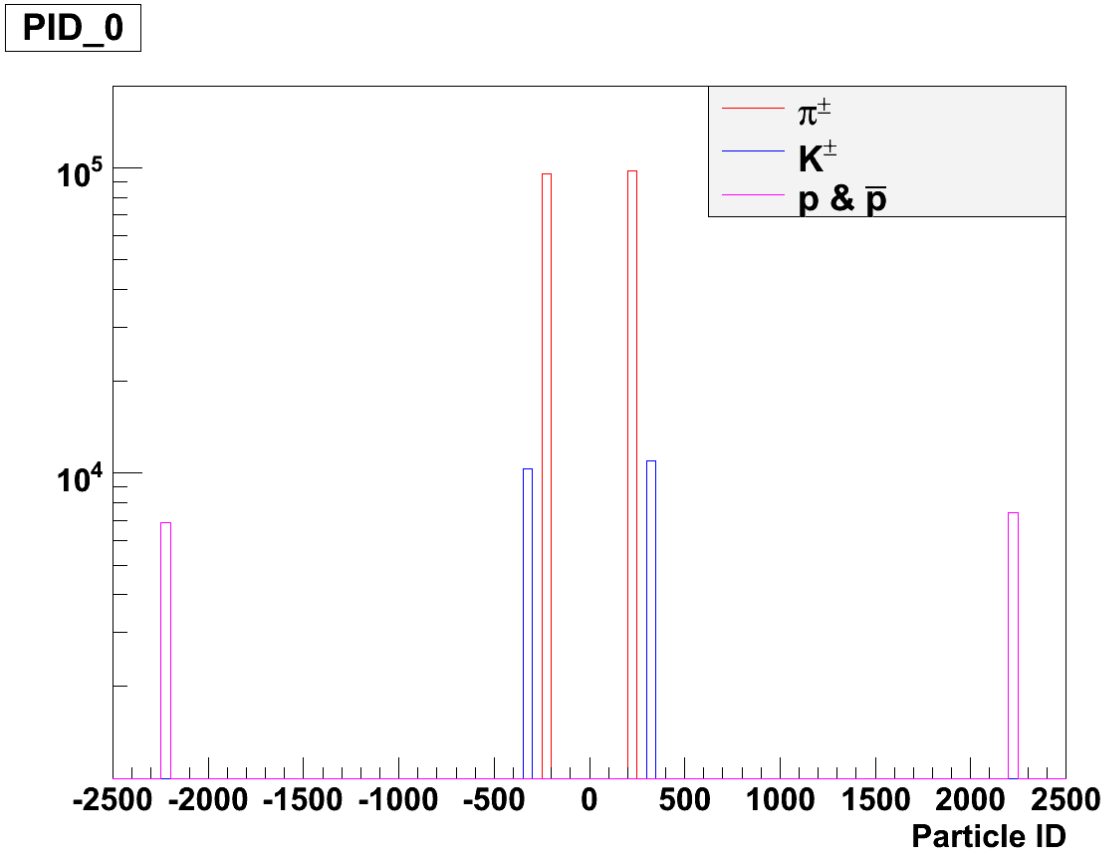

Figure 6.4 The particle ID of final-state charged hadron from Pythia where positive PIDs represent positive charged hadrons such as π^+, K^+ and proton, negative PIDs represent negative charged hadrons such as π^-, K^- and anti-proton.

real data better on both north and south muon arms. Therefore, FLUKA was chosen to be used in our simulation.

6.5.3 Muon Background

Altough hadron triggers have been used to sample the events, lots of hadron-decay-muons are still included in the data. These hadron-decay-muons are mainly from the decay of light mesons such as pions and kaons before these mesons hit into absorbers. Due to their high penetrating power, the muons that stopped at MuID Gap 2 or Gap 3 are assumed to be very low momenta ones. In the simulation, we can easily isolate muons from hadron tracks and plot their spectra as Figure 6.6 shown. It is clear that muons are dominant in low momentum

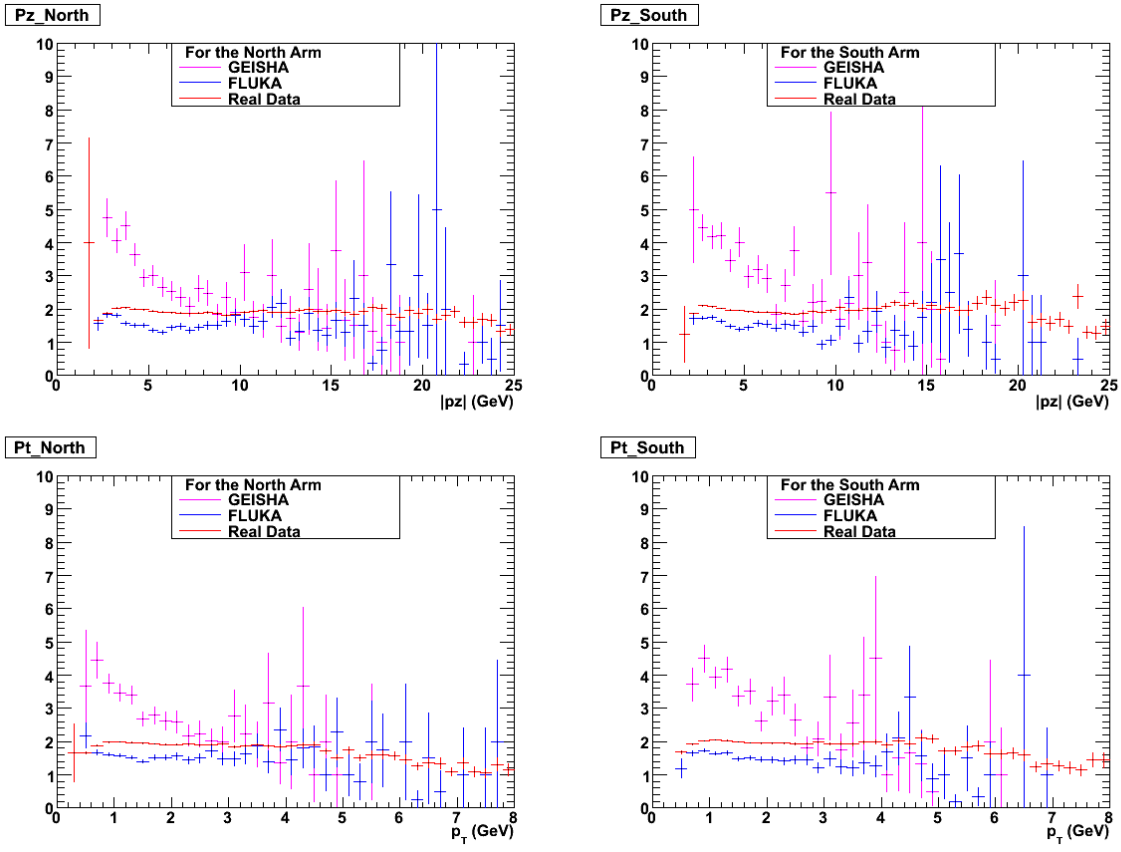

Figure 6.5 The p_T and p_z spectra of the ratio of positive hadrons and negative hadrons for FLUKA simulation, GEISHA simulation and real data.

region and can be removed by appropriate momentum cuts. We can use either momentum at vertex (p_{vtx}) cuts or momentum at MuTr station 1 (p_{st1}) cuts. In this simulation, p_{st1} cuts are used because "good enough" purity can be achieved by removing a little less statistics. Figure 6.6 shows the the spectra of p_{st1} before cuts and after cuts. We can clearly see that muon backgrounds have been removed effectively by the cuts.

6.5.4 Primary and Secondary Hadrons

Most muon background has been removed after applying momentum cuts, only primary and secondary hadrons are left in the data sample. In the simulation, we can distinguish primary hadrons from secondary hadrons, and know the location secondary hadrons are produced at,

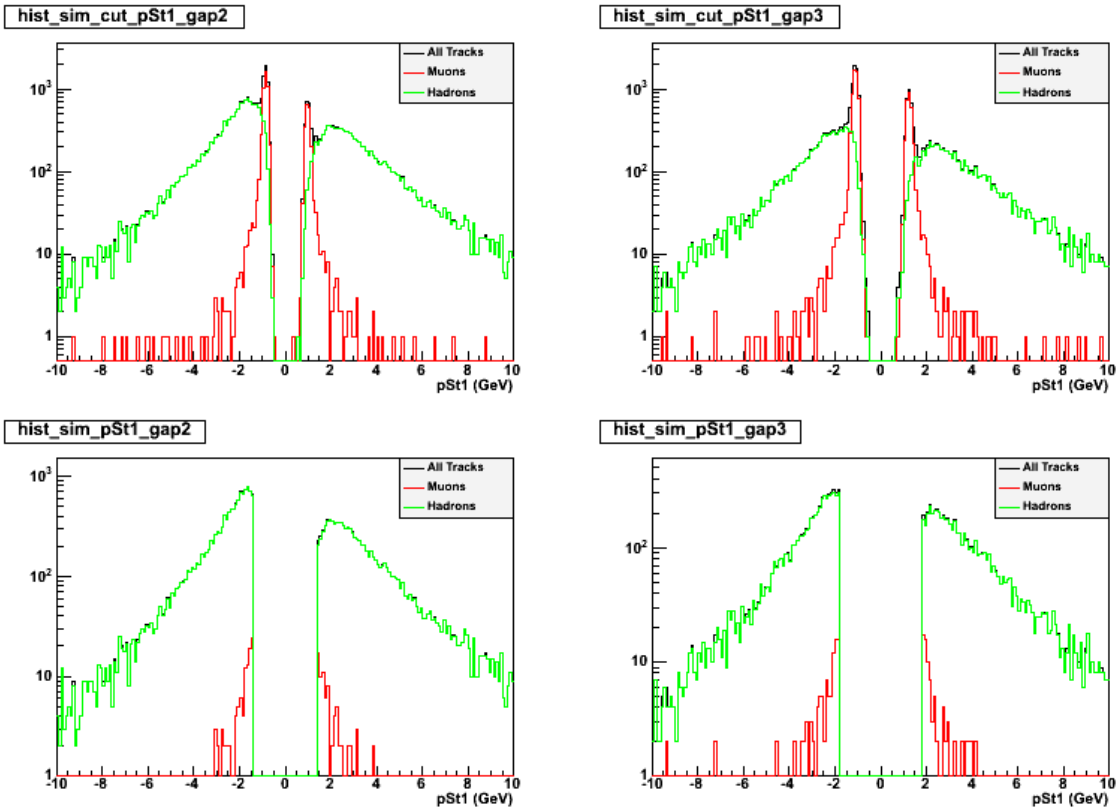

Figure 6.6 The p_{st1} distribution for all tracks, muon and hadrons before (top 2 plots) and after (bottom 2 plots) p_{st1} cuts for north ($p_{st1} > 0$) and south ($p_{st1} < 0$) arms, gap2 (left 2 plots) and gap3 (right 2 plots).

their parent and grandparent hadrons' momenta information. Primary hadrons don't have parents and grandparents, so in the discussion that follows when we refer to the parent or grandparent of a primary hadron it is understood that we are referring to the primary hadron itself. Similarly, if secondary hadrons have parents but don't have grandparents, we set their grandparents to be same with their parents. Figure 6.7 shows that primary hadrons are all produced at collision vertex around $z = 0$, while secondary hadrons are mostly produced in absorber area $41 < |z| < 140$cm. Figure 6.8 shows that some secondary hadrons' parents are generated from vertex but a lot of them are still not. In Figure 6.9, we can see that almost all of hadrons' grandparents are produced from vertex $z = 0$ which should originate from collision and not from hadronic shower. Therefore, we only need to consider at most two generations in

order to determine the origin of charged hadrons in the muon arms. By studying the difference between secondary hadrons and their grandparents, we can analyze how much they affect the real physical asymmetries when they can not fully removed.

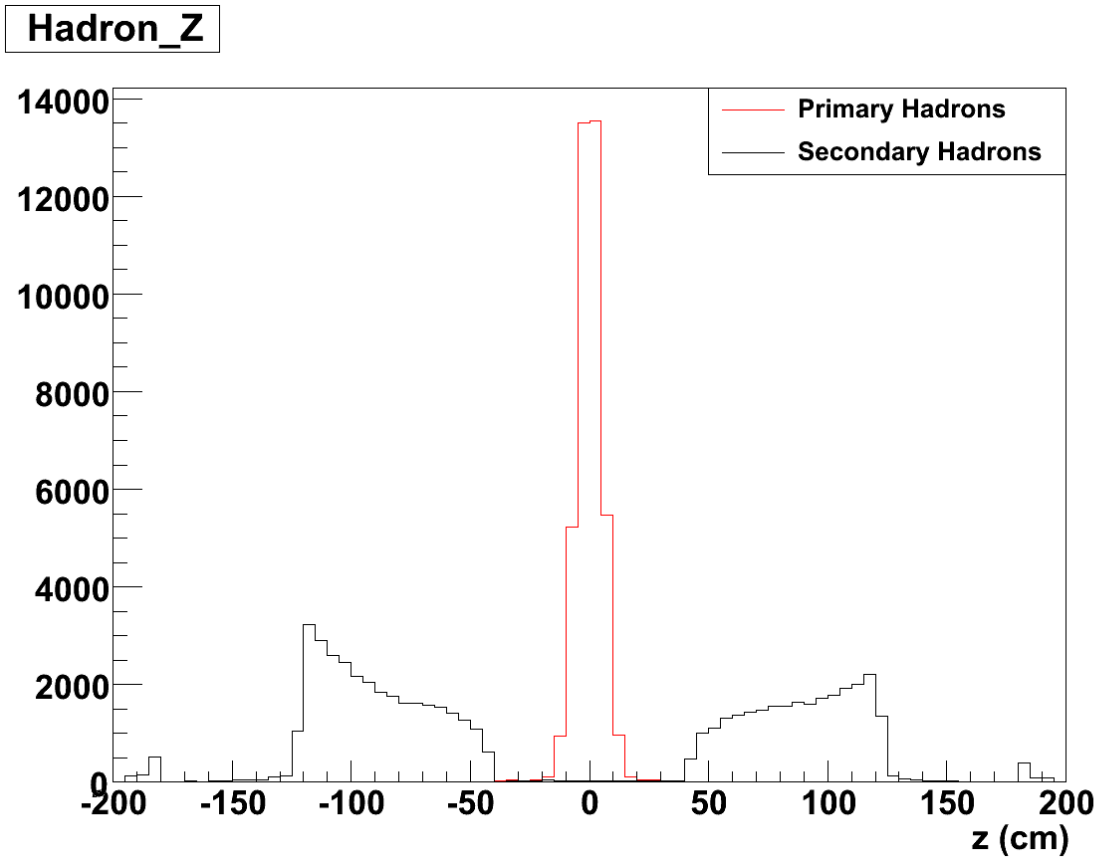

Figure 6.7 The origion location distribution for primary (in red) and secondary hadrons (in black) at both north ($z > 0$) and south ($z < 0$) muon arms.

In order to remove the secondary hadron background, we need to consider hadrons' interaction with absorber. When hadrons punch through the absorber and suffer ionization energy loss, the interaction between the hadrons and media is mainly elastic scattering on electrons, the direction of the hadrons should change very little. On the other hand, when hadrons scatter on a nucleus inelastically and cause hadronic showers, the direction of secondary hadrons (from the showers) can be very different from the primary hadrons (before the showers). It potentially gives us some ideas on separating secondary hadrons from primary

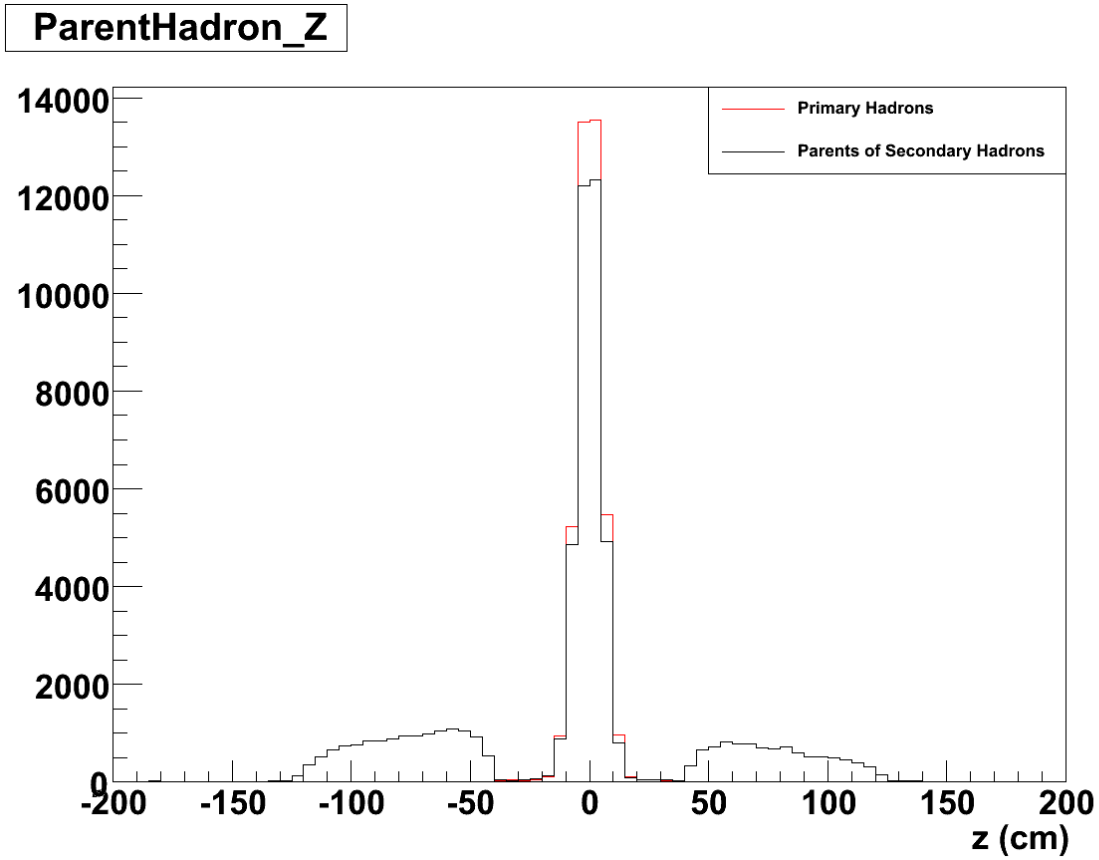

Figure 6.8 The origion location distribution for primary hadrons (in red) and parents of secondary hadrons (in black) at both north ($z > 0$) and south ($z < 0$) muon arms.

hadrons. Therefore, as Figure 6.10 shows, we can calculate the angle θ_{xp} between $\vec{p}_{vtx}$ and $\vec{p}_{st1}$. If θ_{xp} is larger enough for a particular hadron track, the hadron is more likely to be secondary hadron. However, in PHENIX there is no momentum measurement before absorber, $\vec{p}_{vtx}$ is actually reconstructed by using the BBC collision vertex and measurement points in MuTr. The smearing of collision vertex makes reconstructed $\vec{p}_{vtx}$ not very accurate. And, there is a momentum dependence on using θ_{xp} to separating secondary hadrons. Therefore, we use $p\theta_{xp}$ as the cut where $p = \frac{p_{vtx}+p_{st1}}{2}$. Table 6.2 shows the comparison between before and after the $p\theta_{xp}$ cut for percentage of secondary hadrons. We can see that the $p\theta_{xp}$ cut remove some secondary hadron background but lots of secondary hadrons still exist in data.

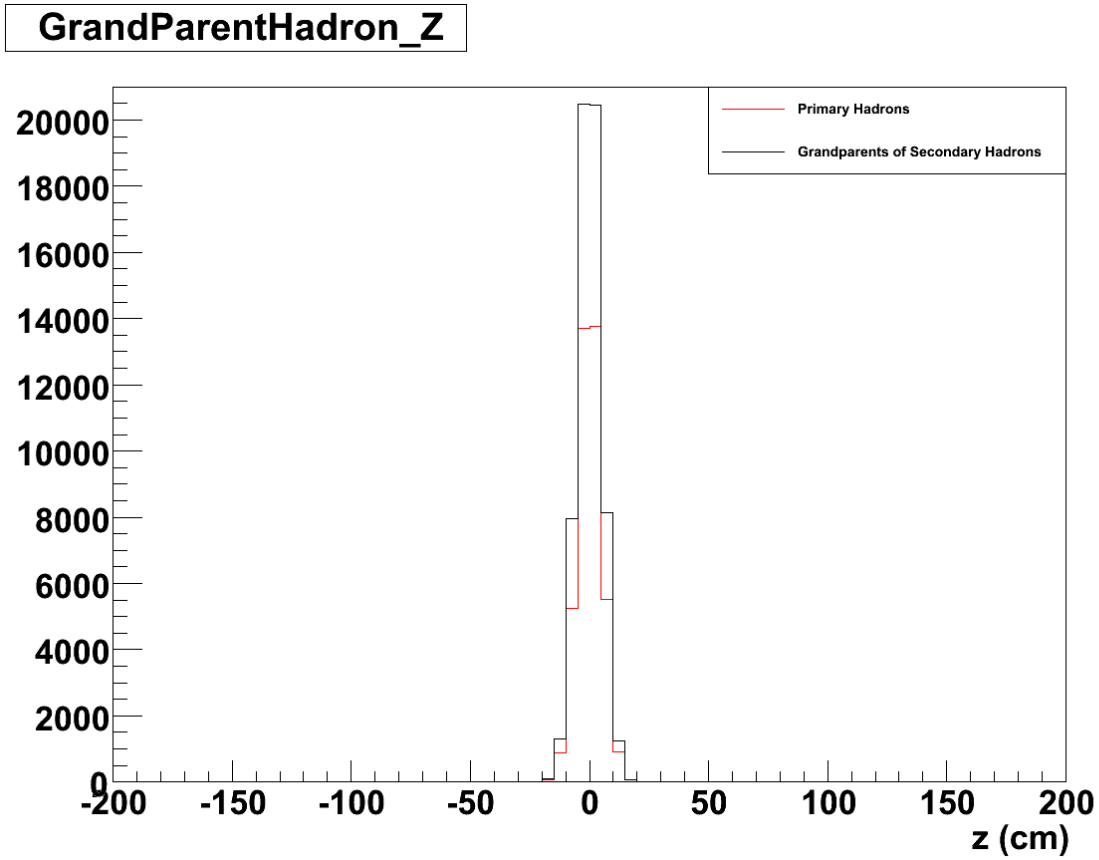

Figure 6.9 The origin location distribution for primary hadrons (in red) and grandparents of secondary hadrons (in black) at both north ($z > 0$) and south ($z < 0$) arms.

6.5.5 Asymmetry Mixing/Dilution Fractions

As discussed before, the secondary hadron can not fully removed by the $p\theta_{xp}$ cut and there is always a big smearing for the measured momentum comparing to the grandparent hadrons. We have to study how these effects affect the measurement of physical asymmetries. The polarization for both blue and yellow proton beams in Run 8 is along y direction in PHENIX coordinate, so the x component of momentum p_x is sensitive to the left-right asymmetry. Since we calculate the left-right asymmetry (the definition is given in next section) in the analysis, there are several reasons which could cause a mixing of particles on our sample that will either dilute the asymmetries that we measure, or mix the asymmetries of different hadrons as following:

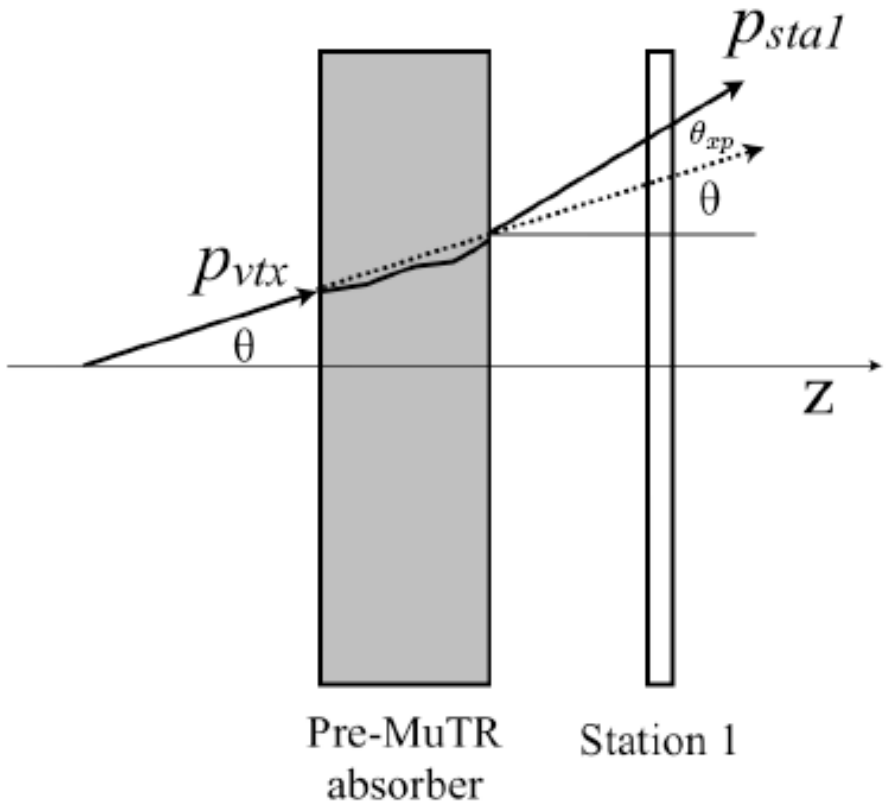

Figure 6.10 The definition of θ_{xp}

1. For particles that come from secondary interactions, the measured p_x may change sign when compared to their parents of grandparents. Thus, even if the polarization information is retained, this effect could dilute the asymmetry.

2. The charge of a secondary hadron changes sign when compared to its parent or grandparent when it is produced in an interaction in the absorber, i.e. in the hadronic shower K^+ produce a π^- which is measured. This could mix the asymmetries for positive and negative hadrons.

3. The measured charge of a hadron is incorrectly assigned when the track is reconstructed in the MuTr. This could mix the asymmetries for positive and negative hadrons, and can affect both primary and secondary hadrons.

4. The measured x_F and p_T of secondary hadrons may be different from their parents' or

Table 6.2 The percentage of primary hadrons existing in simulated data sample before and after $p\theta_{xp}$ cut in various x_F and p_T bins.

x_F	**No Cut**	$p\theta_{xp} < 0.2$	p_T **(GeV)**	**No Cut**	$p\theta_{xp} < 0.2$
< 0.06	34.8%	50.8%	< 2	40.0%	51.3%
$0.06 - 0.1$	40.8%	47.8%	$2 - 3$	42.0%	47.3%
$0.1 - 0.15$	40.8%	50.7%	$3 - 4$	43.9%	48.1%
$0.15 - 0.2$	39.8%	53.3%	$4 - 6$	39.5%	52.4%

grandparents' original momentum. This could mix the asymmetries for different x_F and p_T bins.

Table 6.3 The asymmetry mixing/dilution fractions from simulation in various x_F and p_T bins. These fractions are relative to the full data sample (both primary and secondary hadrons).

x_F/p_T (GeV)	p_x change sign		Charge change sign		Charge misidentified	
	h^+	h^-	h^+	h^-	h^+	h^-
$x_F < 0.06$	3.1%	3.1%	8.5%	9.1%	0.2%	0.6%
$0.06 < x_F < 0.1$	2.4%	2.1%	3.7%	4.8%	0.6%	1.7%
$0.1 < x_F < 0.15$	1.8%	1.9%	2.7%	6.1%	1.6%	4.5%
$0.15 < x_F < 0.2$	3.1%	1.7%	5.3%	14.6%	4.2%	13.9%
$p_T < 2$	3.1%	3.1%	8.2%	8.8%	0.2%	0.7%
$2 < p_T < 3$	1.9%	1.4%	3.2%	4.4%	0.7%	1.9%
$3 < p_T < 4$	1.2%	1.5%	2.4%	7.1%	1.5%	6.4%
$4 < p_T < 6$	2.3%	2.5%	5.4%	16.2%	4.2%	14.9%

We can only estimate how big mixing or dilution effects (1), (2) and (3) are from simulation. We may extract the real yields from measured yields by applying correction for the effect (4), which will be discussed in the next subsection. Of the first three effects, (1) and (2) are important for secondary hadrons, and (3) is a systematic effect for all hadrons. Assuming the three mixing/dilution fractions are independent of each other, we can estimate the combined asymmetry mixing/dilution fractions by

$$M_{combined} = 1 - (1 - M_1) \cdot (1 - M_2) \cdot (1 - M_3) \tag{6.1}$$

where $M_{combined}$ means the combined asymmetry mixing/dilution fractions, M_1, M_2 and M_3 are asymmetry mixing/dilution fractions for above three reasons. The results for the combined

asymmetry mixing/dilution fractions are shown in Table 6.4.

Table 6.4 The estimation of combined asymmetry mixing factors in various x_F and p_T bins.

x_F/p_T (GeV)	h^+	h^-
$x_F < 0.06$	11.5%	12.4%
$0.06 < x_F < 0.1$	6.6%	8.4%
$0.1 < x_F < 0.15$	6.0%	12.0%
$0.15 < x_F < 0.2$	12.1%	27.7%
$p_T < 2$	11.2%	12.2%
$2 < p_T < 3$	5.7%	7.5%
$3 < p_T < 4$	5.0%	14.3%
$4 < p_T < 6$	11.5%	30.5%

6.5.6 The Correction For Bin Sharing Effect

The measured hadron track momenta could be very different from the real track momenta. A high momentum track can be recontructed to be low momentum and more often a low momentum track can be reconstructed to be a fake high momentum track. Thus they can cause bin sharing effects as shown in Figure 6.11− 6.18. In this simulation, we generate 50 times more statistics in high x_F and p_T regions than low x_F and p_T regions in order to save time. In these Figures, the spikes on the right bottom plots are scaled events from low x_F and p_T regions.

These bin sharing effects can be corrected by matrices since we can know the correlations between measured spectra and real spectra for all charged hadrons from the simulation. We are going to discuss this method in a general case as follows.

Define $N(p_T, x_F)$ as the number of hadrons in certain p_T and x_F by assuming that smearing of p_T and x_F is independent of spin. Since measured p_T and x_F of hadrons are different from real p_T and x_F of hadrons, $N^R(p_T, x_F) \neq N^M(p_T, x_F)$ where the superscript R means "real", M means "measured". We divide $N^R(p_T, x_F)$ into n $p_T(x_F)$ bins $N_1^R \cdots N_n^R$, $N^M(p_T, x_F)$ into the same bins $N_1^M \cdots N_n^M$. Then we can have the correlation as

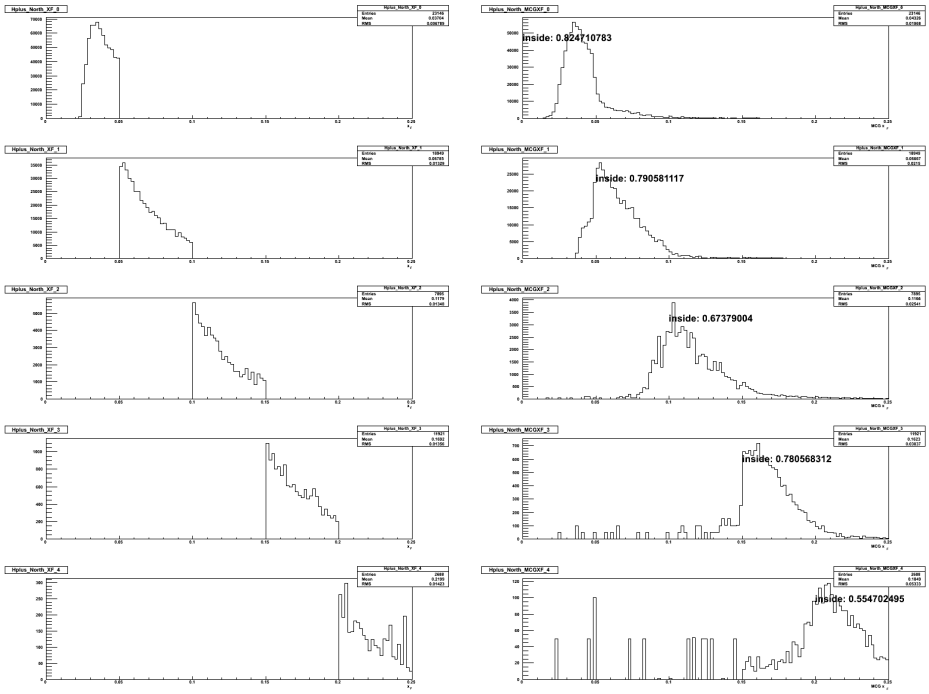

Figure 6.11 The x_F (p_z) smearing effects for positive charged hadrons at the north arm from the Monte-Carlo simulation. The left five plots are x_F (p_z) spectra for measured hadrons. The right five plots are x_F (p_z) spectra for hadrons from collision. The numbers on the right five plots are the fractions of measured hadrons from the same x_F (p_z) bin with hadrons really from collision.

$$\begin{pmatrix} N_1^R \\ \vdots \\ \vdots \\ N_n^R \end{pmatrix} = \begin{pmatrix} C_{11} & \cdots & \cdots & C_{1n} \\ \vdots & C_{ij} & \cdots & \vdots \\ \vdots & \cdots & \cdots & \vdots \\ C_{n1} & \cdots & \cdots & C_{nn} \end{pmatrix} \begin{pmatrix} N_1^M \\ \vdots \\ \vdots \\ N_n^M \end{pmatrix} \tag{6.2}$$

where C_{ij} means the correlation between N_i^R and N_j^M. In a certain (ie. ith) real $p_T(x_F)$ bin, we can get

$$N_i^R = \sum_{k=1}^{n} C_{ik} N_k^M \tag{6.3}$$

For the asymmetries, we have

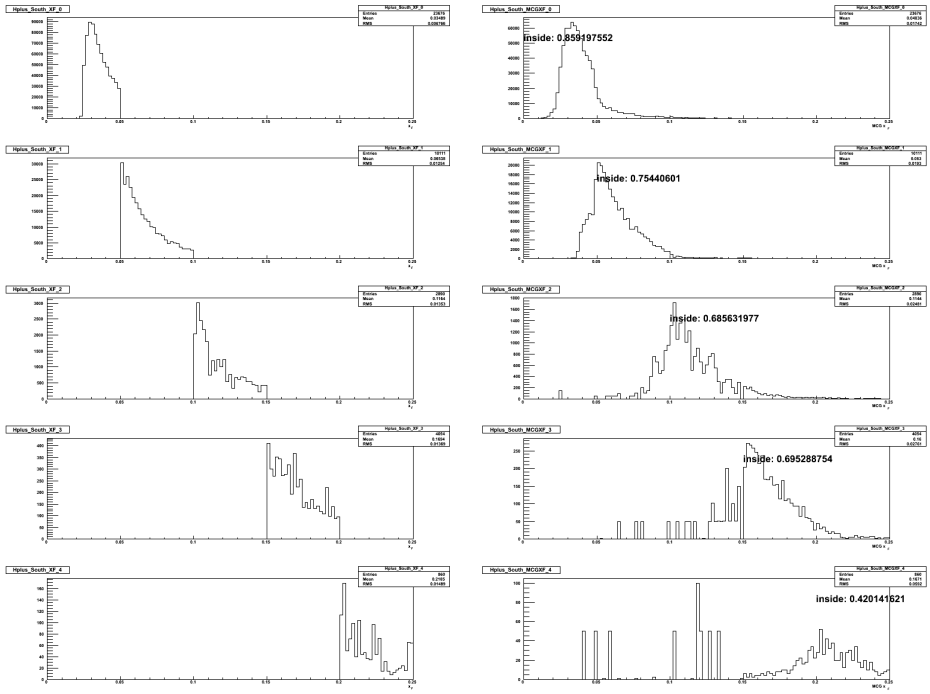

Figure 6.12 The x_F (p_z) smearing effects for positive charged hadrons at the south arm from the Monte-Carlo simulation. The left five plots are x_F (p_z) spectra for measured hadrons. The right five plots are x_F (p_z) spectra for hadrons from collision. The numbers on the right five plots are the fractions of measured hadrons from the same x_F (p_z) bin with hadrons really from collision.

$$A_N = \frac{\sqrt{N_-^{\uparrow} N_+^{\downarrow}} - \sqrt{N_-^{\downarrow} N_+^{\uparrow}}}{\sqrt{N_-^{\uparrow} N_+^{\downarrow}} + \sqrt{N_-^{\downarrow} N_+^{\uparrow}}} \tag{6.4}$$

where $N_+^{\uparrow}, N_+^{\downarrow}, N_-^{\uparrow}, N_-^{\downarrow}$ mean the numbers of hadrons measured in spin $\uparrow$ or $\downarrow$, left(+) or right(-). We want to have the real yield $N_-^{\uparrow}$, $N_+^{\downarrow}$, $N_-^{\downarrow}$ and $N_+^{\uparrow}$ to calculate real A_N, but we can only have measured yield. we can use Eq. 6.3 to convert measured yield to be real yield. For a certain (ie. ith) bin, we can have asymmetries as

$$A_N = \frac{\sqrt{(\sum_k C_{ik} N_{-,i}^{\uparrow,M})(\sum_k C_{ik} N_{+,i}^{\downarrow,M})} - \sqrt{(\sum_k C_{ik} N_{+,i}^{\uparrow,M})(\sum_k C_{ik} N_{-,i}^{\downarrow,M})}}{\sqrt{(\sum_k C_{ik} N_{-,i}^{\uparrow,M})(\sum_k C_{ik} N_{+,i}^{\downarrow,M})} + \sqrt{(\sum_k C_{ik} N_{+,i}^{\uparrow,M})(\sum_k C_{ik} N_{-,i}^{\downarrow,M})}} \tag{6.5}$$

The factors don't cancel because the mixed bins may not have the same number of events, and the error propagation depends on all measured bins that contribute.

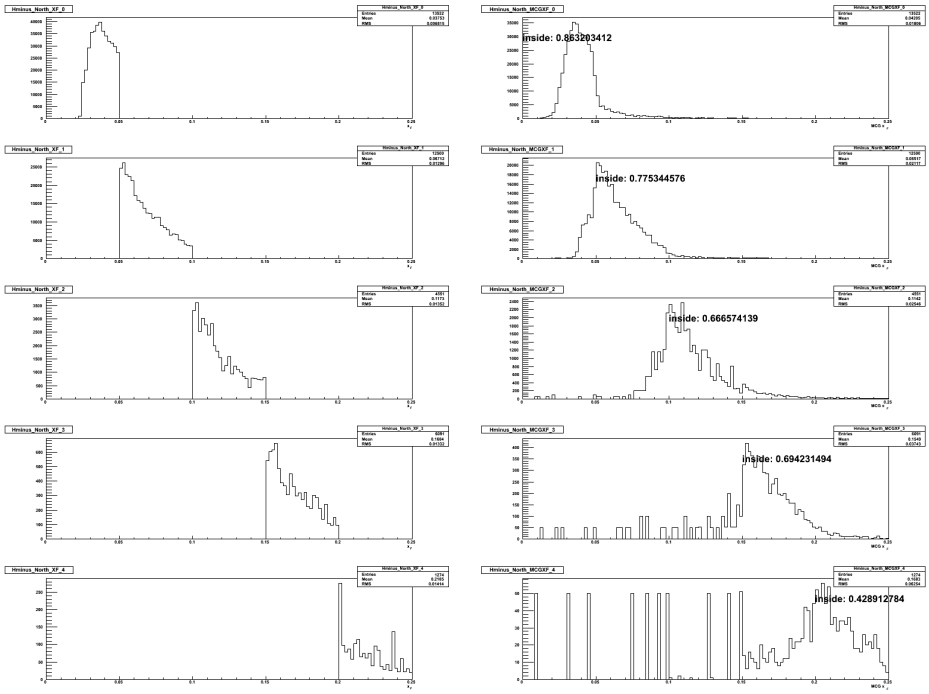

Figure 6.13 The x_F (p_z) smearing effects for negative charged hadrons at the north arm from the Monte-Carlo simulation. The left five plots are x_F (p_z) spectra for measured hadrons. The right five plots are x_F (p_z) spectra for hadrons from collision. The numbers on the right five plots are the fractions of measured hadrons from the same x_F (p_z) bin with hadrons really from collision.

The correlation matrix C can be derived from the simulation. In the simulation, for a measured hadron we can know what its real p_T and x_F are. We put each hadron in corresponding 2-dimensional histogram and normalized and then get a matrix as

$$\begin{pmatrix} N_1^M \\ \vdots \\ \vdots \\ N_n^M \end{pmatrix} = \begin{pmatrix} D_{11} & \cdots & \cdots & D_{1n} \\ \vdots & D_{ij} & \cdots & \vdots \\ \vdots & \cdots & \cdots & \vdots \\ D_{n1} & \cdots & \cdots & D_{nn} \end{pmatrix} \begin{pmatrix} N_1^R \\ \vdots \\ \vdots \\ N_n^R \end{pmatrix} \tag{6.6}$$

where D_{ij} means the probability of a hadron from jth real $p_T(x_F)$ bin but measured in ith $p_T(x_F)$ bin. The matrix D is just the inverse matrix of C or say $C = D^{-1}$.

The correlation matrices C for p_T and x_F bins in north and south arms are shown in

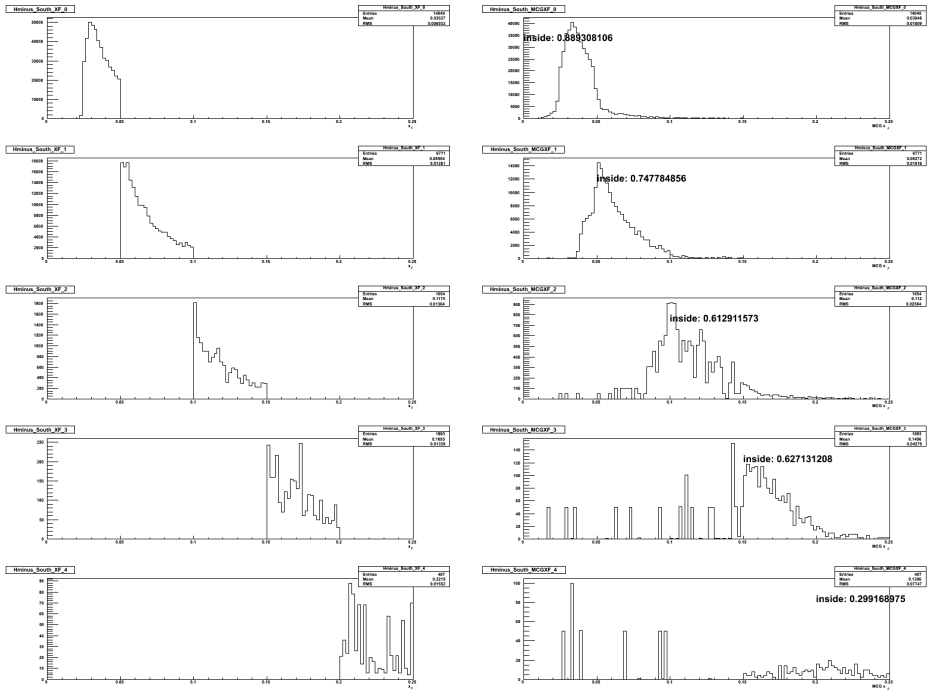

Figure 6.14 The x_F (p_z) smearing effects for negative charged hadrons at the south arm from the Monte-Carlo simulation. The left five plots are x_F (p_z) spectra for measured hadrons. The right five plots are x_F (p_z) spectra for hadrons from collision. The numbers on the right five plots are the fractions of measured hadrons from the same x_F (p_z) bin with hadrons really from collision.

Table 6.5, 6.6, 6.7 and 6.8.

However, it is found that the statistical uncertainties by using bin sharing correction matrices become much larger with bigger bin sharing effects. In Figure 6.11 to 6.18, more than 50% reconstructed hadrons for $x_F > 0.2$ and $p_T > 6\text{GeV}/c^2$ are not in the same bin with hadrons really from collision vertex. In these bins, the bin sharing effects are too large to be corrected. Therefore, we did not use these data samples in this analysis.

6.5.7 Correction of $\langle x_F \rangle$ and $\langle p_T \rangle$

We know that the $\langle x_F \rangle$ and $\langle p_T \rangle$ of measured hadrons are not as same as $\langle x_F \rangle$ and $\langle p_T \rangle$ of the hadrons really from collisions. A correction need to be done to get real $\langle x_F \rangle$ and $\langle p_T \rangle$ for

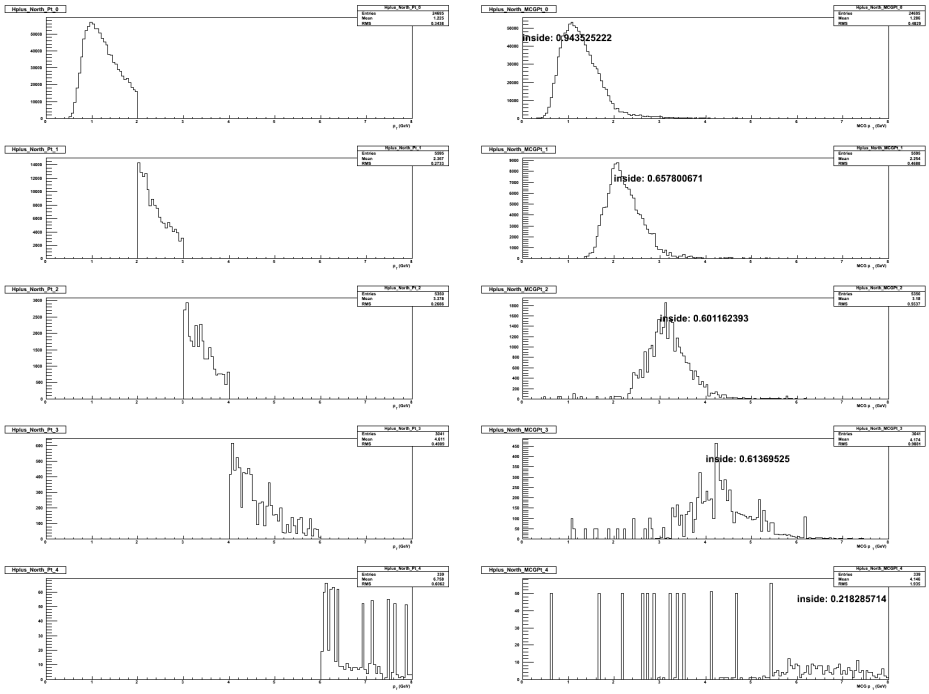

Figure 6.15 The p_T smearing effects for positive charged hadrons at the north arm from the Monte-Carlo simulation. The left five plots are p_T spectra for measured hadrons. The right five plots are p_T spectra for hadrons from collision. The numbers on the right five plots are the fractions of measured hadrons from the same p_T bin with hadrons really from collision.

each x_F and p_T bin.

Let us take correction of $\langle x_F \rangle$ as an example to explain how to do the correction. In our MC simulation, an $n \times n$ two dimensional histogram was created by setting x-axis to to be reconstructed x_F and y-axis to be the real x_F of hadrons. The projection on x-axis of this two-dimensional histogram is the distribution of reconstructed x_F and projection on y-axis is the distribution of real x_F of hadrons from collision. Then we can extract weight for each x-axis bin by matching the reconstructed x_F distribution in simulation to the x_F distribution in real data. We use the weights to correct the two-dimensional histograms and project it to y-axis in selected reconstructed x_F range (ie. $0.06 < x_F < 0.1$). The mean of the projection is just real $\langle x_F \rangle$ of the selected reconstructed x_F range(bin). Similar calculations can be done for p_T bins as well.

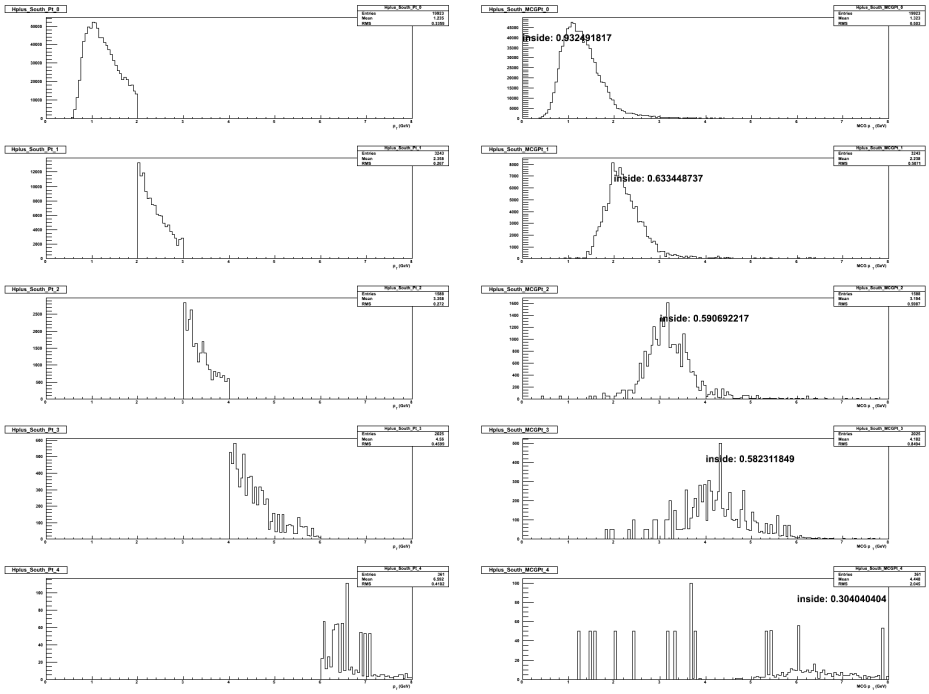

Figure 6.16 The p_T smearing effects for positive charged hadrons at the south arm from the Monte-Carlo simulation. The left five plots are p_T spectra for measured hadrons. The right five plots are p_T spectra for hadrons from collision. The numbers on the right five plots are the fractions of measured hadrons from the same p_T bin with hadrons really from collision.

In order to get $\langle p_T \rangle$ in selected x_F bin, just create a two dimensional histogram with x-axis to to be reconstructed x_F and y-axis to be the real p_T of hadrons' grandparents. Then do same weighting calculation we discussed above. The projection on y-axis of the two dimensional histograms is just real $\langle p_T \rangle$ in the x_F bin. Similar calculation can be applied on get $\langle p_T \rangle$ in selected p_T bins.

6.5.8 Summary of Cuts Used In This Analysis

The optimal cuts found from the simulation are summarized below:

- lastGap == 2 or 3, where lastGap means the last MuID gap the particles stopped by.
- $p_{st1} > 1.4$ GeV for tracks which lastGap==2, $p_{st1} > 1.8$ GeV for tracks which last-

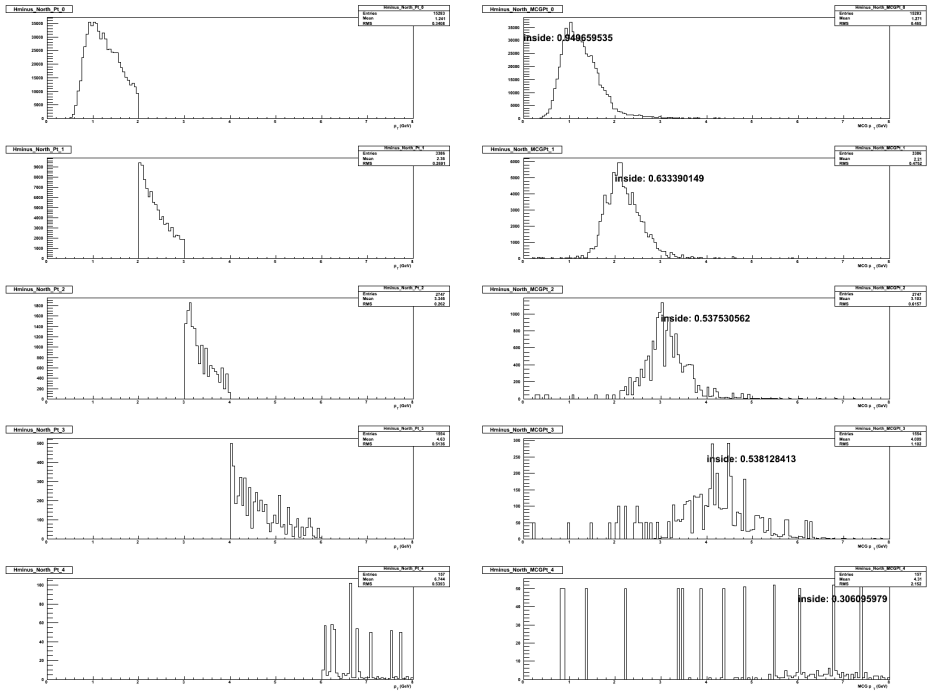

Figure 6.17 The p_T smearing effects for negative charged hadrons at the north arm from the Monte-Carlo simulation. The left five plots are p_T spectra for measured hadrons. The right five plots are p_T spectra for hadrons from collision. The numbers on the right five plots are the fractions of measured hadrons from the same p_T bin with hadrons really from collision.

Gap==3 where p_{st1} is the reconstructed momentum of particles at MuTr Station 1.

- $1 < p_T < 6$ GeV
- $\chi^2_{mutr} > 20$
- $|p_z| < 20$ GeV
- $1.2 < \eta < 2.4$ for north arm, $-2.2 < \eta < -1.2$ for south arm.
- $p\theta_{xp} < 0.2$, where $p = \frac{p_{vtx}+p_{st1}}{2}$, p_{vtx} is the reconstructed momentum of particles at vertex, θ_{xp} is the angle between $\vec{p}_{vtx}$ and $\vec{p}_{st1}$ as Figure 6.10 shown.

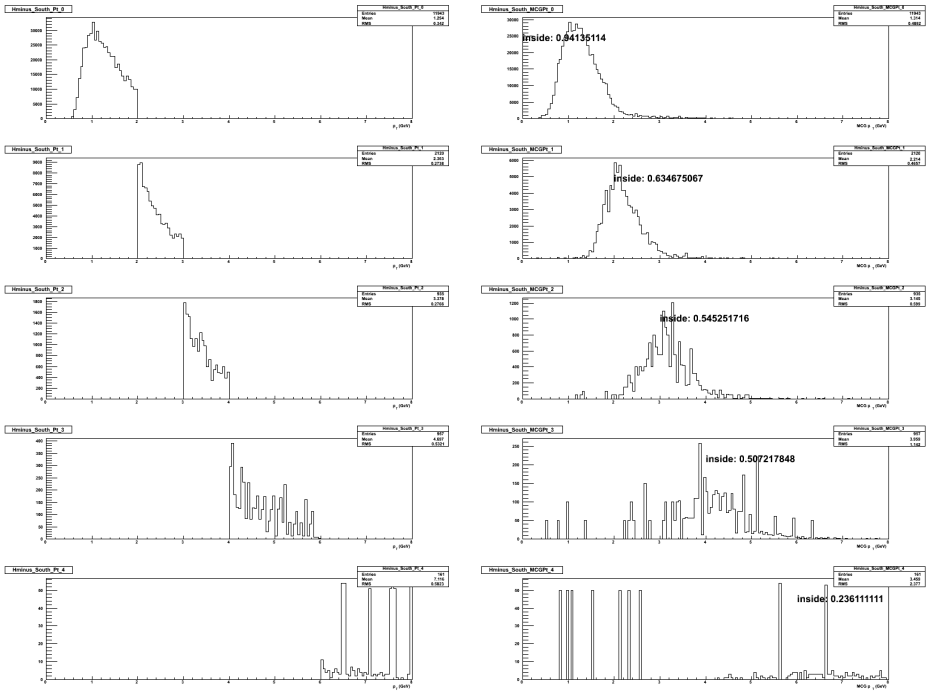

Figure 6.18 The p_T smearing effects for negative charged hadrons at the south arm from the Monte-Carlo simulation. The left five plots are p_T spectra for measured hadrons. The right five plots are p_T spectra for hadrons from collision. The numbers on the right five plots are the fractions of measured hadrons from the same p_T bin with hadrons really from collision.

6.6 Calculation of A_N

Two approaches can be used to calculate the single transverse spin asymmetry: relative luminosity formula and square root formula. Due to low statistics especially for high x_F and p_T bins, relative luminosity formula is not good for this analysis. The details for the two approaches are shown as following.

6.6.1 Square root formula

The advantages of using square root formula are that (1) no luminosity correction is needed and the luminosity asymmetries will be canceled out; (2) it can be used in low statistics cases. The square root formula weighted by $\langle|cos(\phi)|\rangle$ and its uncertainty formula are shown as Eq. 6.7

Table 6.5 The correlation matrices of x_F bins for positive hadrons.

x_F	North Arm			
	< 0.06	$0.06 - 0.1$	$0.1 - 0.15$	$0.15 - 0.2$
< 0.06	1.175	-0.3349	-0.1816	-0.2025
$0.06 - 0.1$	-0.1824	1.404	-0.4139	-0.4737
$0.1 - 0.15$	0.00857	-0.07219	1.694	-0.8555
$0.15 - 0.2$	-0.0015	0.00343	-0.09849	2.532
x_F	South Arm			
	< 0.06	$0.06 - 0.1$	$0.1 - 0.15$	$0.15 - 0.2$
< 0.06	1.139	-0.501	-0.3792	-0.4337
$0.06 - 0.1$	-0.1433	1.553	-0.463	-0.6108
$0.1 - 0.15$	0.004737	-0.05472	2.022	-1.134
$0.15 - 0.2$	-0.00021	0.002559	-0.18	3.178

Table 6.6 The correlation matrices of x_F bins for negative hadrons.

x_F	North Arm			
	< 0.06	$0.06 - 0.1$	$0.1 - 0.15$	$0.15 - 0.2$
< 0.06	1.198	-0.238	-0.1408	-0.2646
$0.06 - 0.1$	-0.2061	1.304	-0.395	-0.5169
$0.1 - 0.15$	0.009202	-0.06676	1.649	-0.902
$0.15 - 0.2$	-0.001459	0.0002719	-0.1136	2.684
x_F	South Arm			
	< 0.06	$0.06 - 0.1$	$0.1 - 0.15$	$0.15 - 0.2$
< 0.06	1.14	-0.3463	-0.3244	-0.5432
$0.06 - 0.1$	-0.1458	1.413	-0.5847	-0.6039
$0.1 - 0.15$	0.007117	-0.07137	2.1	-1.385
$0.15 - 0.2$	-0.001715	0.004387	-0.1912	3.532

and 6.8, where P is the polarization, ϕ is the angle of hadrons in PHENIX coordinate and $N_+^\uparrow, N_+^\downarrow, N_-^\uparrow, N_-^\downarrow$ mean the numbers of hadrons in spin $\uparrow$ or $\downarrow$, left(+) or right(-) which are corrected by using the bin sharing matrices, and $E_+^\downarrow = \frac{(\delta N_+^\downarrow)^2}{N_+^\downarrow}$, and similar definition for $E_-^\uparrow$, $E_+^\uparrow$ and $E_-^\downarrow$.

$$A_N = \frac{1}{P\langle|cos(\phi)|\rangle} \frac{\sqrt{N_-^\uparrow N_+^\downarrow} - \sqrt{N_-^\downarrow N_+^\uparrow}}{\sqrt{N_-^\uparrow N_+^\downarrow} + \sqrt{N_-^\downarrow N_+^\uparrow}} \tag{6.7}$$

Table 6.7 The correlation matrices of p_T bins for positive hadrons.

p_T	North Arm			
(GeV)	< 2	$2-3$	$3-4$	$4-6$
< 2	1.068	-0.4716	-0.3234	-0.3907
$2-3$	-0.07523	1.667	-0.4825	-0.2683
$3-4$	0.009013	-0.2153	2.05	-0.5821
$4-6$	-0.00128	0.01999	-0.2444	2.241
(GeV)	< 2	$2-3$	$3-4$	$4-6$
< 2	1.08	-0.622	-0.305	-0.4512
$2-3$	-0.08854	1.821	-0.4416	-0.4451
$3-4$	0.01046	-0.2332	2.163	-0.693
$4-6$	-0.001936	0.03419	-0.4166	2.589

Table 6.8 The correlation matrices of p_T bins for negative hadrons.

p_T	North Arm			
(GeV)	< 2	$2-3$	$3-4$	$4-6$
< 2	1.074	-0.4485	-0.2654	-0.3953
$2-3$	-0.08337	1.659	-0.5139	-0.2605
$3-4$	0.01003	-0.2244	2.086	-0.5809
$4-6$	-0.0008914	0.0143	-0.3063	2.237
p_T	South Arm			
(GeV)	< 2	$2-3$	$3-4$	$4-6$
< 2	1.08	-0.435	-0.4312	-0.3396
$2-3$	-0.09076	1.68	-0.4895	-0.1673
$3-4$	0.01379	-0.2739	2.312	-1.04
$4-6$	-0.00256	0.02905	-0.3909	2.546

$$\delta A_N = \sqrt{(A_N \frac{\delta P}{P})^2 + \frac{N_-^{\downarrow} N_+^{\uparrow} N_-^{\uparrow} E_+^{\downarrow} + N_-^{\downarrow} N_+^{\uparrow} N_+^{\downarrow} E_-^{\uparrow} + N_-^{\uparrow} N_+^{\downarrow} N_-^{\downarrow} E_+^{\uparrow} + N_-^{\uparrow} N_+^{\downarrow} N_+^{\uparrow} E_-^{\downarrow}}{P^2 \langle |cos(\Phi)| \rangle^2 (\sqrt{N_-^{\uparrow} N_+^{\downarrow}} + \sqrt{N_-^{\downarrow} N_+^{\uparrow}})^4}} \quad (6.8)$$

The fill by fill asymmetry for each P_T and x_F bin is calculated by using Eq. 6.7 and 6.8. Then asymmetry for each fill will be put in a histogram which is fit by a constant as example figure 6.19 shown. The fitting constant and uncertainty will be the average asymmetry and its statistical error. The average asymmetries and uncertainties are shown in Figures 6.20, 6.21 and Tables 6.9, 6.10, 6.11, 6.12.

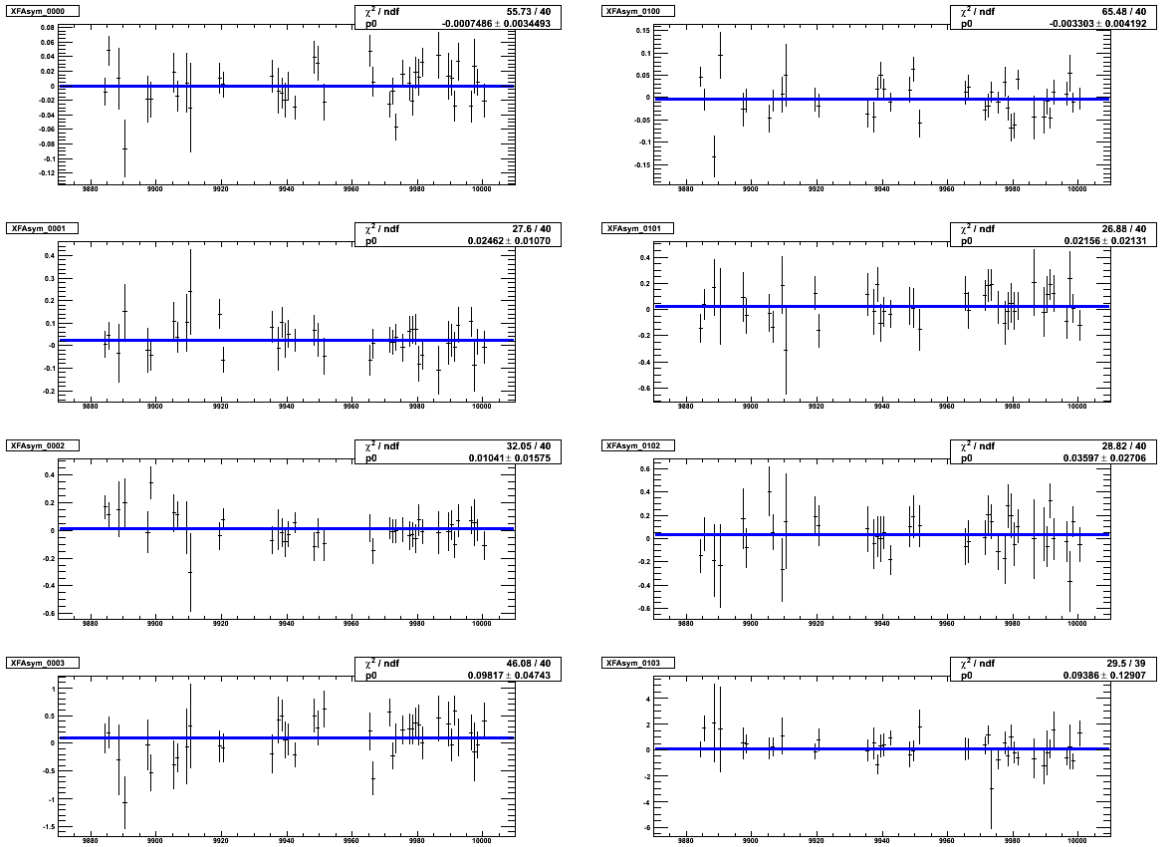

Figure 6.19 The fill by fill asymmetries fitting by a constant for x_F bins of < 0.06, $0.06 - 0.1$, $0.1 - 0.15$ and $0.15 - 0.2$ from top to bottom on the both forward (left) and backward (right) rapidity.

6.6.2 Systematics

The systematic uncertainties on the beam polarization has been estimated by CNI polarimetry group in Brookhaven National Lab, which $\approx 4.2\%$ for blue beam and $\approx 7.2\%$ for yellow beam[63].

We have x_F and p_T dependent systematics uncertainties which come from asymmetry mixing/dilution fractions in the Table 6.4.

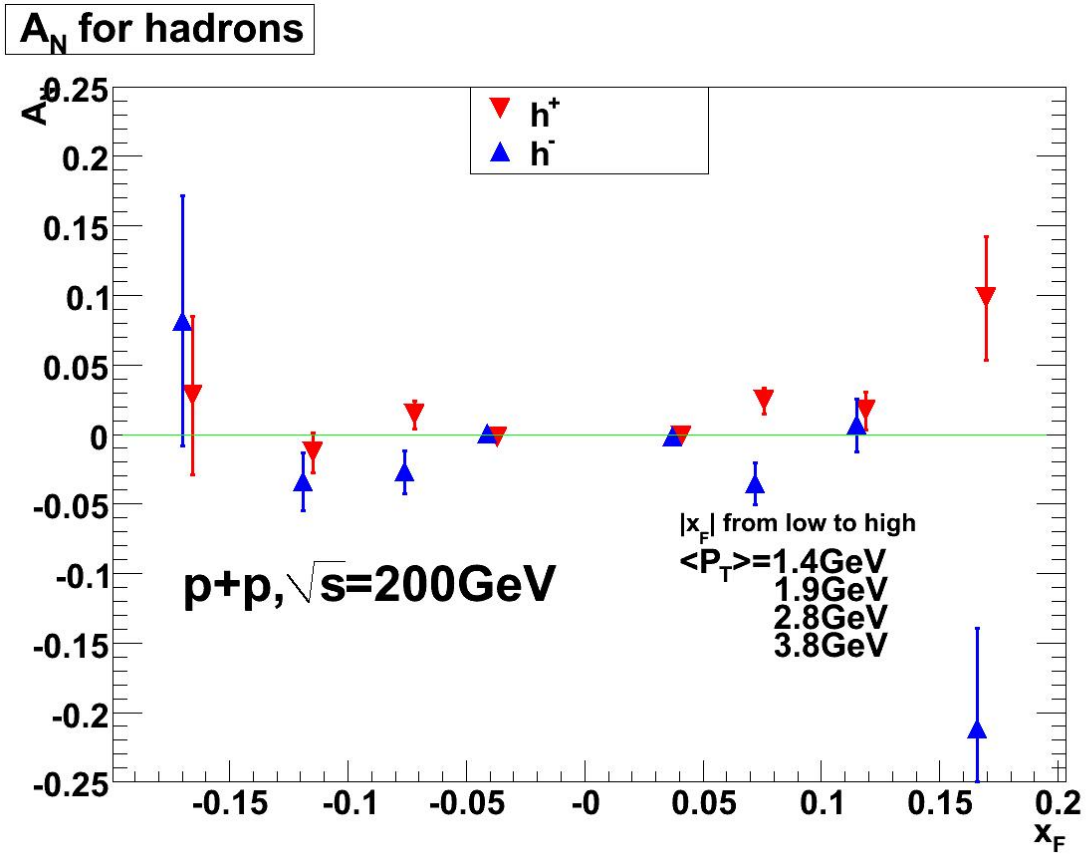

Figure 6.20 The A_N versus x_F for both h^+ and h^- by using square root formula.

Table 6.9 Fill by fill integral asymmetries, uncertainties and χ^2 calculated by square root formula for positive hadrons.

For h^+	$A_N(\times 10^{-2})$			Uncertainty $(\times 10^{-2})$			χ^2/NDF	
in x_F bins	Blue	Yellow	Combined	Blue	Yellow	Combined	Blue	Yellow
$0 < x_F < 0.06$	-0.07	-0.33	-0.18	0.34	0.42	0.27	1.39	1.64
$0.06 < x_F < 0.1$	2.46	2.16	2.40	1.07	2.13	0.96	0.69	0.67
$0.1 < x_F < 0.15$	1.04	3.60	1.69	1.58	2.71	1.36	0.80	0.72
$0.15 < x_F < 0.2$	9.82	9.39	9.77	4.74	12.91	4.45	1.15	0.76
$-0.06 < x_F < 0$	-0.41	0.08	-0.24	0.34	0.46	0.27	0.81	1.11
$-0.1 < x_F < -0.06$	4.05	1.15	1.38	3.59	1.07	1.02	1.40	1.02
$-0.15 < x_F < -0.1$	-1.13	-1.45	-1.32	2.28	1.88	1.45	0.77	0.60
$-0.2 < x_F < -0.15$	1.17	3.48	2.78	10.37	6.82	5.70	0.52	1.06

Table 6.10 Fill by fill integral asymmetries, uncertainties and χ^2 calculated by square root formula for negative hadrons.

For h^- in x_F bins	$A_N(\times 10^{-2})$			Uncertainty $(\times 10^{-2})$			χ^2/NDF	
	Blue	Yellow	Combined	Blue	Yellow	Combined	Blue	Yellow
$0 < x_F < 0.06$	0.10	-0.53	-0.15	0.47	0.57	0.36	1.21	1.01
$0.06 < x_F < 0.1$	-3.88	-2.22	-3.53	1.69	3.29	1.50	0.67	1.06
$0.1 < x_F < 0.15$	0.074	0.30	0.65	2.18	4.17	1.93	1.06	0.94
$0.15 < x_F < 0.2$	-22.52	-2.86	-21.24	7.51	28.55	7.26	1.02	0.62
$-0.06 < x_F < 0$	-0.09	0.27	0.05	0.47	0.60	0.37	1.29	1.22
$-0.1 < x_F < -0.06$	-4.41	-2.67	-2.71	10.04	1.55	1.53	0.65	0.76
$-0.15 < x_F < -0.1$	-2.75	-3.83	-3.39	3.28	2.71	2.09	1.05	1.05
$-0.2 < x_F < -0.15$	-24.82	14.22	8.17	22.80	9.76	8.97	0.44	0.84

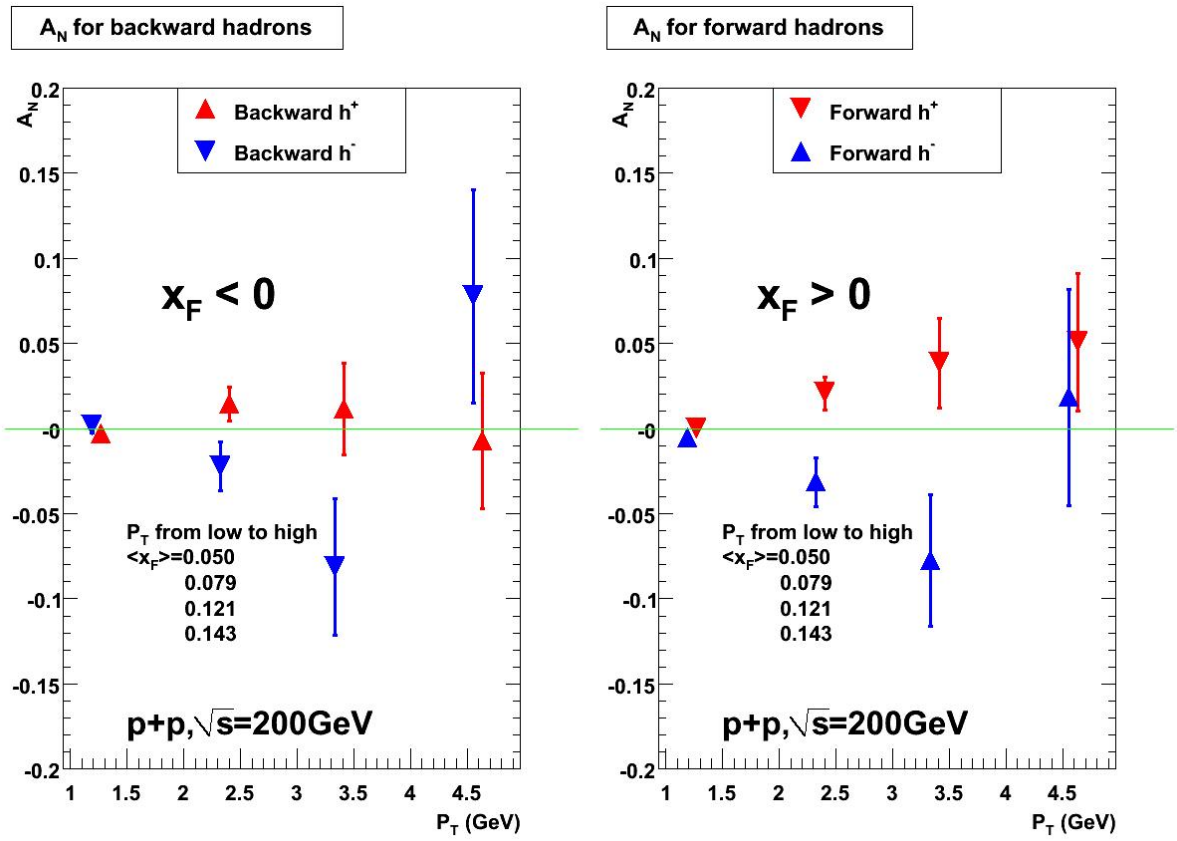

Figure 6.21 The A_N versus p_T for both h^+ and h^- by using square root formula.

Table 6.11 Fill by fill integral asymmetries, uncertainties and χ^2 calculated by square root formula for positive hadrons.

For h^+ in p_T (GeV)		$A_N(\times 10^{-2})$			Uncertainty $(\times 10^{-2})$			χ^2/NDF	
		Blue	Yellow	Combined	Blue	Yellow	Combined	Blue	Yellow
Forward	$p_T < 2$	0.18	-0.46	-0.04	0.31	0.43	0.25	1.32	1.55
	$2 < p_T < 3$	2.39	1.58	2.06	1.25	1.53	0.97	0.98	1.07
	$3 < p_T < 4$	1.99	7.04	3.82	3.31	4.38	2.64	0.87	0.95
	$4 < p_T < 6$	5.37	4.54	5.05	5.16	6.54	4.05	1.07	1.15
Backward	$p_T < 2$	-0.60	0.04	-0.31	0.35	0.38	0.26	0.82	0.97
	$2 < p_T < 3$	1.68	1.03	1.43	1.26	1.57	0.98	0.83	1.08
	$3 < p_T < 4$	-0.75	1.66	1.15	3.62	4.08	2.71	0.83	1.10
	$4 < p_T < 6$	-1.06	0.26	-0.73	4.61	8.10	4.00	1.19	0.92

Table 6.12 Fill by fill integral asymmetries, uncertainties and χ^2 calculated by square root formula for negative hadrons.

For h^- in p_T (GeV)		$A_N(\times 10^{-2})$			Uncertainty $(\times 10^{-2})$			χ^2/NDF	
		Blue	Yellow	Combined	Blue	Yellow	Combined	Blue	Yellow
Forward	$p_T < 2$	-0.02	-1.44	-0.53	0.43	0.58	0.35	1.05	0.71
	$2 < p_T < 3$	-3.96	5.02	-0.31	1.84	2.22	1.42	0.90	1.16
	$3 < p_T < 4$	-8.74	-5.17	-7.77	4.51	7.37	3.85	1.00	1.15
	$4 < p_T < 6$	2.33	1.15	1.83	8.40	9.75	6.36	1.32	1.05
Backward	$p_T < 2$	0.04	0.20	0.12	0.49	0.52	0.36	1.32	1.41
	$2 < p_T < 3$	-1.81	-2.87	-2.23	1.84	2.27	1.43	0.90	1.13
	$3 < p_T < 4$	-2.84	-15.85	-8.14	5.19	6.27	4.00	0.82	0.91
	$4 < p_T < 6$	4.02	14.82	7.76	7.76	10.67	6.28	1.21	1.02

CHAPTER 7. Single Transverse Spin Asymmetry of Mid-Rapidity Back-to-Back Di-Hadron Correlation

As we discussed in Charpter 2, it was proposed that the Sivers effect can be observed by back-to-back di-jet correlation in transversely polarized $p+p$ collision. PHENIX mid-rapidity is only covered by two central arms with azimuthal coverage $\frac{\pi}{2}$ and $|\eta| < 0.35$, which make it very difficult to directly reconstruct full jets. In this analysis, we use di-hadron correlation instead of di-jet correlation.

In the mid-rapidity back-to-back di-hadron correlation, di-hadron from di-jets respectively means a triggered leading π^0 and an away-side leading charged hadron. In this chapter, we will discuss the di-hadron analysis in details.

7.1 Run Selection

This data sample was collected from transverse polarized p+p collision at $\sqrt{s} = 200$GeV from run189579 (3/12/2006) through run197795 (4/25/2006) in Run6.

Some runs are excluded due to failing one or more of the following QA check:

- Remove runs whose sum of BBCLL1 scaler counts are not consistent with BBC Live counts from Run Control Log Book
- Remove runs whose spin patterns not found in spin database
- Remove runs whose polarization information are not consistent between PDST and CDEV
- Remove low statistics runs

- Remove runs whose time duration were less than 8 minutes
- Remove runs with missing beam polarization information
- Remove runs during STAR magnet trip
- Remove runs which missing GL1P Log files

The survived good runs in QA check is listed in Appendix II.

7.2 Event and Particle Selection

7.2.1 Global Event Selection

There are two requirements for the global event selection:

- z-vertex requirement: As many of the central-arm analyses, we use $|z_{BBC}| < 30$cm in this analysis.
- Trigger requirement: The event must be triggered by a coincidence between the ERT4x4c trigger and a BBCLL1 trigger. The ERT triggers will be introduced below.

7.2.2 ERT triggers

Although BBCLL1 trigger samples roughly 50% of all $p+p$ events and roughly 80% of π^0 events in PHENIX acceptance, π^0 has relatively small cross section in high p_T region which we are really interested in. Thus, we require an additional ERT (Emcal RICH Trigger) trigger in coincidence with the minimum bias trigger.

The ERT trigger is a particle based trigger which can trigger particles with a certain deposited energy. If a particle in a particular event is qualified for the ERT trigger condition, the event will be recorded. It means that not only candidate particles but particles in the event which are not associated with an ERT trigger are recorded. Those non-associate particles are called "random sample". In order to ensure that a particle is associated with a trigger, the size of the trigger region is limited.

The EMCal towers are grouped in sets of 2×2 towers, which make up a basic trigger tile. If a high energy particle splits its energy in neighboring tiles, the threshold might not be met for any one individual tile. Therefore, 2×2 neighboring basic tiles are combined to create 4×4 tower trigger. There are 3 types of ERT 4×4 trigger: $4 \times 4a$, $4 \times 4b$ and $4 \times 4c$, which can correspondingly trigger different threshold energy 2.1GeV, 2.8GeV and 1.4GeV. In this analysis, ERT $4 \times 4c$ triggered data sample is used. Sets of 12×12 towers are grouped into super-modules, which are used in the trigger logic for event triggering. Super-modules are the smallest triggering unit written in the output data. The π^0 is reconstructed from two photons, in which the higher energy photon candidate are required to be fired by a triggered super-module. This reduces random photons greatly and improve the signal background ratio of reconstructed π^0s.

7.2.3 Photon selection and π_0 reconstruction

Since π^0s have a short life time(roughly 10^{-16}s) and 99% of them decay in two photons channel ($\pi^0 \rightarrow \gamma + \gamma$), we measure decay photon pairs to reconstruct π^0s.

The photons entering the EMCal will produce an electromagnetic shower, a spray of electrons and photons. These electrons and photons will radiate light in the EMCal material and be collected by EMCal towers.

Because the energy distribution among towers of the same cluster (photon/hadron) drops sharply from center to edge, we use 21 towers (5×5 without 4 corners) to reconstruct one particle. Photons usually need central 3×3 towers to collect almost all the energy, while hadrons may need all 21 towers. Since we do not know whether it is a photon or hadron in the first stage of data reconstruction, we will use two energies to mark each cluster: "e" assuming it is a hadron (based the sum of energy of all towers), and "ecore" assuming it is a photon (based on the sum of energy of central 9 towers).

When a cluster has very low energy, it is very difficult to say if it comes from a signal or electronic noise. In order to reduce electronic noise, we usually exclude those low energy clusters by placing a higher threshold. Due to the different nature of the two types of EMCal

at PHENIX, two different minimum energy cuts are applied: $E > 0.1$GeV for PbSc and $E > 0.2$GeV for PbGl.

The EMCal tower electronics sometimes does not work fully well. One tower may be too hot or dead. If a photon comes of such tower, it is not to be trusted. So we make a dead/warn map of EMCal towers, and require that any photon we used cannot be from this map. In PHENIX, the general EMCal dead-warn map is included into recalibrators. These maps are calculated by EMCal experts, written into database and later called by the recalibrators. Beyond that, we need make extra warn-dead maps by checking hits from each tower in various p_T range because the towers could have p_T dependent hot or dead behavior.

Hot (noisy) and dead towers, as well as towers with failing in energy calibration, are defined as bad towers. To determine hot and dead towers, sector by sector distributions of the number of hits per tower were plotted for energy bins 1GeV wide from 0 to 10GeV. For the lowest energy bin $(0 - 1\text{GeV})$, clusters with energy below 0.1GeV (0.2GeV) in PbSc (PbGl) were not used. For each energy bin, towers in which the number of hits was 10 times RMS(Root of Mean Square) value larger than the mean were declared hot. Any tower that was declared hot in any energy bin was declared hot for the full data sample. Dead towers were defined as towers with hit less than the mean by more than 10 times RMS value. Edge towers are not able to be calibrated and are thus declared bad. A 3×3 block of towers around any bad tower is excluded, and any cluster centered on an excluded tower is excluded from the analysis. In Run6, the masked and edge towers for each sector is shown in Figure 7.1, and the statistics of bad towers for all sectors is listed in Table 7.1.

Photons, electrons and hadrons all will shower in an infinite calorimeter. However, hadrons interact with the material via the strong force, while photons and electrons interact electromagnetically. Therefore, due to the much shorter range of the strong force, hadrons will typically travel farther in the material before interacting. Similarly, due to the different forces involved, the average shape of the shower is different in the two cases. Here, we will use this difference to exclude showers that have a low probability to be electromagnetic.

Using a test beam of $E = 1$GeV photons [33], the shower shape in towers similar to

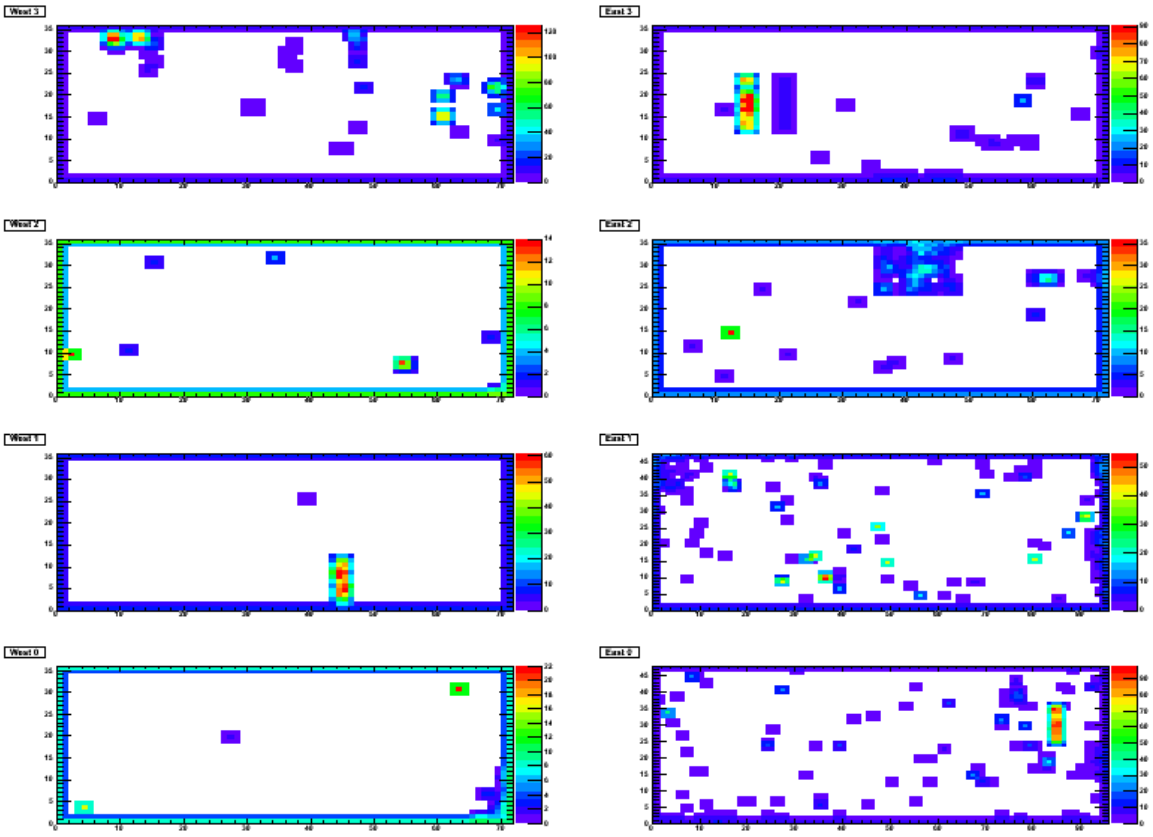

Figure 7.1 Dead—Warn Map for each sector in both west and east central Emcal detectors in Run6. All colorful towers are masked as dead—hot towers and excluded from the analysis.

those in the EMCal was measured. The fractional energy per tower was calculated for each electromagnetic cluster, and an average distribution was determined. By fitting the fractional energy per tower for each candidate cluster in PHENIX, the probability (calculated from the χ^2 of the fit that the cluster fits the expected distribution for an electromagnetic shower is determined. In the π^0 analysis, all clusters that have a less than 2% probability (called *photon_prob*) of being electromagnetic are usually excluded.

Once we measure at least two good photons by Emcal detectors in each event, we can use them to reconstruct the momentum and energy of π^0 by momentum and energy conservation laws and then calculate the invariant mass for π^0. Because the east arm has two different types of Emcal detectors: PbSc and PbGl, the energy measured by them may not be consistent. Thus

Table 7.1 The statistics of bad/edge towers for all sectors in Run6.

Sector	**Masked Bad Towers**	**Edge Towers**	**Total towers**
W0 (PbSc)	469 (18.1%)	416 (16.0%)	2592
W1 (PbSc)	469 (18.1%)	416 (16.0%)	2592
W2 (PbSc)	476 (18.3%)	416 (16.0%)	2592
W3 (PbSc)	665 (25.7%)	416 (16.0%)	2592
E0 (PbGl)	1247 (27.1%)	560 (12.2%)	4608
E1 (PbGl)	1213 (26.3%)	560 (12.2%)	4608
E2 (PbSc)	687 (26.5%)	416 (16.0%)	2592
E3 (PbSc)	662 (25.5%)	416 (16.0%)	2592
PbSc	3428 (22.0%)	2496 (16.0%)	15552
PbGl	2460 (26.7%)	1120 (12.2%)	9216
Total	5888 (23.8%)	3616 (14.6%)	24768

we avoid using one photon from the PbSc and the other photon from the PbGl to reconstruct the π^0. The distribution of the invariant mass of photon pairs for PbSc at both west and east arms and PbGl at east arm in various p_T range is shown in Figure 7.2, 7.3 and 7.4.

In the high p_T region, most "fake" π^0 come from the random combination of a high p_T photon (may come from a real high p_T π^0) and a low energy photon from unknown source. In order to remove these "fake" π^0s, an asymmetry between the energy of two photons is defined in Eq. 7.1. In this analysis, we apply an $Asymmetry < 0.7$ cut to all π^0s.

$$Asymmetry = \frac{E_1^\gamma - E_2^\gamma}{E_1^\gamma + E_2^\gamma} \tag{7.1}$$

In order to estimate the signal background ratio, we usually use a Gaussian function plus a 3rd order polynomial to fit the photon pair spectra. An example is shown in the Figure 7.5. The Gaussian is taken as real π^0 signal and the 3rd order polynomial is taken as combinatorial background. We usually take Gaussian peak $\pm 2.5\sigma$ as the effective π^0 signal region, which is roughly $0.115 < Mass_{\pi^0} < 0.165\text{GeV}/c^2$. The signal background ratio varies with p_T and is shown in 7.5.

The cuts used for π^0 reconstruction are summarized below:

- All photon clusters must not include the masked hot or dead towers;

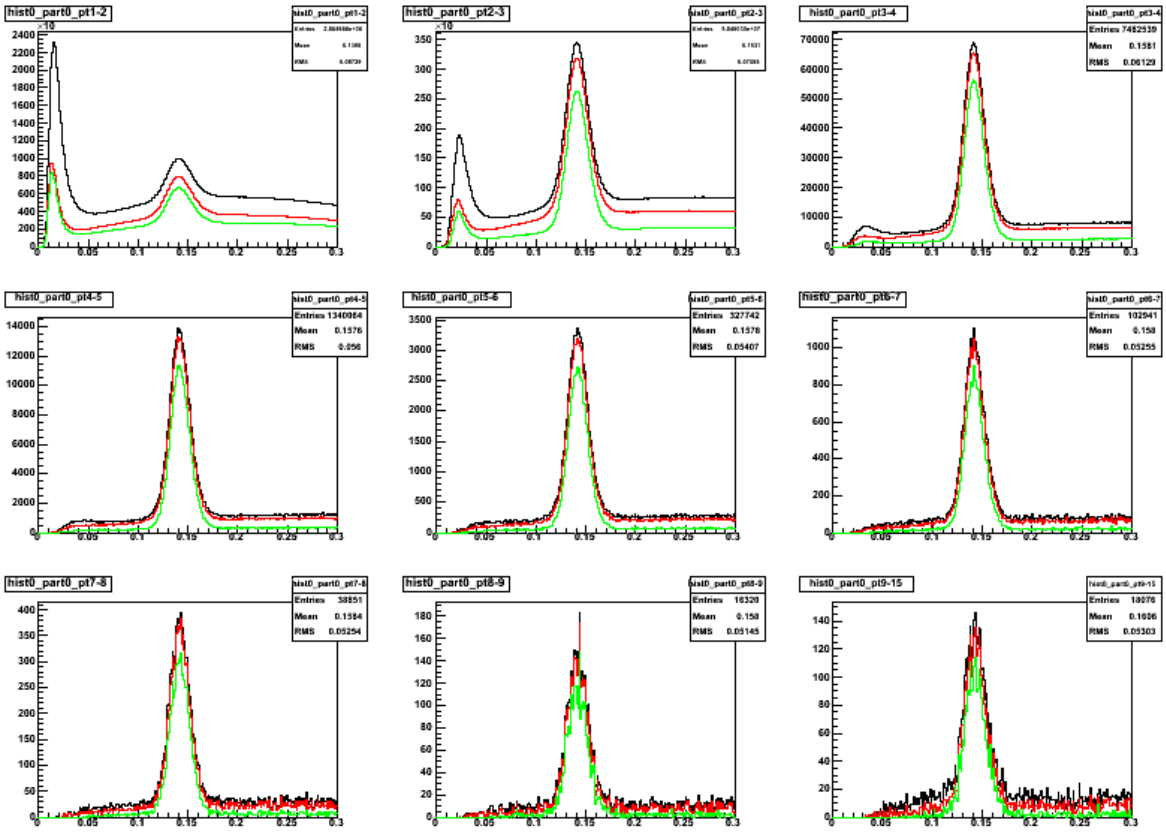

Figure 7.2 Photon pair invariant mass spectra of PbSc at west arm with p_T in various range in the order of left to right and top to bottom. Black lines indicate the spectra by applying minimum photon energy cut in all reconstructed π^0. Red lines indicate the spectra by applying additional *photon_prob* cut based on black lines. Green lines indicates the spectra by applying additional di-photon energy asymmetry cut based on red lines.

- Both photon are from the same type of Emcal at the same arm, and at least one of the pair of photons must be from the same EMCal module that fires the ERT trigger in that event;
- $E_\gamma > 0.1$GeV for PbSc and $E_\gamma > 0.2$GeV for PbGl;
- *photon_prob* > 0.02;
- Asymmetry of two photon energies is less than 0.7;

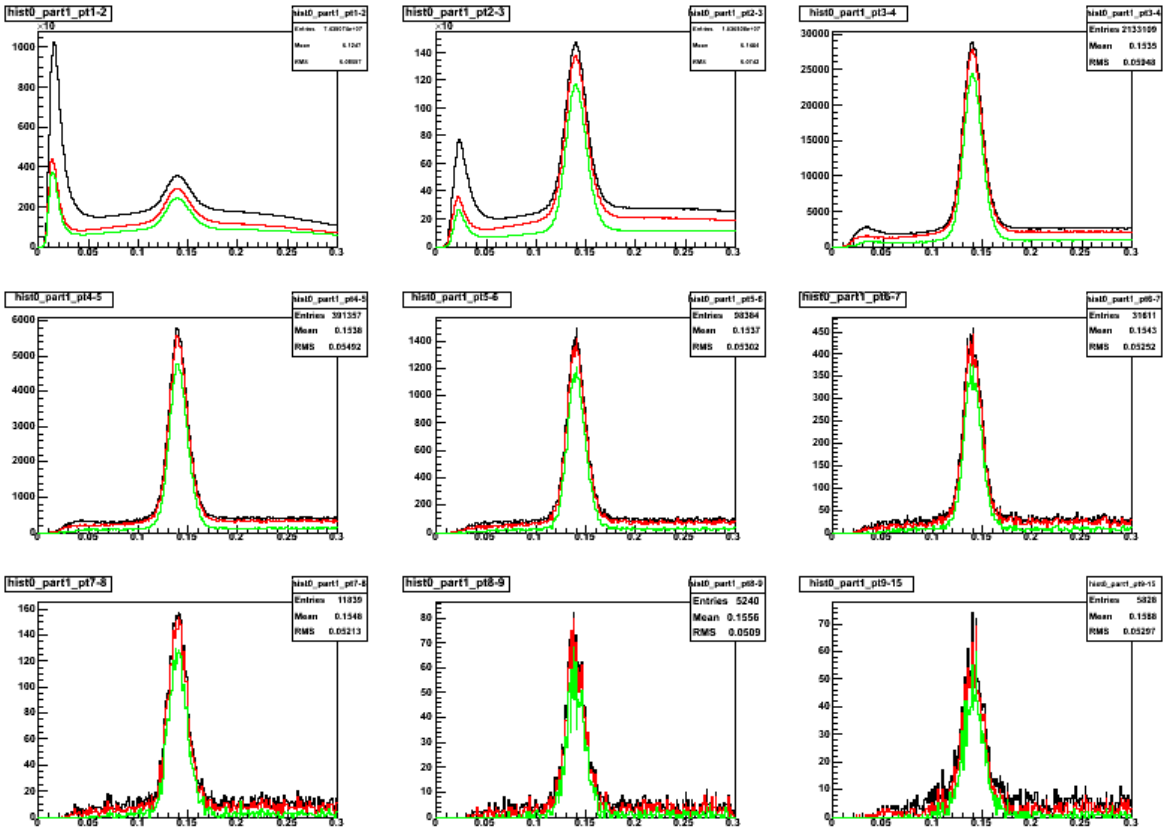

Figure 7.3 Photon pair invariant mass spectra of PbSc at east arm with p_T in various range in the order of left to right and top to bottom. Black lines indicate the spectra by applying minimum photon energy cut in all reconstructed π^0. Red lines indicate the spectra by applying additional *photon_prob* cut based on black lines. Green lines indicates the spectra by applying additional di-photon energy asymmetry cut based on red lines.

- $0.115 < M_{\pi^0} < 0.165$ GeV/c^2

7.2.4 Charged Hadron Selection

Charged hadrons are reconstructed by using tracks from the drift chambers(DCs) and pad chambers(PCs). The drift chambers are used to measure the momentum of charged tracks, and the pad chambers are used as matching. Because conversions and fake tracks (ghost) exist, we need make a quality cut on each single charged track. First we need use DC and PC1 (first layer of PC). DC has 3 set of planes: X1 and X2 for ϕ resolution, and UV for z resolution.

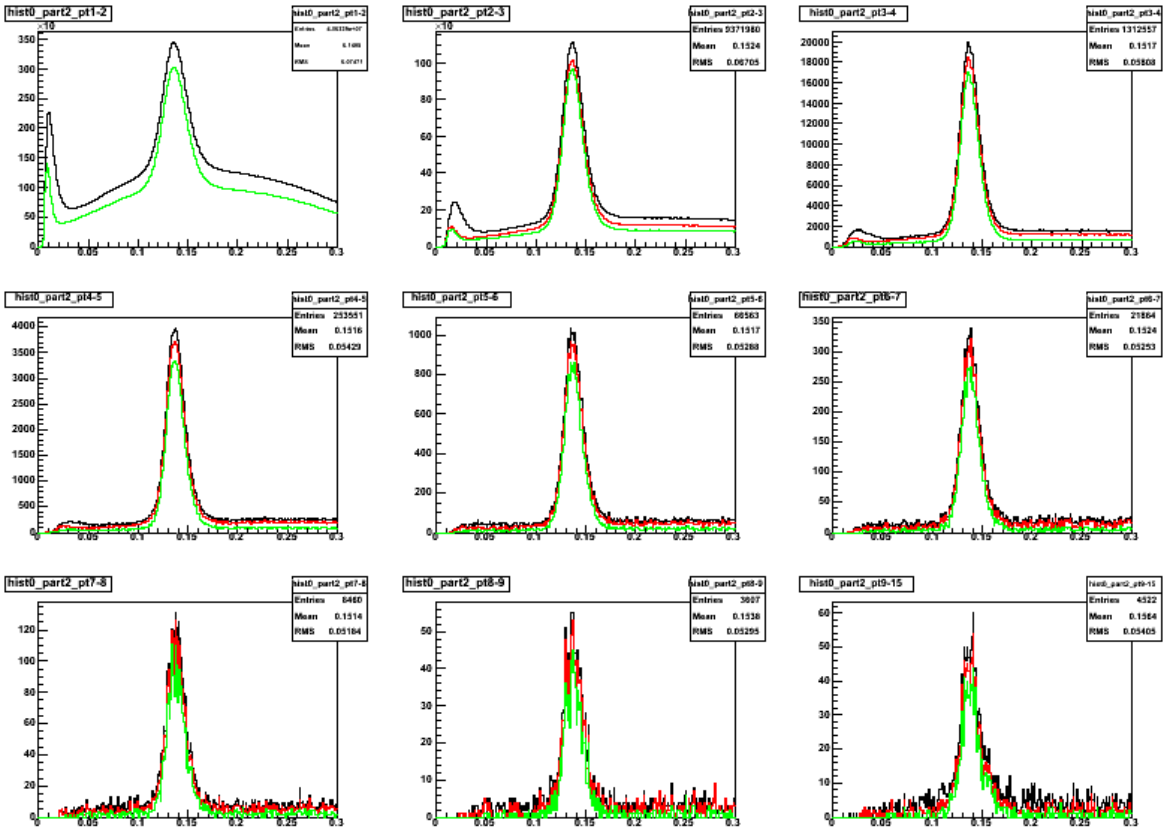

Figure 7.4 Photon pair invariant mass spectra of PbGl at east arm with p_T in various range in the order of left to right and top to bottom. Black lines indicate the spectra by applying minimum photon energy cut in all reconstructed π^0. Red lines indicate the spectra by applying additional *photon_prob* cut based on black lines. Green lines indicates the spectra by applying additional di-photon energy asymmetry cut based on red lines.

Each track will be assigned a 6 bit word to represent its basic quality. From low to high, each bit means:

- bit 0: This track has sufficient X1 hits;
- bit 1: This track has sufficient X2 hits;
- bit 2: This track has UV information;
- bit 3: This track has a unique set of UV hits;

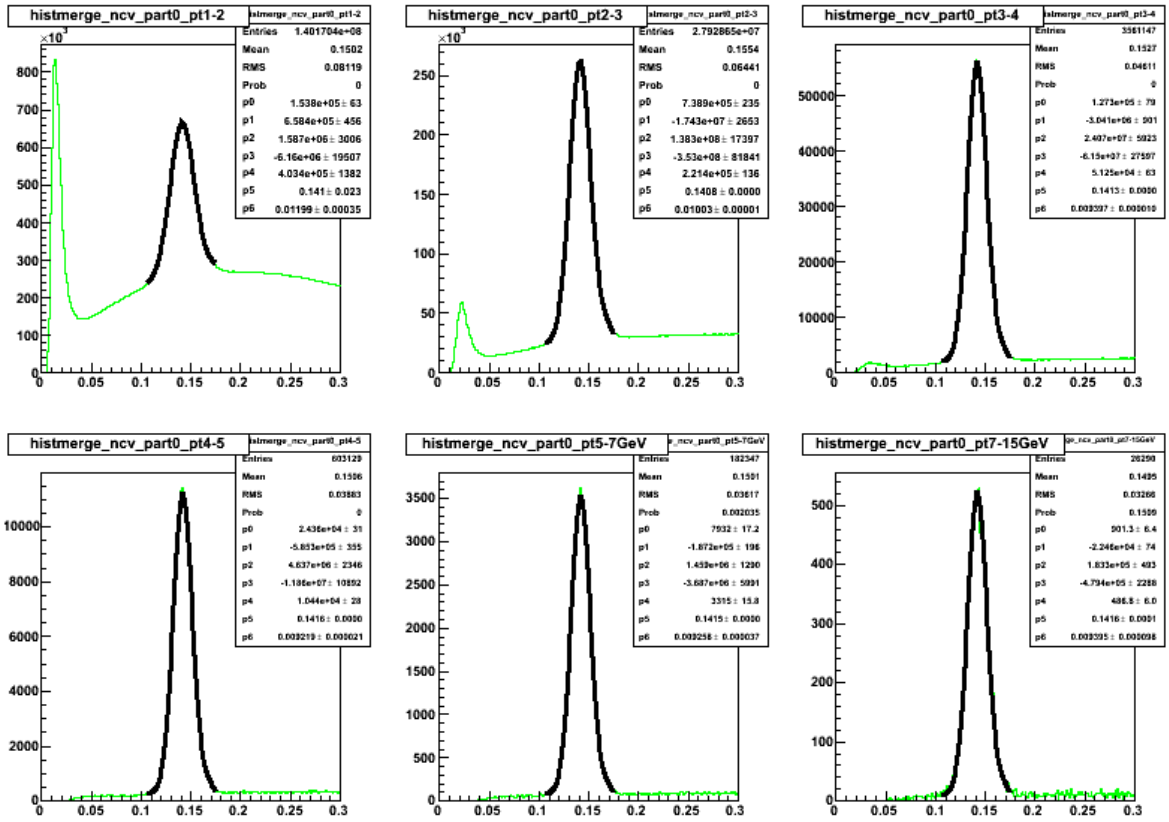

Figure 7.5 Photon pair invariant mass spectra is fit by a Gaussian function plus a 3rd order polynomial in various p_T region.

- bit 4: This track has matched PC1 hits (falling within the window of the DC track's projectionto PC1)
- bit 5: This track has a uniquely matched PC1 hits.

In this analysis, a track with quality being equal to 63 (all bits fired) or 31 (only bit 5 not fired) is considered as a good track.

Also, it is possible that a track hits the edge of DC detector and cross out the side boundary, and thus is reconstructed inaccurately. This can also bring unexpected error to our charged efficiency calculation. To avoid this case, we required a fiducial cut $z_{DC} < 70$cm, so that tracks hitting the edge of the DC and PC will not be included in my analysis.

When a track passes the quality cut at first step, it could be a real charged particle instead of "ghost" track, such as the random combination of DC and PC1 hits. However, it is still not sufficient. For example, conversion or decay tracks may be reconstructed with an incorrect momentum information, because the current reconstruction assumes all charged tracks come from collision vertex. This usually cause a much higher reconstructed momentum than the real momentum.

In order to reduce such tracks, we need use hits from outer layers of PC and EMCal to match the track reconstructed by DC and PC1. Since PC2 is only installed at the west arm, PC3 matching is used in our analysis. We calculate how the reconstructed charged track from DC and PC1 propagate in the magnetic field remnant, and then project this track to PC3 panels. If a real PC3 hit is found within the certain range of the projection, this track would be a good track. Otherwise, the track could still be a good track if it missed PC3 matching because it happened to hit PC3 dead area. Thus this track will be projected to Emcal to see if a EMCal hit could match the track. The track will be kept when Emcal matching works, otherwise it will be abandoned. The difference between projection and hits will then be plotted in both ϕ (pc3dphi/emcdphi) and z (pc3dz/emcdphi) direction and fitted in Gaussian. The σ of Gaussian for both pc3dphi and pc3dz are written into data and called pc3sdphi/emcsdphi and pc3sdz/emcsdz. Naturally, such distribution should be a normal Gaussian, centered at 0 and $\sigma = 1$. In practice, these distributions are double Gaussian instead of single Gaussian, in which the narrow Gaussian is the signal and the wide Gaussian is the background. The narrow Gaussian could have a little shift away from the center 0 and the σ may not be exactly equal to 1. It was also found that the distribution of pc3dphi/emcsdphi and emcsdz/pc3dz can be charge and p_T dependent as shown in Figure 7.6− 7.13. Table 7.2 shows that the average mean and σ of narrow Gaussian for pc3dphi, pc3dz, emcdphi and emcdphi. In this analysis, we used 3σ (σ is from the narrow Gaussian) matching cut for all these PC3 and Emcal matching.

Since we need charged hadrons only, electrons should be excluded from data sample. Thus, we need project charged tracks to RICH radiation rings. Charged hadrons with $p_T < 4.7$GeV will not radiate Cherenkov light in the PHENIX RICH detectors and thus should have zero

Table 7.2 The averaged means and widths (σ) are used for PC3/EMC matching.

	h^+		h^-	
	Mean	Width	Mean	Width
pc3sdphi	-0.12	1.05	-0.12	1.05
pc3sdz	-0.37	1.00	-0.35	1.00
emcsdphi	-0.05	1.06	-0.09	1.05
emcsdz	-0.10	1.17	-0.08	1.19

coincidence with RICH radiation rings which indicate $n0 \leq 0$. Figure 7.14 shows that this cut does remove electrons since EMCal energy deposit (e) of an electron over its momentum is usually near 1. We did not include $p_T > 4.7$GeV charged tracks in our analysis. Due to large background for the charged tracks at $p_T < 1.4$GeV, we did not use them either.

All cuts used for charged hadron selection are listed as following:

- quality = 31‖63;
- $|z_{DC}| < 70$cm;
- Matching pc3sdphi, pc3sdz in 3σ;
- Matching emcsdphi, emcsdz in 3σ when PC3 matching is not associate with the track;
- $1.4 < p_T < 4.7$GeV
- $n0 \leq 0$

7.2.5 Pair Cut

A particular event may have more than one trigger π^0s and associated charged hadrons survived in all track quality cuts. We only choose the largest p_T triggered π^0 and associated charged hadron as leading hadrons, and then make correlation. Since we are interested in back-to-back di-hadron, we also require the angle between $\vec{p}_T$ of triggered π^0 and associated charged hadron to be larger than $\frac{\pi}{2}$.

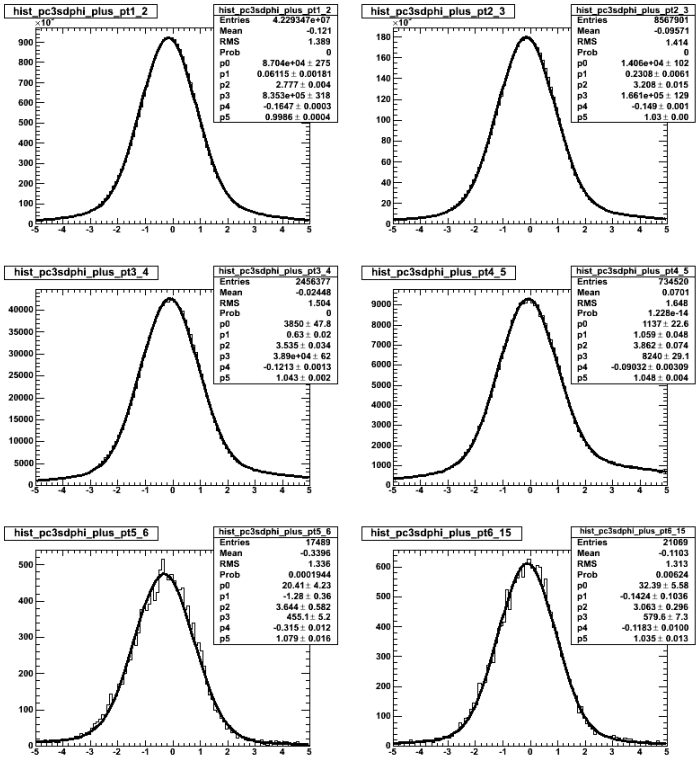

Figure 7.6 The pc3sdphi distribution by using double Gaussian fitting for positive charged tracks in p_T range of $1-2$, $2-3$, $3-4$, $4-5$, $5-6$ and $6-15$GeV in order of left to right and top to bottom, where parameters p1, p2 are mean and width of wide (background) Gaussian, p4 and p5 are mean and sigma of narrow (signal) Gaussian.

7.3 The Asymmetry of Di-Hadron Correlations

As we discussed in Chapter 6, there are two methods to calculate the asymmetry: relative luminosity formula and square root formula. Due to the low statistics, we calculate the left-right asymmetry by using square root formula because it has an advantage that no luminosity correction is needed. Before calculating the asymmetry, we need introduce our physical observables first.

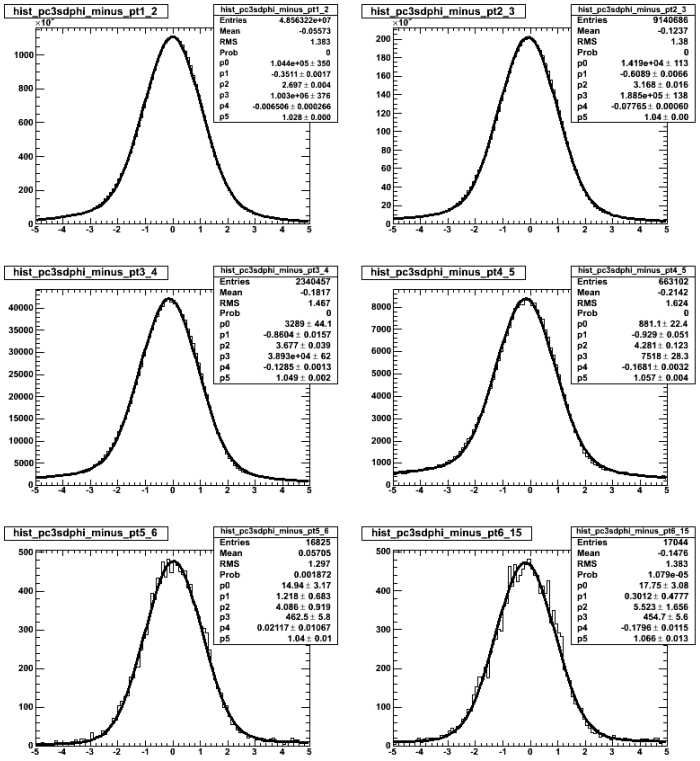

Figure 7.7 The pc3sdphi distribution by using double Gaussian fitting for negative charged tracks in p_T range of $1-2$, $2-3$, $3-4$, $4-5$, $5-6$ and $6-15$GeV in order of left to right and top to bottom, where parameters p1, p2 are mean and width of wide (background) Gaussian, p4 and p5 are mean and sigma of narrow (signal) Gaussian.

7.3.1 q_{Ty} and q_{Tx}

As we discussed in Chapter 2, we introduce the sum of two leading back-to-back hadrons transverse momentum q_T (as shown in Figure 2.6) which can be used to replace k_T in di-hadron correlation. The q_T projection on y-axis - q_{Ty} component should be similar with k_{Ty} which is sensitive to the asymmetry because the spin orientation in Run6 is along x-axis in PHENIX coordinate. q_{Tx} should not be sensitive to the asymmetry.

7.3.2 Square root formula

The di-hadron asymmetry and its statistical error can be calculated by

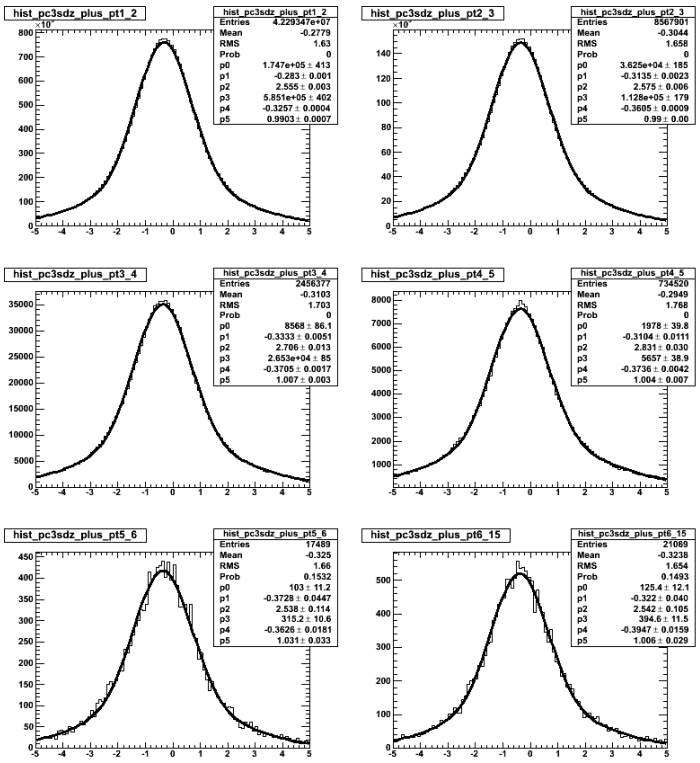

Figure 7.8 The pc3sdz distribution by using double Gaussian fitting for positive charged tracks in p_T range of $1-2$, $2-3$, $3-4$, $4-5$, $5-6$ and $6-15$GeV in order of left to right and top to bottom, where parameters p1, p2 are mean and width of wide (background) Gaussian, p4 and p5 are mean and sigma of narrow (signal) Gaussian.

$$A_N^{DH} = \frac{1}{P}\frac{\sqrt{N_-^{\uparrow}N_+^{\downarrow}} - \sqrt{N_-^{\downarrow}N_+^{\uparrow}}}{\sqrt{N_-^{\uparrow}N_+^{\downarrow}} + \sqrt{N_-^{\downarrow}N_+^{\uparrow}}} \tag{7.2}$$

$$\delta A_N^{DH} = \sqrt{(A_N^{DH}\frac{\delta P}{P})^2 + \frac{N_-^{\downarrow}N_+^{\uparrow}(N_-^{\uparrow}+N_+^{\downarrow}) + N_-^{\uparrow}N_+^{\downarrow}(N_-^{\downarrow}+N_+^{\uparrow})}{P^2(\sqrt{N_-^{\uparrow}N_+^{\downarrow}} + \sqrt{N_-^{\downarrow}N_+^{\uparrow}})^4}} \tag{7.3}$$

where A_N^{DH} is the di-hadron asymmetry, δA_N^{DH} is the statistical error of the di-hadron asymmetry, P and δP are polarization and its statistical error, N is di-hadron yields and the superscript $\uparrow(\downarrow)$ indicates spin up(down), the subscript -(+) indicates $q_{Ty}(q_{Tx}) < 0$ and $q_{Ty}(q_{Tx}) > 0$.

Since two different ERT trigger circuits were used to record odd and even bunches data

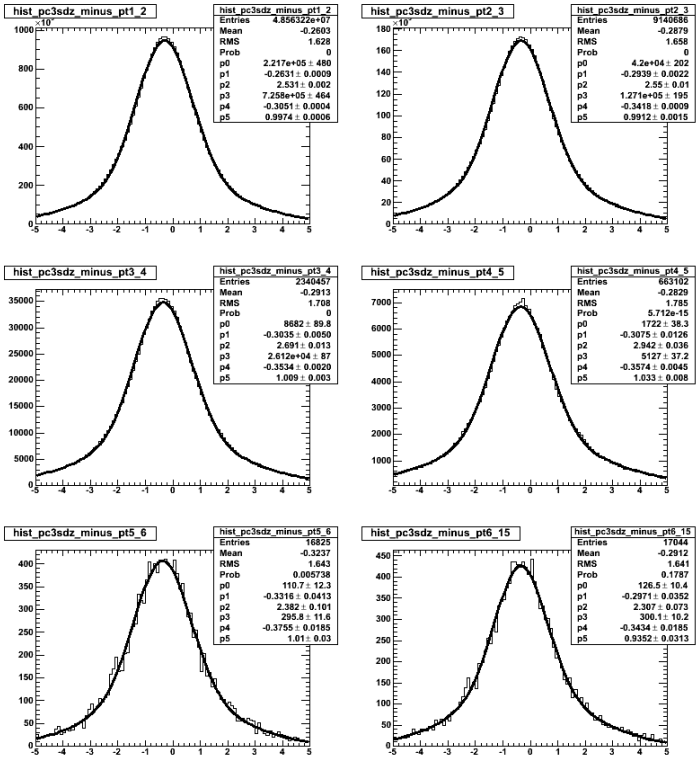

Figure 7.9 The pc3sdz distribution by using double Gaussian fitting for negative charged tracks in p_T range of $1-2$, $2-3$, $3-4$, $4-5$, $5-6$ and $6-15$GeV in order of left to right and top to bottom, where parameters p1, p2 are mean and width of wide (background) Gaussian, p4 and p5 are mean and sigma of narrow (signal) Gaussian.

and it could also cause an asymmetry shift, we calculated the results for even bunches and odd bunches separately, and then combine them by using Eq. 7.4, where δA_N is the statistical error of asymmetry. The Figure 7.15, 7.16 show the fill-by-fill and fill-combined asymmetries for even and odd bunches on q_{Ty} and q_{Tx}. Table 7.3 shows asymmetries and their uncertainties for even, odd and all bunches on q_{Ty} and q_{Tx} for both blue and yellow beams.

$$A_N = \frac{\frac{A_N(even)}{\delta A_N^2(even)} + \frac{A_N(odd)}{\delta A_N^2(odd)}}{\frac{1}{\delta A_N^2(even)} + \frac{1}{\delta A_N^2(odd)}} \tag{7.4}$$

As we know, a fragmented hadron only carries a fraction of jet momentum. Because we are using q_T from back-to-back leading di-hadron instead of k_T from di-jet as physical observable,

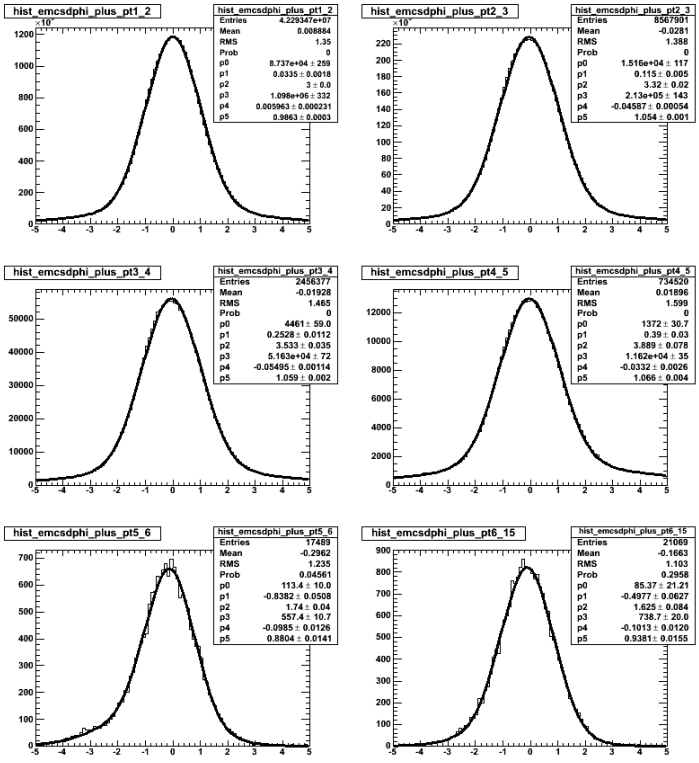

Figure 7.10 The emcsdphi distribution by using double Gaussian fitting for positive charged tracks in p_T range of $1-2$, $2-3$, $3-4$, $4-5$, $5-6$ and $6-15$GeV in order of left to right and top to bottom, where parameters p1, p2 are mean and width of wide (background) Gaussian, p4 and p5 are mean and sigma of narrow (signal) Gaussian.

the difference between hadron and jet momenta could cause a smearing in the asymmetry. Also the central arms of PHENIX do not have full 2π acceptance, which could also cause the measured asymmetry different from the real asymmetry. All of these effects need be understood by Monte-Carlo simulation that will be discussed later.

7.3.3 Bunch Shuffling

Bunch shuffling is used to check for any spin related systematic bias and verify the uncertainties to be correctly calculated. In this analysis, it was done by replacing random spin orientation for both blue and yellow beams and then calculate the asymmetries. 5000 runs of bunch shuffling for fill by fill q_{Ty} and q_{Tx} asymmetries and χ^2/NDF calculated by square

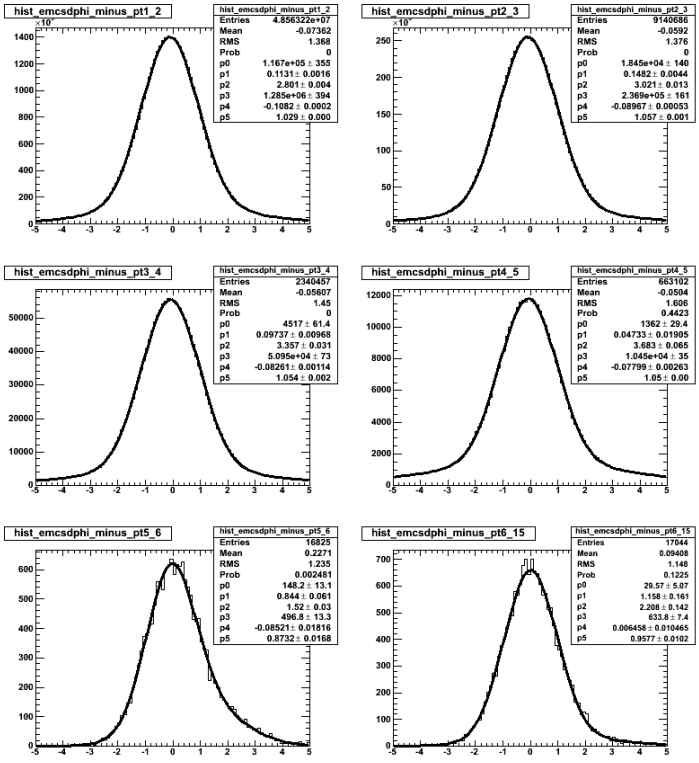

Figure 7.11 The emcsdphi distribution by using double Gaussian fitting for negative charged tracks in p_T range of $1-2$, $2-3$, $3-4$, $4-5$, $5-6$ and $6-15$GeV in order of left to right and top to bottom, where parameters p1, p2 are mean and width of wide (background) Gaussian, p4 and p5 are mean and sigma of narrow (signal) Gaussian.

root formula on both blue and yellow beam have been done as Figure 7.17, and the mean and width of fitting Gaussian equation are in Table 7.4. From this table, we can see asymmetries in random spins are center at 0, and the width of fitting asymmetries matches the statistical errors very well.

7.3.4 Correction for acceptance and fragmentation

We used a toy Monte Carlo simulation to find out how the asymmetry expected due to the Sivers effect in di-jet collisions is seen through di-hadron correlation measurements in the PHENIX detector. These calculations are intended to elucidate how such an asymmetry would be visible in the PHENIX detector, as well as the effects of finite acceptance and the sensitivity

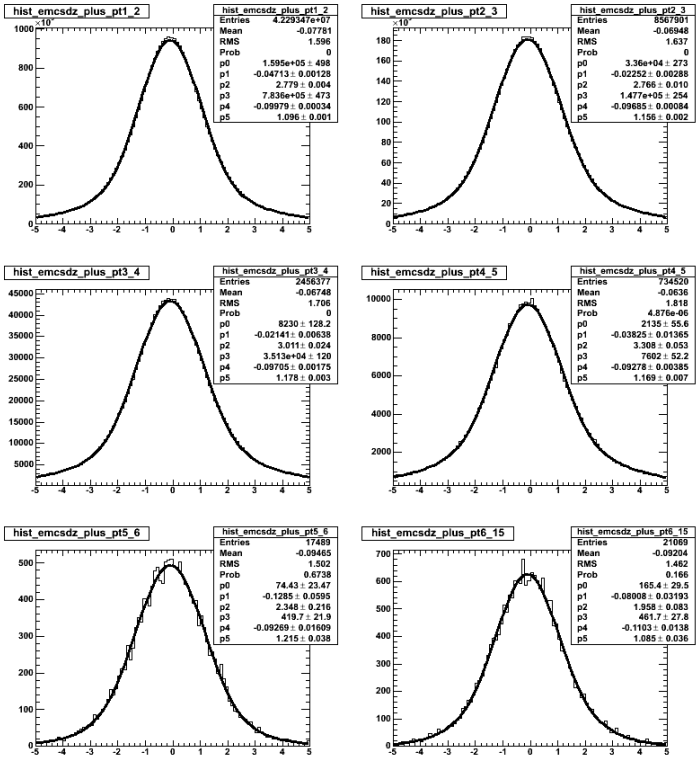

Figure 7.12 The emcsdz distribution by using double Gaussian fitting for positive charged tracks in p_T range of $1-2$, $2-3$, $3-4$, $4-5$, $5-6$ and $6-15$GeV in order of left to right and top to bottom, where parameters p1, p2 are mean and width of wide (background) Gaussian, p4 and p5 are mean and sigma of narrow (signal) Gaussian.

to fragmentation functions. The full details about the simulation can found in [34]. Here we will briefly discussed the results.

In order to study how the limited acceptance of PHENIX and fragmentation affect the measured asymmetry, we include the acceptance dilution factor and fragmentation dilution factor in Eq. 7.2 to achieve the full di-jet asymmetry as Eq. 7.5 shown.

$$A_N^{DH} = \frac{1}{P}\langle f\rangle\langle a\rangle \frac{\sqrt{N_-^{\uparrow}N_+^{\downarrow}} - \sqrt{N_-^{\downarrow}N_+^{\uparrow}}}{\sqrt{N_-^{\uparrow}N_+^{\downarrow}} + \sqrt{N_-^{\downarrow}N_+^{\uparrow}}} \tag{7.5}$$

where $\langle f\rangle$ represents the fragmentation correction, and $\langle a\rangle$ represents the correction factor due to limited acceptance.

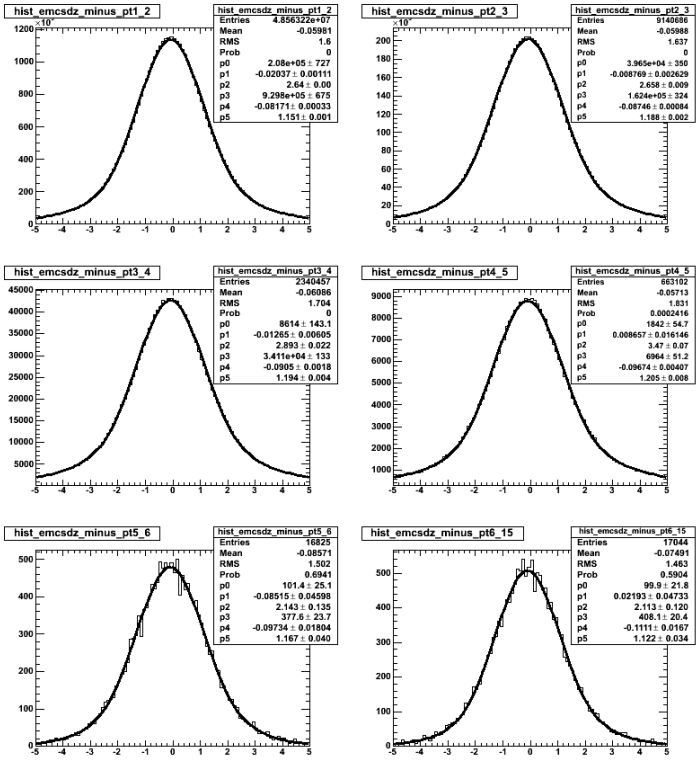

Figure 7.13 The emcsdz distribution by using double Gaussian fitting for negative charged tracks in p_T range of $1-2$, $2-3$, $3-4$, $4-5$, $5-6$ and $6-15$GeV in order of left to right and top to bottom, where parameters p1, p2 are mean and width of wide (background) Gaussian, p4 and p5 are mean and sigma of narrow (signal) Gaussian.

In the toy Monte Carlo simulation, we parametrize the pythia output to inject a di-jet asymmetry in k_{Ty} and then calculate the output asymmetry from two leading fragmented hadrons correlation in limited PHENIX acceptance as we did in real data analysis. By comparing the input and output asymmetry, we can know how much the acceptance and fragmentation factors are.

Before describing the toy MC in detail, it is necessary to first describe the pythia simulation that the toy MC was tuned to. QCD hard scattering events (subprocesses 11,12,13,28,53,68) were run for 200GeV $p+p$ collisions using the PHENIX wrapper PHPythia. The Gaussian intrinsic k_T factor was increased from 1.0GeV to 1.5GeV (MSTP[91]=1 and PARP[91]=1.5) to better match the PHENIX data (see [35]) and a minimum parton p_T of 5.0GeV was selected

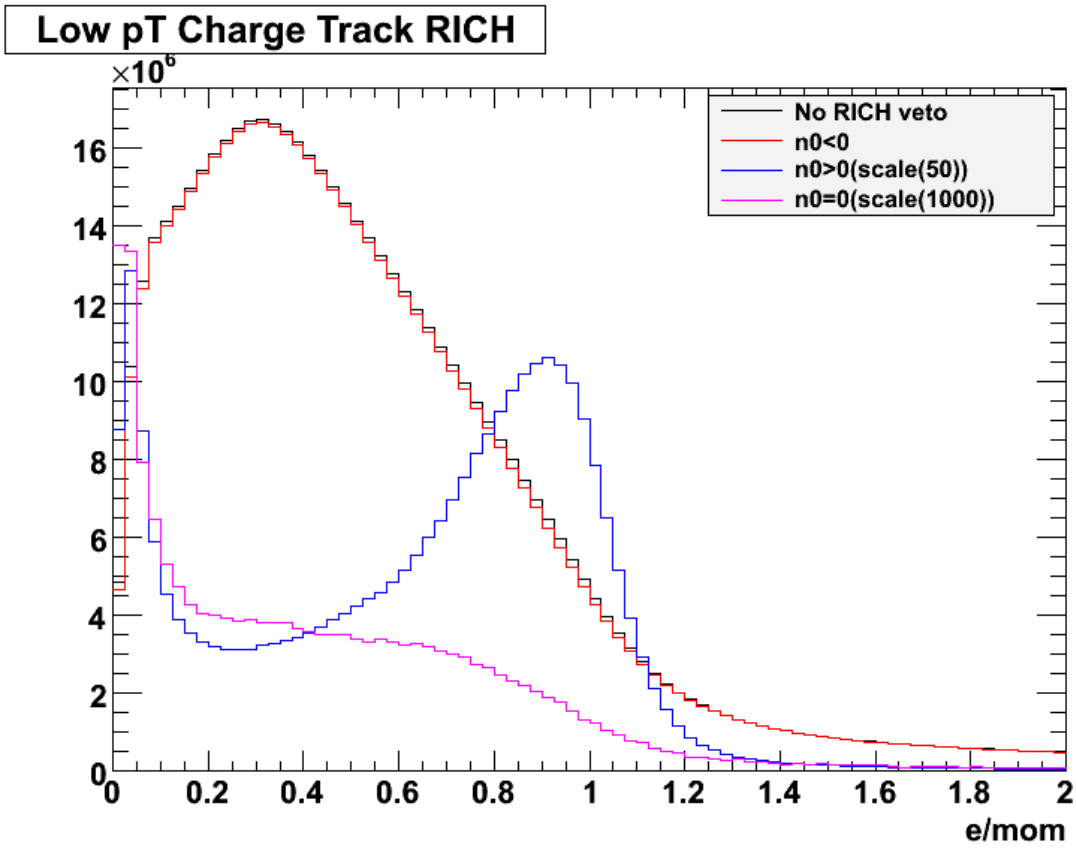

Figure 7.14 e/mom spectra for low p_T ($p_T < 4.7$GeV) charged tracks for various RICH cuts. The blue line shows e/mom has a peak near 1 when using the RHIC cut $n0 > 0$, which essentially indicate electron signal. The spectra by using $n0 < 0$ and $n0 = 0$ cut do not show the electron signal.

(CKIN[3]=5.0). Approximately 50M events were generated for this study. These events could be passed through various acceptance filters when analyzed (described below) and used to provide both parameterizations and comparisons with the toy MC.

The toy Monte Carlo that we have written proceeds as follows:

1. For each pair to be generated, a vertex and spin orientation are generated. The vertex distribution is Gaussian with a sigma of 23cm. The vertex is required to be within +/- 30 cm.

2. The type of process is generated, where "processes" are characterized by the final state

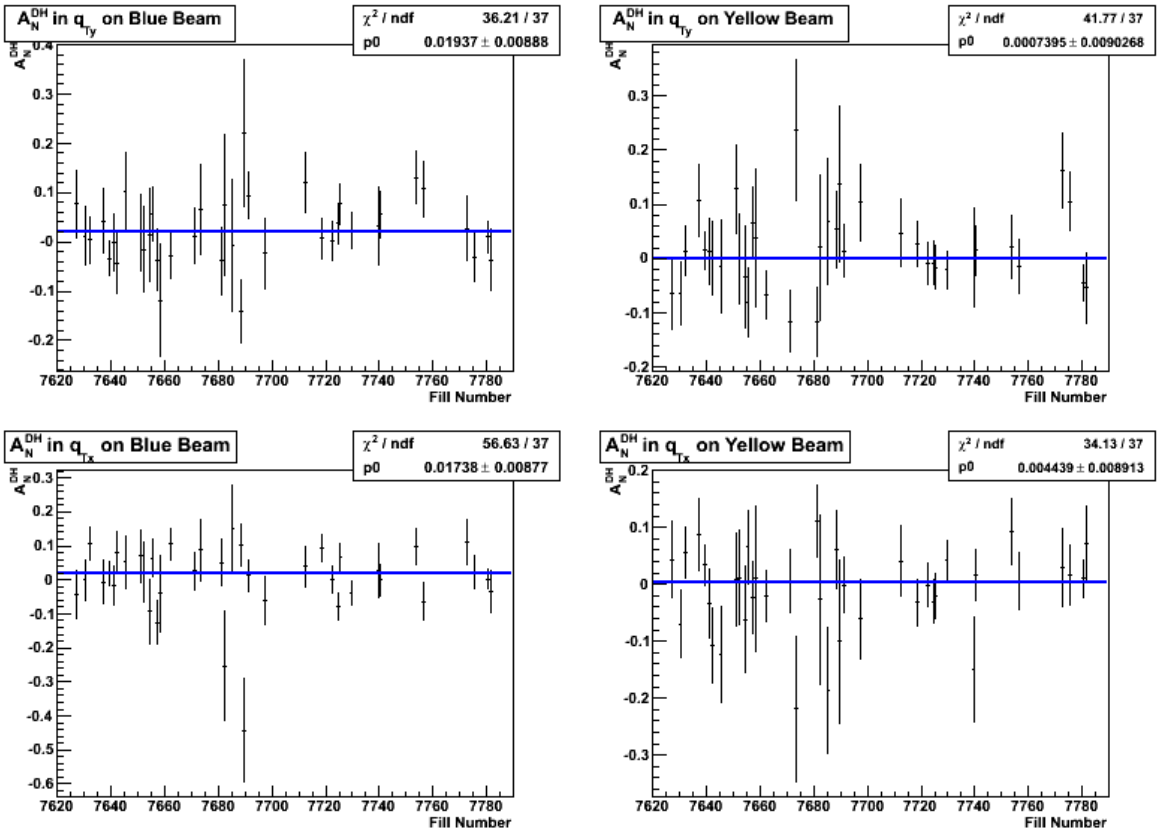

Figure 7.15 Fill-by-fill physics asymmetries in qty and qtx for even bunches on blue and yellow beams which are calculated by square root formula. Constant fittings were applied to figure out fill combined asymmetries which are shown as blue solid lines. "p0"s on top-right box is the value of fill-combined asymmetries.

partons that will be fragmented - qq, qg or gg. These probabilities are chosen based on the pythia Monte Carlo averaged over the p_T range as 0.12, 0.54 and 0.34, respectively.

3. Next, a parton pair is generated by choosing q-squared value for the interaction. The q-squared distribution used is a power-law fit to the q-squared distribution in pythia events (see Figure 7.18). The parton p_T is taken to be the square-root of q-squared. The angular distribution in ϕ is chosen to be isotropic from 0 to 2π.

4. At this point a partonic k_T is chosen in both k_{Tx} and k_{Ty} as a Gaussian distribution with a 1.5GeV sigma. An asymmetry can be injected at this point by shifting the k_{Ty}

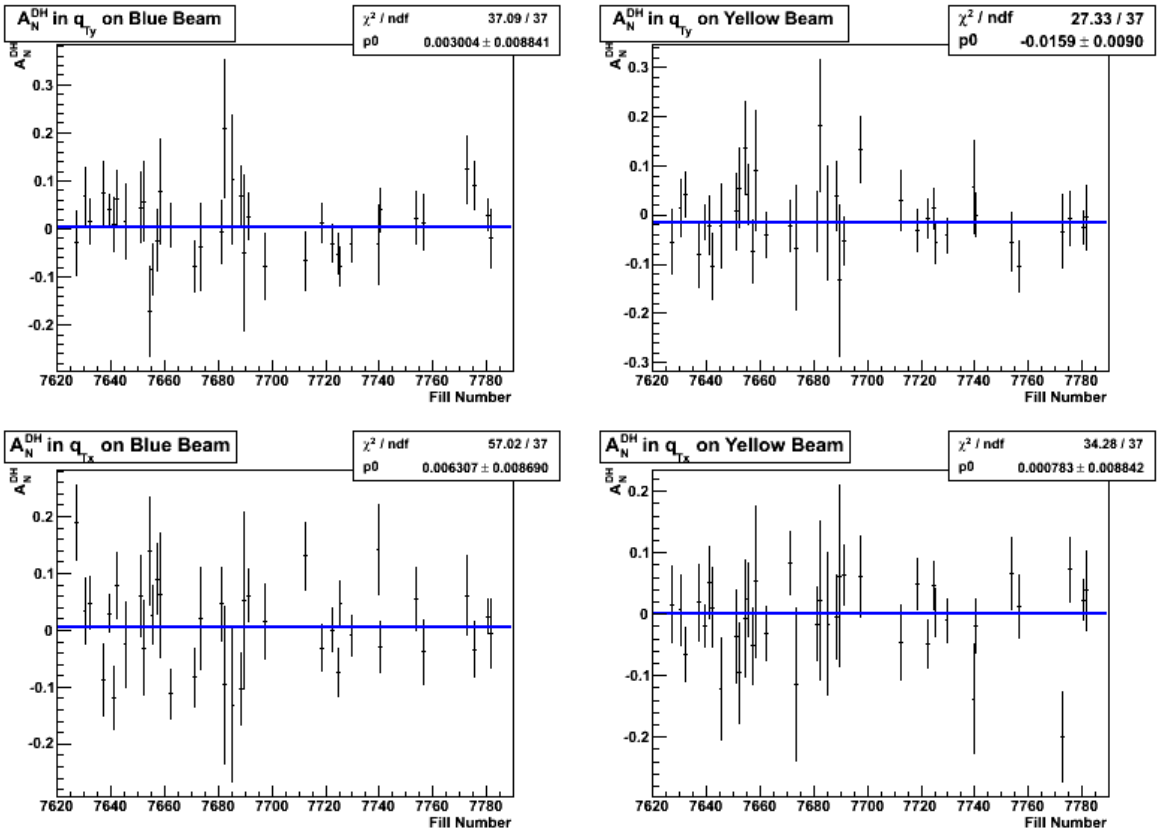

Figure 7.16 Fill-by-fill physics asymmetries in qty and qtx for odd bunches on blue and yellow beams which are calculated by square root formula. Constant fittings were applied to figure out fill combined asymmetries which are shown as blue solid lines. "p0"s on top-right box is the value of fill-combined asymmetries.

value by a chosen fraction of the Gaussian sigma (1%, 5%, 10%, etc.). This k_T is used to modify the magnitude and direction of the momentum vector of one of the scattered partons. This mimics the Sivers effect at the partonic level for q_{Ty}. For q_{Tx} it can be used to investigate the acceptance and fragmentation effects, but for the Run-6 data it would not represent the Sivers effect.

5. At this point the scattered partons are fragmented using quark and gluon fragmentation functions, based on the subprocess final state chosen in (2). The fragmentation functions used are taken from [36], which includes a recent global analysis of fragmentation functions for charged hadrons. The quark fragmentation function used the parameterization

Table 7.3 Fill integral asymmetries, uncertainties and χ^2 calculated by square root formula for even, odd and all bunches on q_{Ty} and q_{Tx} for both blue and yellow beams.

	Asymmetry($\times 10^{-2}$)	Stat. Uncertainties($\times 10^{-2}$)	χ^2/NDF
q_{Ty} blue (even bunches)	1.94	0.89	0.981
q_{Ty} blue (odd bunches)	0.30	0.88	1.002
q_{Ty} blue (all bunches)	1.12	0.63	0.709
q_{Ty} yellow (even bunches)	0.07	0.90	1.129
q_{Ty} yellow (odd bunches)	-1.59	0.90	0.739
q_{Ty} yellow (all bunches)	-0.76	0.64	0.973
q_{Tx} blue (even bunches)	1.74	0.88	1.531
q_{Tx} blue (odd bunches)	0.63	0.87	1.541
q_{Tx} blue (all bunches)	1.18	0.62	1.536
q_{Tx} yellow (even bunches)	0.44	0.89	0.922
q_{Tx} yellow (odd bunches)	0.08	0.88	0.926
q_{Tx} yellow (all bunches)	0.26	0.63	0.976

for light quarks only, and ignores the different fragmentation fits for charm and bottom quarks. The fragmentation functions are shown in Figures 7.19 and 7.20. (Note, in particular how much more "hard" the gluon fragmentation function is compared to that for quarks.)

6. Finally, the transverse momentum of each "hadron" determined in (5) is smeared using a Gaussian j_T to represent the intrinsic momentum in the fragmentation process. The parameter $\sqrt{\langle j_T^2 \rangle}$ was taken as 0.585 GeV, again from [35].

7. The parton pair was then subjected to a set of analysis cuts intended to represent the PHENIX detector and analysis described in previous section. If any cut fails, the pair is regenerated starting with step (2). To start with, a randomly chosen hadron from (6) is taken to be a π^0 and is required to have a $p_T > 3.0$GeV/c. If it passes the minimum transverse momentum cut, it is then decayed into photons and each photon is checked to see if it is in the PHENIX acceptance using a simple geometric acceptance model. If the π^0 passes the acceptance filter, it is taken as the trigger hadron in the pair and the second particle in the pair is checked as the associated hadron. The associated

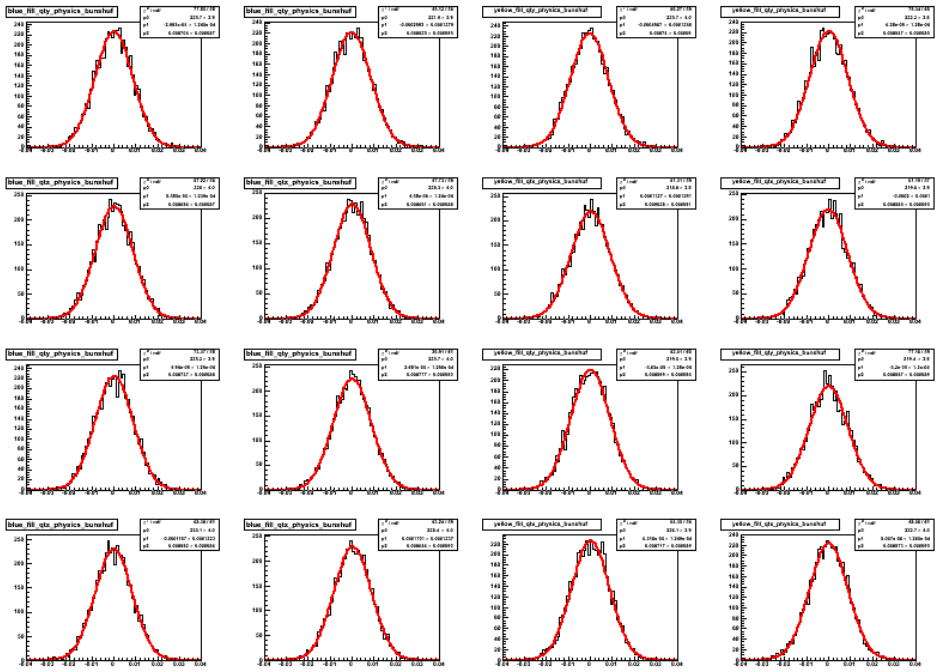

Figure 7.17 5000 times of bunch shuffling fill-combined asymmetries calculated by square root formula for even (first and third column) and odd (second and fourth column) bunches in q_{Ty}(first row) and q_{Tx} (second row) on blue beam, q_{Ty}(third row) and q_{Tx} (four row) on yellow beam were filled in histograms and then fit by Gaussian.

hadron is chosen as to have charge +,-,0 with equal probability and is assumed to be a pion. The exception to this is if the associated hadron p_T is higher than the trigger hadron p_T, in which case the associated hadron is chosen to be either + or - only. The associated particle is subjected to a set of transverse momentum cuts ($1.4 < p_T < 4.7$ GeV/c for charged pions, $p_T > 2.0$GeV/c for π^0's and checked against the same PHENIX acceptance filter used for the trigger hadron. As before, π^0's are decayed into photons and each photon is checked to see if it is in the acceptance.

8. If both the trigger and associated hadron pass all cuts, the pair is accepted and the pair kinematics are stored in an output ntuple. The results shown later in this note are based on the simulation of 1 million pairs using the above outlined procedure.

One million pairs were generated using both "perfect" and "PHENIX" acceptance with

Table 7.4 Fill-combined bunch shuffling asymmetries calculated by square root formula in q_{Ty} and q_{Tx} for even and odd bunches on blue and yellow beams

Scale	1		2		Uncertainties
$\times 10^{-2}$	Mean	Width	Mean	Width	from calculation
q_{ty} blue beam (even bunch)	-0.003	0.87	0.005	0.87	0.89
q_{ty} blue beam (odd bunch)	0.026	0.89	0.003	0.88	0.88
q_{ty} yellow beam (even bunch)	-0.046	0.87	-0.006	0.90	0.90
q_{ty} yellow beam (odd bunch)	0.006	0.88	-0.005	0.90	0.90
q_{tx} blue beam (even bunch)	0.009	0.87	-0.011	0.86	0.88
q_{tx} blue beam (odd bunch)	0.005	0.87	0.017	0.86	0.87
q_{tx} yellow beam (even bunch)	0.011	0.90	0.006	0.87	0.89
q_{tx} yellow beam (odd bunch)	-0.002	0.90	0.008	0.89	0.88

fragmentation by injecting asymmetries of 0%, 1%, 2.5%, 5%, 7.5% and 10%. The output asymmetries in q_{Ty} calculated by using the squareroot formula are plotted against the input asymmetries in Figure 7.21. In order to separate the acceptance and fragmentation correction factors, we did the same work without fragmentation as shown in Figure 7.22. Then we can extract the fragmentation and acceptance dilution factors for q_{Ty} asymmetries as shown in Table 7.5. The factors for q_{Tx} can also be extracted as shown in Table 7.5.

Table 7.5 Asymmetry correction factors q_{Ty} and q_{Tx} from the toy MC for the "perfect" and PHENIX acceptance cases. Errors shown are statistical only.

	$a(q_{Ty})$	$f(q_{Ty})$	$a(q_{Tx})$	$f(q_{Tx})$
"Perfect" Acceptance	0.93 ± 0.01	1.53 ± 0.02	0.93 ± 0.01	1.45 ± 0.02
PHENIX Acceptance	1.18 ± 0.01	1.48 ± 0.02	0.81 ± 0.01	1.69 ± 0.02

7.4 The result

Applying the correction factors of acceptance and fragmentation, the asymmetries in q_{Ty} and q_{Tx} for both blue and yellow beams by back-to-back leading di-hadron correlation at mid-rapidity are shown in Figure 7.23, which has been approved as a PHENIX preliminary result. According to the Sivers function, the asymmetries of q_{Ty} for two beams should be opposite

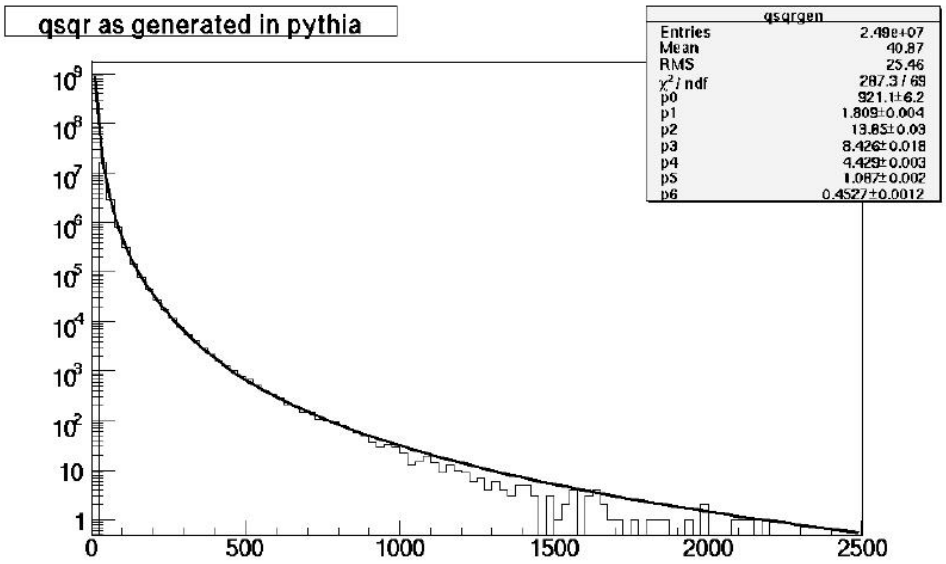

Figure 7.18 The q-squared distribution generated in pythia events and the power-law fit used in the toy MC.

sign. At mid-rapidity, the single transverse spin asymmetry of di-hadron correlation is sensitive to the gluon Sivers function. This result shows that the asymmetry of di-hadron correlation at mid-rapidity is consistent with zero, which may indicate that the gluon Sivers function is very small.

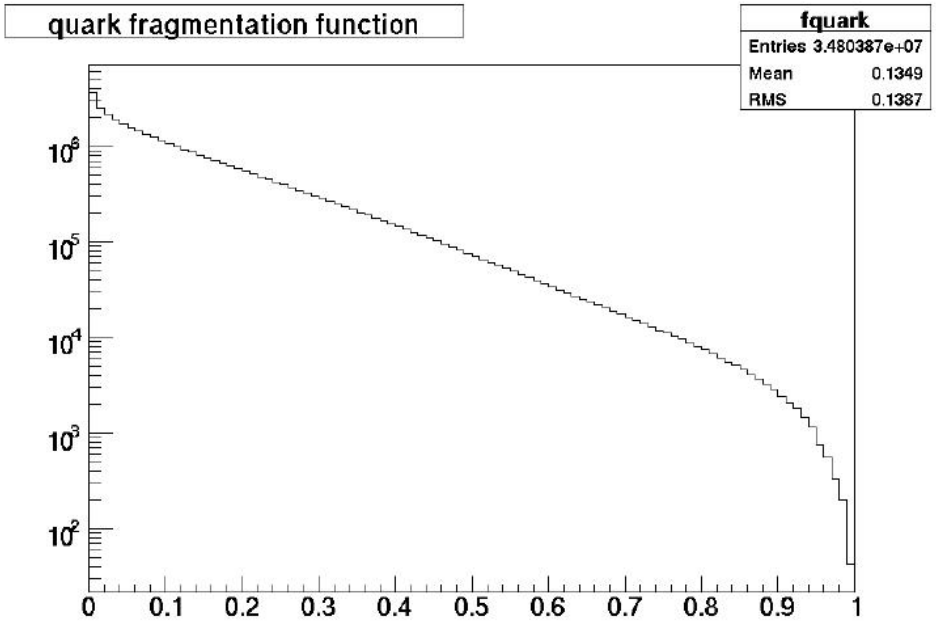

Figure 7.19 The quark fragmentation function used in the toy MC. The horizontal axis is partonix x, while the vertical axis is dN/dx.

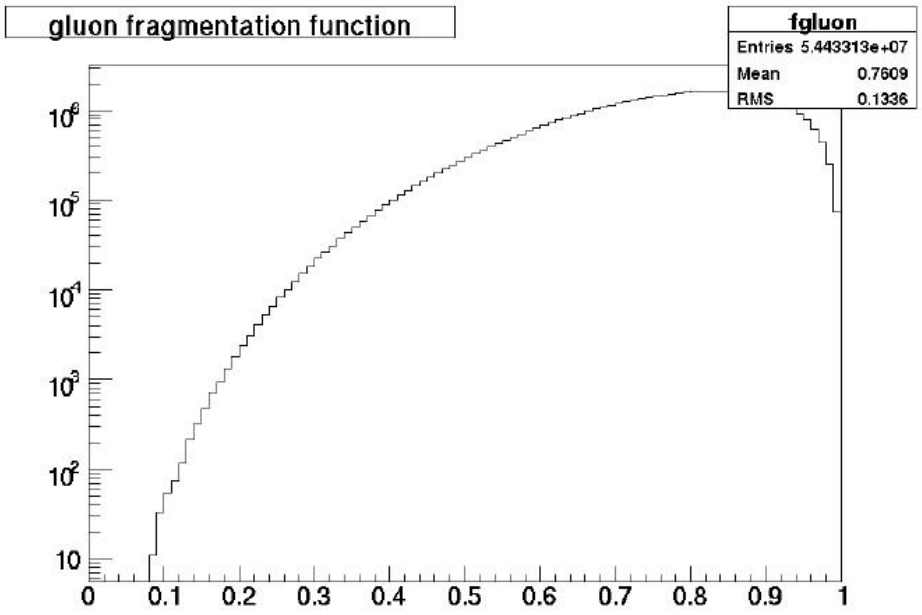

Figure 7.20 The gluon fragmentation function used in the toy MC. The horizontal axis is partonix x, while the vertical axis is dN/dx.

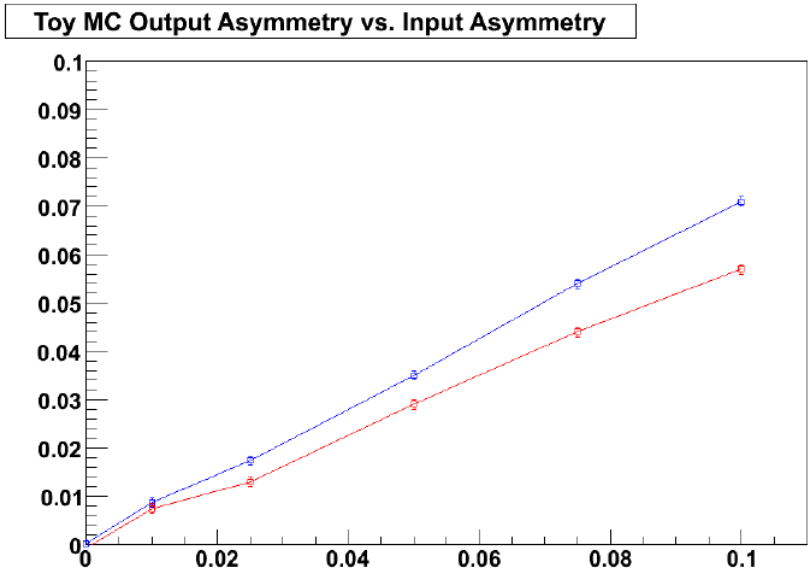

Figure 7.21 Output asymmetry (y-axis) vs. input asymmetry (x-axis) in q_{Ty} using the toy MC. The blue curve is for "perfect" acceptance, while the red curve is for the modeled PHENIX acceptance.

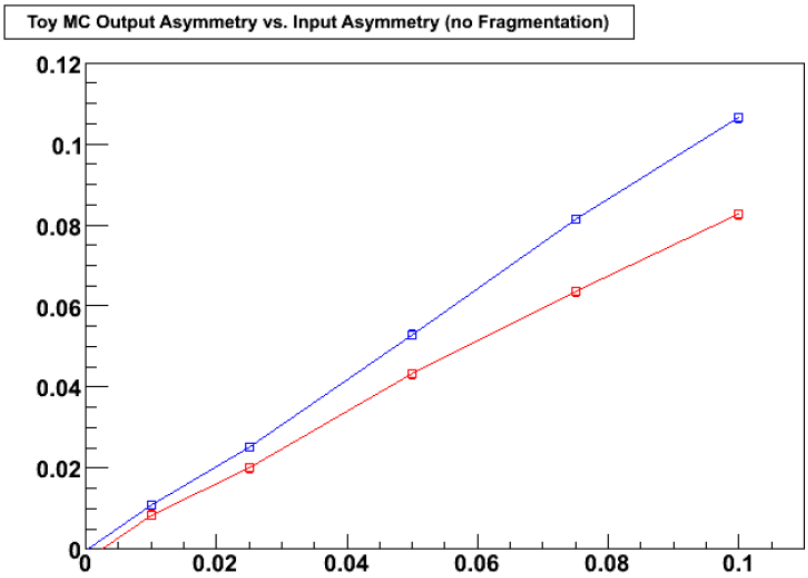

Figure 7.22 Output asymmetry (y-axis) vs. input asymmetry (x-axis) in q_{Ty} using the toy MC without fragmentation. The blue curve is for "perfect" acceptance, while the red curve is for the modeled PHENIX acceptance.

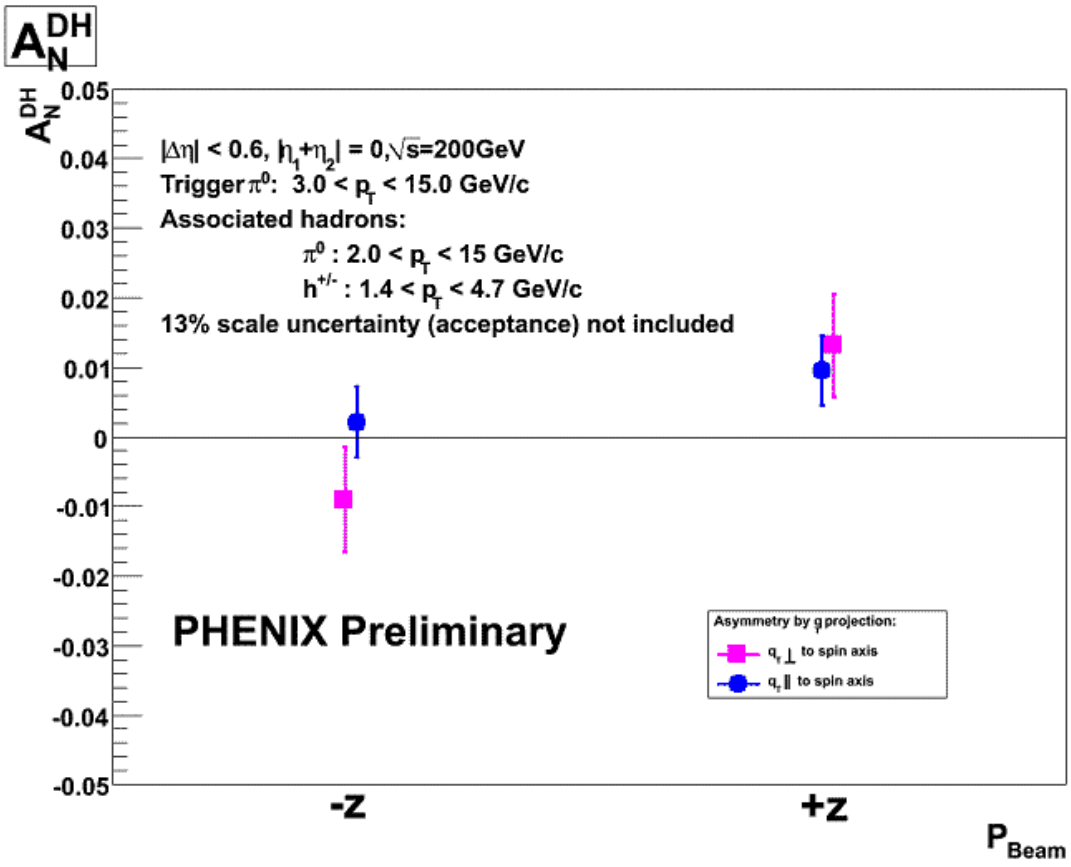

Figure 7.23 The di-hadron asymmetries q_{Ty} (called $q_T\perp$ in purple color) and q_{Tx} (called $q_T\parallel$ in blue color) for blue (+z) and yellow (-z) in beams.

CHAPTER 8. Conclusion and Outlook

8.1 QCD and Spin Physics

Among the essential goals of spin physics, the first one is to understand the nucleon spin structure in terms of its basic partonic constituents and the second one is to test the spin sector of perturbative QCD at the highest possible precision level. Concerning the first point, one needs to know how the quark and gluon distributions in a polarized nucleon make its spin $\frac{1}{2}$. The second point is very relevant to reinforce the validity of the already well established perturbative QCD theory, because many spin asymmetries have been calculated, at the next-to-leading order (NLO), and have not yet been compared with experimental data.

The current activities in QCD spin physics involve, in particular, the phenomenological description of parton distributions in the framework of a statistical approach. It can be applied equally well to unpolarized and polarized data, a rather unique situation, and it is valid in a wide kinematical range in x and Q^2. It has, so far, a very good predictive power, for both Deep Inelastic Scattering and hadronic collisions recent results. The transverse momentum dependence of the parton distributions has been also included, because its relevance has been realized in connection with transverse spin effects and orbital angular momentum contributions. The spin physics program of the polarized $p+p$ collider at RHIC, operating since 2001, have made measurements of double helicity and single transverse spin asymmetries in various channels. It reaches the energy of $\sqrt{s} = 500$GeV, allowing the gauge bosons $W^{\pm}$ and Z production and the measurement of the parity-violating asymmetries since 2009.

8.2 Conclusion

In this thesis, we present the measurement of single transverse spin asymmetry, A_N, for non-identified charged hadron by using muon spectrometer ($1.2 < |\eta| < 2.4$) at $\sqrt{s} = 200$GeV transversely polarized $p + p$ collision. A number of systematic checks have been performed. The dominant asymmetry dilution and mixing effects has been studied. The bin sharing effects have been corrected by using matrices extracted from the Monte-Carlo simulation.

The exploration of transverse spin asymmetries in SIDIS and $p + p$ collision needs to investigate the dependence of the asymmetries on the p_T of the hadrons. This raises serious questions about the universality of the distribution and fragmentation functions which can be investigated in both experiment and theory. It has as well forced modelers to include the intrinsic k_T of the partons in some fashion. These issues are being addressed aggressively by the theoretical community. The result from BRAHMS experiment at RHIC only showed the asymmetries respected to p_T up to 2.5GeV. PHENIX has larger p_T acceptance for muon spectrometer which can effectively measure charged hadrons up to 5GeV or higher. The A_N result for foward non-identified charged hadrons has been compared with the forward identified pion measurements from BRAHMS experiment at $\sqrt{s} = 200$GeV transversely polarized $p + p$ collision as shown in Figure 8.1. The figure shows that larger asymmetries are found at PHENIX for the same x_F because of its larger $\langle p_T \rangle$. However, PHENIX result may have a limited constraint to the parameters in pQCD calculation since the muon spectrometers of PHENIX can not identify charged hadrons or measure the fractions of each type of charged hadrons. The pQCD calculation can only be made for particular hadrons such as pions.

Several effects are believed to be potential contributors to the observed asymmetries, which are twist-3, Sivers, and Collins mechanisms. The Sivers function accounts for how a parton's transverse momentum depends on the orientation of the nucleon spin and provides an interesting window into the structure of the nucleon. At present the quark Sivers functions have been constrained by SIDIS experiments and the gluon Sivers function is still not constrained very well.

In this thesis, we present the measurement of the single transverse spin asymmetry via

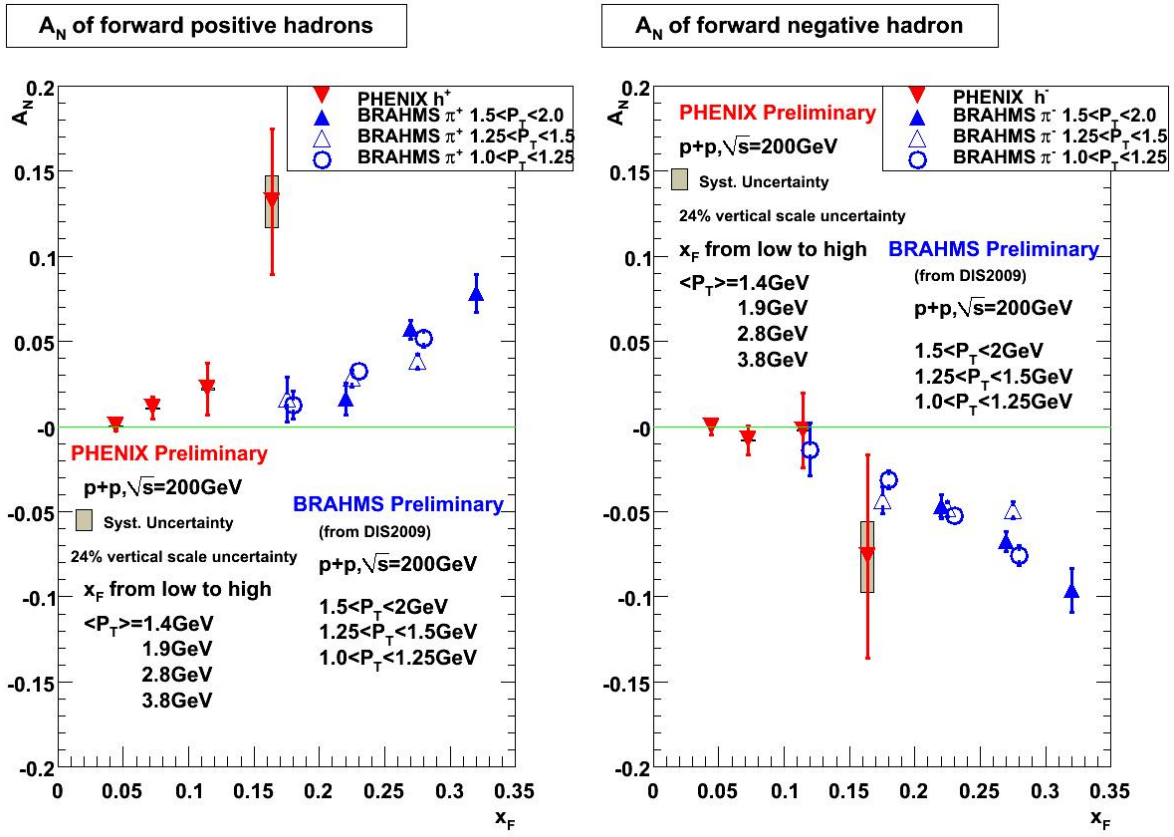

Figure 8.1 The comparison of A_N between foward charged hadron at PHENIX experiment (in red color) and forward charged pion at BRAHMS experiment (in blue color) at $\sqrt{s} = 200\text{GeV}$ $p+p$ collision.

di-hadron correlation in mid-rapidity ($|\eta| < 0.35$) at $\sqrt{s} = 200\text{GeV}$ transversely polarized $p+p$ collision. The dilution effects from acceptance and fragmentation have been studied. In mid-rapidity, the quark Sivers effect is believed to be very small due to current quark Sivers function, the single transverse spin asymmetry is sensitive to the gluon Sivers function. Therefore, this measurement may provide better constraint to the gluon Sivers function.

However, the Sivers function is notable for an unusual "modified" universality property such that the sign of the Sivers distribution as measured in a Drell-Yan process will be opposite the sign of the distribution as measured in DIS. The modified universality is an important test of the QCD gauge-link formalism used to calculate these initial/final state interactions of the

incoming/outgoing parton lines.

The Sivers and Collins mechanisms are using TMD factorization, while twist-3 is using co-linear factorization. A recent paper [37] from T. Rogers and P. Mulders shows that TMD factorization is not valid in high transverse momentum hadron production and co-linear factorization still works. It is very interesting to know how large the violation of TMD factorization is, and if this can be determined for a of measurements at RHIC.

8.3 Outlook

The effects in single transverse spin asymmetries for forward hadron production from transversely polarized $p+p$ collisions are more complicated than in polarized SIDIS. The issues surrounding universality and factorization on theoretical interpretation needs to be understood better. Therefore, it requires each individual effect to be isolated in future measurements. With the installation of Silicon VTX and FVTX detectors and setup of possible other new detectors, PHENIX will have an ability to make such measurements through some new channels. We would like to discuss some of them in the following.

8.3.1 Drell-Yan Process and W Boson Production

The Drell-Yan process in high-energy hadron collisions takes place when a quark of one hadron and an anti-quark of another hadron annihilate, creating a virtual photon which then decays into a pair of oppositely-charged leptons. This process was first suggested by Sidney Drell and Tung-Mow Yan in 1970 [38] to describe the production of lepton-antilepton pairs in high energy hadron collisions. Experimentally, this process was first observed by J.H. Christenson et al. in proton-uranium collisions at Alternating Gradient Synchrotron (AGS) in the Brookhaven national lab [39].

As we discussed above, the Drell-Yan process in transversely polarized proton collisions is extremely important because the change of the sign of asymmetry between Drell-Yan process and SIDIS is an important verification of current theoretical model calculations. However, the asymmetry of Drell-Yan is very difficult to be observed. The measured asymmetry by

estimate is not very large (roughly 5%) in PHENIX muons spectrometer acceptance. The cross section is very small so that it is very difficult to accumulate enough statistics without very good luminosity or measurement in a long time. Lots of randomly combined muons pairs from D and B meson decay mix with the Drell-Yan signal. With the help of FVTX detector, those decay muons can be effectively removed and the signal background ratio will be greatly improved.

The single transverse spin asymmetry of W bosons was proposed by Z.Kang and J.Qiu in 2009[40]. As same as the Drell-Yan process, there is only initial-state interaction in W boson production. Thus, it essentially can be used to test the sign change of asymmetry discussed above instead of Drell-Yan process. The asymmetry for W bosons would be very large, up to 30%. The PHENIX detectors with the installation of VTX and FVTX can only measure lepton decay from W bosons. Even for measuring leptops decay from W bosons, the estimated peak asymmetry can be about 10%. However, the cross section in the process is relatively small, so that it would be a challenge for PHENIX to collect enough statistics.

8.3.2 Di-jet and Photon-Jet Correlation

Obviously, the back-to-back di-jet correlation is a cleaner channel to measure the Sivers effect than di-hadron correlation since there is no fragmentation folded in. Thus, it completely avoid the Sivers effect mixing with the Collins effect. The current central-arm detectors of PHENIX experiment don't have full 2π acceptance, it is very difficult to fully reconstruct jets. The silicon VTX detector provides a 2π azimuthal coverage, which adds tracking capabilities to the central-arm detectors. Although the momentum resolution by the VTX detector alone is rather limited (about 20% in $\delta p/p$), the resolution is sufficient for selecting high p_T hadrons from the recoil jets. The large η coverage ($|\eta| < 1.2$) of the VTX detector is in particular essential for the measurement. The hardware work for VTX detector is almost finished, and the detector is expected to be installed in 2010.

Another way to measure the Sivers effect directly would be through the asymmetry in photon-jet production, which is proposed by A. Bacchetta et al in 2007 [41]. It was thought

to be another channel to test the modified universality of the Sivers distribution besides Drell-Yan and W boson production. However, the TMD factorization was directly used for the theoretical calculation in [41], which is proven not to be true in this process [37]. It makes the theoretical interpretation of such a measurement more complicated. The difference between experimental measurements and theoretical prediction may indicate how big the violation of TMD factorization is in this process. It requires PHENIX to have an ability to measure photons at forward rapidity in order to do such photon-jet correlation measurements. PHENIX collaboration is writing a proposal to build Forward Calorimeter (FoCal) which will provide PHENIX a capability to measure photons within the region of $1 < |\eta| < 3$.

8.3.3 Open Charm Production

As we discussed above, the gluon Sivers function is not well constrained so far. A new window into the gluon structure of the nucleon was opened by a measurement of the transverse single spin asymmetry in open charm production. There are two channels that dominate open charm production; s-channel quark annihilation $q + \bar{q} \rightarrow c + \bar{c}$, and the gluon fusion process $g + g \rightarrow c + \bar{c}$. Gluons do not carry transverse spin, so for both channels there cannot be any polarization for charm quarks when the initial state protons are purely transversely polarized. The missing of final state quark polarization rejects the Collins effect and make the Sivers effect as the only source of a single spin asymmetry. With accomplishment of VTX and FVTX detector upgrade in PHENIX, D mesons can be tagged on an event-by-event basis, therefore a very clean sample of events can be produced for SSA analysis.

APPENDIX A. List of Good Runs and Fills in Run6 and Run8

Run6

List of good runs

190770 190771 190772 190774 190776 190777 190778 190891 190894 190895 190896 190897
190953 190954 190955 190956 190958 190960 190962 190966 190967 190970 190972 190973
190974 191068 191070 191071 191079 191093 191095 191097 191098 191099 191103 191104
191105 191107 191109 191110 191112 191215 191216 191219 191221 191309 191311 191320
191367 191368 191370 191371 191499 191504 191549 191556 191629 191630 191634 191652
191653 191656 191663 191665 191677 191693 191695 191753 191756 191762 191929 191931
191932 191933 191934 191935 191936 191937 192488 192489 192496 192497 192503 192505
192666 192672 192675 192678 192869 192878 192879 192880 192881 192882 192896 192910
192911 193024 193025 193026 193045 193046 193053 193056 193057 193059 193063 193066
193067 193142 193147 193581 193582 193583 193584 194307 194312 194313 194314 194315
194316 194320 194321 194450 194451 194454 194455 194456 194457 194458 194498 194499
194500 194501 194502 194503 194504 194505 194516 194517 194522 194524 194526 194527
194528 194529 194531 194569 194570 194575 194576 194577 194578 194579 194580 194581
194748 194760 194763 194766 194767 194772 194773 194777 194780 194781 194782 195690
195694 195696 195697 195880 195884 195895 195900 195901 195903 197390 197391 197401
197402 197408 197409 197517 197521 197522 197758 197762 197763 197764 197765 197766
197767 197768 197771 197772 197774 197789 197794 197795

List of good fills

7627 7630 7632 7637 7639 7641 7642 7645 7651 7652 7654 7655 7657 7658 7662 7671 7673 7681 7682 7685 7688 7689 7691 7697 7712 7718 7722 7724 7725 7729 7739 7740 7753 7756 7772 7775 7780 7781

Run8

List of good runs

256541 256543 256544 256545 256546 256548 256549 256565 256566 256568 256569 256570 256571 256719 256721 256736 256737 256989 256990 257001 257002 257003 257004 257080 257084 257085 257123 257124 257125 257126 257130 257131 257132 257151 257159 257275 257323 257324 257326 257327 257329 257330 257331 257333 257335 257336 257337 257338 257339 257409 257410 257412 257414 257415 257477 257478 257480 257495 257497 257498 257500 257501 257509 257510 257511 257514 257519 257520 257521 257522 257525 257526 257528 257529 257645 257648 257650 257651 257652 257654 257655 257841 257842 257844 257848 257850 257851 257920 257927 257928 257929 257930 257931 257936 257937 257939 257940 257947 257948 257953 257954 258249 258250 258251 258253 258254 258255 258256 258260 258262 258263 258264 258265 258266 258267 258385 258386 258387 258388 258389 258390 258391 258392 258393 258394 258396 258489 258490 258491 258493 258495 258496 258497 258498 258503 258505 258506 258507 258509 258510 258511 258512 258513 258511 258648 258648 258649 258650 258651 258652 258653 258654 258655 258664 258666 258668 258669 258676 258677 258678 258794 258795 258796 258797 258794 258795 258796 258797 258798 258800 258801 258807 258809 258811 258812 258813 258814 258815 258818 258819 258842 258843 258844 258845 258849 258851 258852 258859 258861 258862 258863 258864 258866 258867 258868 258869 259040 259041 259042 259043 259044 259051 259052 259053 259057 259058 259059 259060 259116 259117 259118 259123 259127 259252 259253 259254 259255 259256 259257 259258 259259 259276 259278 259279 259280 259281 259284 259285 259286 259288 259289 259365 259367 259368 259370 259371 259372 259465 259466 259467

259470 259472 259474 259476 259488 259491 259492 259493 259499 259499 259556 259557 259560 259561 259562 259563 259564 259565 259565 259567 259568 259569 259570 259571 259575

List of good fills

9884 9885 9888 9890 9897 9898 9905 9906 9909 9910 9919 9920 9935 9937 9938 9939 9940 9942 9948 9949 9951 9965 9966 9971 9972 9973 9975 9977 9978 9979 9980 9981 9986 9989 9990 9991 9992 9996 9997 9998 10000

BIBLIOGRAPHY

[1] I. Alekseev et al. *Polarized proton collider at RHIC*, Nucl. Instrum. Meth., A499:392-414, 2003.

[2] A. Zelenski et al., *Optically-pumped polarized H^- ion source for RHIC spin physics*, Rev. Sci. Instrum., 73:888-891, 2002.

[3] T. Roser, Coordinator, *Conceptual Design for the Acceleration of Polarized Protons in RHIC*, September 3, 1993.

[4] L. H. Thomas, *Philos. Mag.*, 3:1, 1927.

[5] T. Roser, *RHIC spin program: machine aspects and recent progress*, 2002.

[8] I. Nakagawa et al., *Run05 proton beam polarization measurements by pC-polarimeter*, RHIC/CAD Accelerator Physics Note, 275, 2007.

[9] H. Okada et al., *Measurement of the analyzing power in $p+p$ elastic scattering in the peak CNI region at RHIC*, Phys. Lett., B 638: 450-452006.

[10] I. Nakagawa et al., *RHIC polarimetry*, Eur. Phys. J., Special Topics 162, 259-265 2008.

[11] W. W. MacKay et al., *COMMISSIONING SPIN ROTATORS IN RHIC*, Proceedings of the 2003 Particle Accelerator Conference, 2003.

[12] C. Adler et al., Nucl. Instrum. Meth., A499:433C436, 2003.

[13] M. Allen et al., Nucl. Instrum. Meth., A499:549C559, 2003.

[14] M. Aizawa et al., Nucl. Instrum. Meth., A499:508C520, 2003.

[15] L. Aphecetche et al., *PHENIX calorimeter*, Nucl. Instrum. Meth., A499:521-536, 2003

[16] H. Akikawa et al., *Physics Research Section A: Accelerators, Spectrometers, Detectors and Associated Equipment*, Nucl. Instrum. Meth., 537 (2003).

[17] A. M. Glenn, *Single Muon Production and Implications for Charm in 200 GeV Au+Au Collisions*, PhD thesis, University of Tennessee, 2004.

[18] PHENIX Collaboration: A. Adare, et al., *The gluon spin contribution to the proton spin from the double helicity asymmetry in inclusive π^0 production in polarized p+p collisions at $\sqrt{s}$=200 GeV*, Phys. Rev. Lett., 103:012003, 2009.

[19] R. L. Jaffe and X.-D. Ji. *Chiral odd parton distributions and polarized Drell-Yan*, Phys. Rev. Lett., 67:552-555, 1991.

[20] G. L. Kane, J. Pumplin, and W. Repko. *Transverse quark polarization in large pT reactions, e^+e^-jets, and leptoproduction: A testof QCD*, Phys. Rev Lett., 41:1689, 1978.

[21] E704 Collaboration: D.L. Adams et al., *Analyzing Power in Inclusive π^+ and π^- Production at High x_F with a 200GeV Polarized Proton Beam.*, Phys. Lett. B 264, 462 (1991).

[22] For reviews, see U. D'Alesio and F. Murgia, Prog. Part. Nucl. Phys. 61, 394 (2008).

[23] D. W. Sivers, *Single-spin production asymmetries from the hard scattering of pointlike constituents*, Phys. Rev. D41, 83 (1990).

[24] J. W. Qiu and G. Sterman, *Single transverse spin asymmetries*, Phys. Rev. Lett. 67, 2264 (1991).

[25] A. V. Efremov and O. V. Teryaev, Sov. J. Nucl. Phys. 36, 140 (1982)

[26] J. Collins, Nucl. Phys. B 396, 161 (1993)

[27] D.Boer and W.Vogelsang, *Asymmetric jet correlations in $p + p^\uparrow$ scattering*, Phys. Rev. D 69, 094025 (2004).

[28] J. C. Collins. *Fragmentation of transversely polarized quarks probed in transverse momentum distributions*, Nucl. Phys., B396:161-182, 1993

[29] J. C. Collins. *Hard scattering in QCD with polarized beams*, Nucl. Phys., B394:169-199, (1993).

[30] J. C. Collins, S. F. Heppelmann, and G. A. Ladinsky. *Measuring transversity densities in singly polarized hadron - hadron and lepton - hadron collisions*, Nucl. Phys., B 420:565-582, (1994).

[31] X. Artru, J. Czyzewski, and H. Yabuki. *Single spin asymmetry in inclusive pion production, Collins effect and the string model.* Z. Phys., C 73:527-534, (1997).

[32] K. Abe, et al., *Measurement of Azimuthal Asymmetries in Inclusive Production of Hadron Pairs in e^+e^- Annihilation at Belle*, Phys. Rev. Lett. 96, 232002 (2006).

[33] L. Aphecetche et al. *PHENIX calorimeter*, Nucl. Instrum. Meth., A499: 521-536, (2003).

[34] J.Lajoie et al. PHENIX Analysis Note 742, (2008).

[35] S. S. Adler et al in PHENIX Collaboration, *Jet properties from dihadron correlations in $p+p$ collisions at $\sqrt{s} = 200 GeV$*, Phys. Rev. D 74, 072002 (2006).

[36] Daniel de Florian and Rodolfo Sassot, *Global analysis of fragmentation functions for protons and charged hadrons*, Phys. Rev. D 76, 074033 (2007).

[37] Ted Rogers and Piet Mulders, *No generalized transverse momentum dependent factorization in the hadroproduction of high transverse momentum hadrons*, Phys. Rev. D 81, 094006 (2010).

[38] S.D. Drell and T.M. Yan, *Massive Lepton-Pair Production in Hadron-Hadron Collisions at High Energies*, Phys. Rev. Lett. 25, 902-902 (1970).

[39] J.H. Christenton et. al., *Observation of Massive Muon Pairs in Hadron Collisions*, Phys. Rev. Lett. 25, 1523-1526 (1970).

[40] Z.Kang and J.Qiu, *Test the time-reversal modified universality of the Sivers function*, Phys. Rev. Lett. 103, 172001 (2009).

[41] A. Bacchetta et. al., *Sivers single-spin asymmetry in photon-jet production*, Phys. Rev. Lett. 99 212002 (2007).

[42] C. G. Callan and D. J. Gross, *Bjorken Scaling in Quantum Field Theory*, Phys. Rev. D 8, 4383-4394 (1973).

[43] M. Gell-Mann, *A Schematic Model of Baryons and Mesons*, Physics Letters 8 (3): 214-215 (1964).

[44] G. Zweig, *An SU(3) Model for Strong Interaction Symmetry and its Breaking*, CERN Report No.8182/TH.401 (1964).

[45] Ne'emann, *Derivation of strong interactions from gauge invariance*, Nuclear Physics 26: 222 (1961).

[46] E.D. Bloom et. al., *High-Energy Inelastic e-p Scattering at* 6° *and* 10°. Physical Review Letters 23 (16): 930-934 (1969).

[47] M. Breidenbach et. al., *Observed Behavior of Highly Inelastic Electron-Proton Scattering*, Physical Review Letters 23 (16): 935-939 (1969).

[48] R.P. Feynman, *Very High-Energy Collisions of Hadrons*, Physical Review Letters 23 (24): 1415-1417 (1969).

[49] J.D. Bjorken, *Asymptotic Sum Rules at Infinite Momentum*, Physical Review 179: 1547-1553 (1969).

[50] C. G. Callan and D. J. Gross, *High-Energy Electroproduction and the Constitution of the Electric Current*, Phys. Rev. Lett. 22, 156 (1968).

[51] D. de Florian, R. Sassot, M. Stratmann, and W. Vogelsang, *Global Analysis of Helicity Parton Densities and their Uncertainties*, Phys. Rev. Lett. 101, 072001 (2008).

[52] J. Soffer, *Positivity Constraints for Spin-Dependent Parton Distributions*, Phys. Rev. Lett. 74 1292-1294 (1995).

[53] R. Seidl et al. Belle Collaboration, *Measurement of Azimuthal Asymmetries in Inclusive Production of Hadron Pairs in e^+e^- Annihilation at Belle*, Phys. Rev. Lett. 96, 232002 (2006).

[54] A. D. Martin, W. J. Stirling, R. S. Thorne and G. Watt, *Update of parton distributions at NNLO*, Phys. Lett. B 652, 292 (2007).

[55] P. Nadolsky et al., *Implications of CTEQ global analysis for collider observables*, Phys. Rev. D 78 : 013004 (2008).
CTEQ Website: *http://www.phys.psu.edu/ cteq/*

[56] R.Ball et al., *Combined PDF and strong coupling uncertainties at the LHC with NNPDF2.0*, arXiv:1005.0397v1 [hep-ph].
NNPDF Website: *http://sophia.ecm.ub.es/nnpdf/*

[57] M. Hirai1, S. Kumano and N. Saito, *Determination of polarized parton distribution functions with recent data on polarization asymmetries*, Phys. Rev. D 74, 014015 (2006).

[58] M. Hirai1, S. Kumano and N. Saito, *Determination of polarized parton distribution functions and their uncertainties*, Phys. Rev. D 69, 054021 (2004).

[59] M. Gluck, E. Reya, M. Stratmann, and W. Vogelsang, *Models for the polarized parton distributions of the nucleon*, Phys. Rev. D 63, 094005 (2001).

[60] Daniel de Florian, Rodolfo Sassot, Marco Stratmann, Werner Vogelsang, *Extraction of spin-dependent parton densities and their uncertainties*, Phys. Rev. D 80, 034030 (2009).

[61] PHENIX Collaboration, *Jet properties from dihadron correlations in $p+p$ collisions at $\sqrt{s} = 200 GeV$*, Phys. Rev. D 74, 072002 (2006).

[62] H. Liu et al., *Run8pp 200GeV Muon Arm QA*, PHENIX analysis note 833.

[63] CNI Polarimeter Group, *2008 Polarizations for RHIC*, http://www4.rcf.bnl.gov/ cnipol/.

[64] The Coordinated Theoretical-Experimental Project on QCD (CTEQ), http://www.phys.psu.edu/ cteq/.

[65] MRST group, http://durpdg.dur.ac.uk/hepdata/mrs.html.

[66] NNPDF group, http://sophia.ecm.ub.es/nnpdf/.

[67] Ashman J., et al. Phys. Lett. B, 1988, v. 206, 364; Nucl. Phys. B, 1989, v. 328, 1.

[68] S. Arnold et al., *Sivers effect at HERMES, COMPASS and CLAS12*, arXiv:0805.2137.

[69] C.J. Bomhof et al., *Single-Transverse Spin Asymmetry in Dijet Correlations at Hadron Colliders*, Phys. Rev. D 75, 074019 (2007).